ACOUSTIC DYNAMICS OF NANOPARTICLES AND NANOSTRUCTURED PHONONIC CRYSTALS

PAN HUIHUI (B. Sc)

A THESIS SUBMITTED
FOR THE DEGREE OF DOCTOR OF PHILOSOPHY
DEPARTMENT OF PHYSICS
NATIONAL UNIVERSITY OF SINGAPORE
2013

Acknowledgements

I would like to express my deepest appreciation to my supervisor, Prof. Kuok Meng Hau, not only for his advice, encouragement and unwavering dedication, but also for being a great mentor to me professionally. I would also like to thank my co-supervisor Associate Prof. Lim Hock Siah for his great and endless help in my theoretical simulations. I am very grateful for all their guidance and support in my doctoral research over the past four years and I feel myself very fortunate to be under their supervision.

Many thanks to Prof. Ng Ser Choon for his patient, fruitful discussions, and for sharing his extensive research knowledge with me. Thanks also go to our research fellows Dr. Wang Zhikui and Ms. Vanessa Zhang Li for their invaluable guidance on the Brillouin measurements and analyses of experimental data. Technical support from our laboratory technologist Mr. Foong Chee Kong is much appreciated. The support and assistance provided by my fellow graduate students, Ma Fusheng, Hou Chenguang, Sun Jingya, Di Kai and Lin Cheng Sheng are gratefully acknowledged.

Additionally, I would like extend my gratitude to Prof. Adekunle Olusola Adeyeye and Assistant Prof. Yang Hyunsoo of the Department of Electrical and Computer Engineering, as well as Asst. Prof. Lu Xianmao of the Department of Chemical and Biomolecular Engineering of National University of Singapore for fabricating the samples studied in this thesis.

I am grateful to Associate Prof. Sow Chorng Haur for his advice and help in the fabrication of some colloidal samples. Thanks are also due to Sharon Lim Xiaodai, Wu Jianfeng, Mahdi Jamali, Yan Yuanjun and Diao Yingying for helping me with the sample fabrication.

In addition to the people mentioned above, I would like to thank all my friends whose support and encouragement have made my PhD life easier, richer, happier and more memorable.

Last but not least, I wish to express my gratitude to my family members for their understanding, support and encouragement.

Table of Contents

Abstract

In this thesis, Brillouin light scattering, a powerful technique for probing the elastic properties and phonon propagation in nanostructured materials at hypersonic frequencies, has been employed to investigate the confined acoustic phonons in single-crystal gold nano-octahedra and the surface phonon dispersions in one- and two-dimensional hypersonic phononic crystals. Theoretical investigations, based on finite element analysis, of the acoustic vibrational modes of gold nano-octahedra and the phonon dispersions of the phononic crystals have also been undertaken.

The size-dependence of the vibrational mode frequencies of octahedron-shaped gold nanocrystals has been measured by micro-Brillouin spectroscopy. Our analysis reveals that the nine well-resolved peaks observed are due to confined acoustic modes, with each peak arising from more than one mode. The elastic constants of the nanocrystals are found to be comparable to those of bulk gold crystals. Our findings suggest that the eigenfrequencies of any free regular-shaped homogeneous object always scale with its inverse linear dimension. Additionally, this universal relationship is valid for such objects of any size in the classical regime, and is independent of elastic properties.

The surface acoustic dispersions of a one-dimensional (1D) periodic array of alternating Fe (or Ni, Cu) and $Ni_{80}Fe_{20}$ (Py) nanostripes on a SiO_2/Si substrate have been investigated. The measured phononic band structures of surface elastic waves reveal Bragg and hybridization bandgaps for all three samples studied. These hybridization bandgaps arise from the avoided crossing of the Rayleigh waves and the zone-folded Sezawa waves. Two other 1D phononic crystals measured are in the form of periodic arrays of alternating Py and BARC (bottom anti-reflective coating) nanostripes on a Si(001) substrate, with respective 350 nm and 400 nm lattice constants. The observed phononic gaps of these two samples are considerably larger than those of laterally patterned multi-component crystals previously studied. Additionally, the phonon hybridization bandgap is found to have an unusual origin in the hybridization and avoided crossing of the zone-folded Rayleigh and pseudo-Sezawa waves. The surface phonon dispersion and gap widths can be tunable by varying the lattice constants.

Also studied in this thesis is a two-dimensional bi-component nanostructured crystal, in the form of a periodic chessboard array of alternating Py and cobalt square dots on a SiO_2/Si substrate, which has been fabricated using high-resolution electron-beam lithographic, sputtering, etching, and lift-off techniques. The dispersion relations of surface acoustic- and optical-like waves along the Γ-M and Γ-X symmetry directions have been mapped. The measured phononic band structures exhibit diverse features, such as partial hybridization bandgap and unusual surface optical-like phonon branches, where there are out-of-phase vibrational characteristics between neighboring dots. Numerical simulations generally reproduced the experimental dispersion relations.

List of Publications

Journal articles:

1. H. H. Pan, Z. K. Wang, H. S. Lim, S. C. Ng, V. L. Zhang, M. H. Kuok, T. T. Tran, and X. M. Lu, "Hypersonic confined eigenvibrations of gold nano-octahedra." *Applied Physics Letters* **98**, 133123 (2011).
2. V. L. Zhang, F. S. Ma, H. H. Pan, C. S. Lin, H. S. Lim, S. C. Ng, M. H. Kuok, S. Jain, and A. O. Adeyeye, "Observation of dual magnonic and phononic bandgaps in bi-component nanostructured crystals." *Applied Physics Letters* **100**, 163118 (2012).
3. V. L. Zhang, C. G. Hou, H. H. Pan, F. S. Ma, M. H. Kuok, H. S. Lim, S. C. Ng, M. G. Cottam, M. Jamali, and H. Yang, "Phononic dispersion of a two-dimensional chessboard-patterned bi-component array on a substrate" *Applied Physics Letters* **101**, 053102 (2012).
4. H. H. Pan, V. L. Zhang, K. Di, M. H. Kuok, H. S. Lim, S. C. Ng, N. Singh, and A. O. Adeyeye, “Phononic and Magnonic Dispersions of Surface Waves on a Permalloy/BARC Nanostructured Array” *Nanoscale Research Letters* **8**, 115 (2013).

International conferences:

1. H. H. Pan, V. L. Zhang, Z. K. Wang, H. S. Lim, S. C. Ng, and M. H. Kuok, “Brillouin Study of Phononic Crystals” **ICMAT** (International Conference on Materials for Advanced Technologies), (2011) Singapore. (Oral presentation)
2. H. H. Pan, V. L. Zhang, H. S. Lim, S. C. Ng, M. H. Kuok, S. Jain, and A. O. Adeyeye, “Brillouin Study of the Bandgap Structure of Laterally-patterned Phononic Crystals” **PHONONS 2012** (XIV International Conference on Phonon Scattering in Condensed Matter), (2012) Ann Arbor, MI, USA.

List of Tables

List of Figures

List of Abbreviations

1D	One-dimensional
2D	Two-dimensional
3D	Three-dimensional
BARC	Bottom anti-reflective coating
BLS	Brillouin light scattering
BZ	Brillouin zone
DUV	Deep ultraviolet
EBL	Electron beam lithography
EG	Ethylene glycol
FP	Fabry-Pérot
FSR	Free spectral range
FWHM	Full width at half maximum
HFPSW	High-frequency pseudo-surface wave
IPA	Isopropyl alcohol
LGM	Longitudinal guided mode
LR	Longitudinal resonance
MIBK	Methyl isobutyle ketone
MPC	Magphonic crystal
PDDA	Poly(diallyldimethylammonium chloride)
PMMA	Polymethyl methacrylate
PS	Polystyrene
PSAW	Pseudo-surface acoustic wave

Py	Permalloy, $Ni_{80}Fe_{20}$
RW	Rayleigh wave
SAED	Selected area electron diffraction
SAW	Surface acoustic wave
SEM	Scanning electron microscopy
SOW	Surface optical-like wave
SW	Sezawa wave
TEM	Transmission electron microscopy

Chapter 1 Introduction

Nowadays, there is increasing interest in nanoscale structures in view of their intriguing properties and applications in diverse areas such as catalysis, biosensing, drug delivery, optoelectronics, and nonlinear optics [1-8]. These properties differ from those of the corresponding bulk materials because of surface and quantum effects. For instance, the surface to volume ratio of a nanoparticle is larger compared to that of the bulk material, making some chemical reactions more likely to take place [3,4], which is important for both basic research and applications such as crystal growth, catalysis, chemical and biochemical sensing. Also, energy quantization due to low dimensionality would affect the magnetic, electrical, optical, acoustic and mechanical properties of nanostructures [5-8].

An understanding of the acoustic and mechanical properties of nanostructures is of great importance to both fundamental physics and their applications. In nanoscale materials, the acoustic phonon spectrum undergoes modification due to spatial confinement resulting in quantized phonon modes [8]. Thus the acoustic dynamics of nanostructures depend on their size and shape, as well as their constituent materials. For example, for spherical particles, their acoustic modes are found to have distinct frequencies which are inversely proportional to their diameters [9-11]. These confined acoustic vibrational modes in single nanoparticles are called eigenvibrations or eigenmodes of these nanoparticles. By studying the eigenvibrations of these nanoparticles, their mechanical and thermal properties for instance can be extracted, which would contribute to their applications as structural and functional elements in, e.g., biological sensing devices. Among the types of materials studied, noble metal nanoparticles have been the focus of extensive studies due to their remarkable optical properties and numerous applications, such as surface plasmonics, chemical sensing, and photothermal therapy [3,12,13]. One of the main objectives of this thesis is the elucidation of the acoustic dynamics of gold nano-octahedra.

Besides the confined eigenmodes of single nanoparticles, another interesting research area is the propagation of elastic waves in phononic crystals. Nanostructured phononic crystals, the elastic analogue of photonic crystals, are novel metamaterials that have the potential to control and manipulate the propagation of phonons. These materials possess periodic variations of density and elastic properties, resulting in the formation of phononic bandgaps which prevent acoustic waves with certain frequencies from propagating through them. As such, phononic crystals, besides being of great fundamental scientific interest, are expected to show enormous promise in a wide variety of applications like acoustic lasers, heat management devices, and acoustic superlenses [14,15].

With the advancement in nanofabrication techniques, phononic crystals in the hypersonic range have been realized and actively investigated over the past few years. Hypersonic phononic crystals are expected to have applications in the area of heat conductivity because of their ability to control the flow of thermal phonons in them. Recently, Hopkins *et al.* (2010) has succeeded in observing the reduction in the thermal conductivity of single crystalline silicon by phononic crystal patterning [16]. In addition, the lattice spacing of hypersonic phononic crystals is of the order of optical light wavelength, thus they can exhibit dual phononic and photonic bandgaps and enhance photon-phonon interactions [17]. These photonic-phononic materials, also called phoxonic crystals [18-22], are attracting great interest as they are expected to possess both the attributes and functionalities arising from the bandgap structures of their component excitations which permit their potential application; for example, in the design of acousto-optical devices. Another class of materials with dual-excitation bandgaps is the magnonic-phononic crystals [23-25]. These novel metamaterials, which we term *magphonic* crystals (MPCs), possess simultaneous magnonic and phononic bandgaps. As magnons (spin waves) are outside the scope of this thesis, only the phononic properties of magphonic crystals studied will be considered.

Most experiments on hypersonic dispersions of phononic crystals focused on bulk acoustic waves. Recent works however have stimulated interest in surface acoustic waves (SAWs) propagating in such structures, and these studies would result in wide applications, particularly in the area of SAW-based devices [26]. An elucidation of the surface phonon dispersions in one-dimensional (1D) and two-dimensional (2D) phononic crystals, by experimental and theoretical means, is the other key objective of this thesis.

1.1 Review of studies of confined acoustic vibrations

A milestone in the understanding of confined acoustic vibrations of an object is the analytical calculations of the eigenvibrations of an isotropic free elastic sphere by Lamb in 1882 [9]. In Lamb's theory, the eigenmodes of a free sphere can be classified into two categories: spheroidal and torsional. In the former, the motion has both radial and transverse components. In the latter, the motion has only a transverse component, and as the radial component is absent, the volume of the sphere remains unchanged. The modes are labeled by the angular momentum quantum number $l = 0, 1, 2. . .$, and the sequence of modes, in increasing order of energy, by $n = 1, 2, 3, . . .$. The frequencies of these modes, according to Lamb, are inversely proportional to the sphere diameter. Illustrative schematics of the ($n = 1$, $l = 0$) spheroidal and ($n =1$, $l = 2$) torsional modes are displayed in Fig. 1.1.

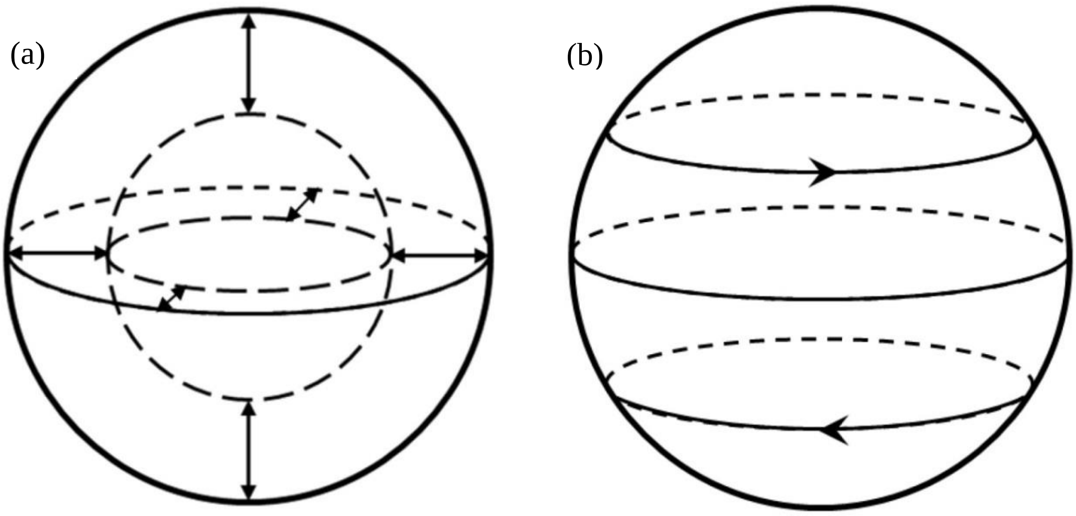

Fig. 1.1 Schematics of (a) the ($n = 1$, $l = 0$) spheroidal mode and (b) the ($n = 1$, $l = 2$) torsional mode of a sphere.

Since the establishment of the Lamb theory, many experimental studies of the eigenvibrations of spherical objects were undertaken. The first observation was reported in 1986 by Duval *et al.*, and was for Raman scattering from spinel microcrystallites [10]. They observed only one broad Raman peak whose frequency was found to vary with particle size. Based on the assumption that the microcrystallites are spherical, they attributed the observed Raman peak to a spheroidal mode of the microcrystallites. Their observations also suggested that the frequency of the spheroidal mode is proportional to the inverse diameters of these microcrystallites, in agreement with Lamb's prediction. Following this work, eigenmodes were extensively studied in various nano-objects, such as nanowires, nanotubes, nanorods and nanoparticles, using techniques like time-resolved spectroscopy, Raman scattering and Brillouin light scattering (BLS) [27-37]. Time-resolved spectroscopy is a time domain technique and usually only one or two modes can be observed, while Raman spectroscopy is technically limited to the detection of vibrations, with frequencies in the THz range, of very tiny particles (tens of nanometers). Brillouin light scattering is able to generally detect more vibrational modes with frequencies in the GHz range of larger nanoparticles.

The first comprehensive experimental verification of the Lamb's theory was reported by Kuok *et al.* in 2003 using BLS [11]. Up to six well-resolved Brillouin peaks were observed by them in 3D ordered arrays of unembedded SiO_2 nanospheres for four different sphere sizes. Clear evidence, of the mode quantization and of the linear relationship between the mode frequencies and the inverse sphere diameter, was shown in this study. Following this study, BLS was used to study the confined acoustic modes of loose silica spheres by Lim *et al.* (2004) [38]. They found that bulk acoustic waves can also be observed in larger microspheres. Cheng *et al.* (2005) measured the eigenvibrations in polystyrene opals and observed up to 21 acoustic modes [39]. Later, Li *et al.* (2006) developed a micro-Brillouin system which is able to measure the BLS signal from a single isolated SiO_2 sphere of about 260 nm in diameter [40], which interestingly is only about half the excitation wavelength used. The feasibility of recording Brillouin spectra from a single particle as tiny as this further enhances the capabilities of BLS as a powerful experimental tool for studying the acoustic dynamics of nanostructures. Brillouin spectra of single isolated polymer nanospheres were also measured by the same group [41].

In recent years, Brillouin studies were extended to more complicated particles, like hollow nanospheres [42], non-spherical particles [43], nanotubes [30], nanowires [44], and core-shell nanospheres [45,46]. Non-spherical particles studied include GeO_2 [43] and silver nanocubes [47].

As reviewed above, much experimental work has been carried out on the acoustic dynamics of free isotropic spherical nanoparticles. In contrast, very few experiments on the eigenvibrations of non-spherical crystalline nanoparticles have been reported. This is due to the difficulties in synthesizing high-quality monodisperse samples of such non-spherical nanoparticles and elucidating the nature of their eigenmodes.

Recently, noble metal nanocrystals have been the focus of extensive studies due to their unique chemical and physical properties which are strongly dependent on their size and shape [12,13,48-51]. With the rapid development of synthetic techniques, non-spherical metal nanocrystals of various symmetries such as cubes, octahedra, and other shapes were fabricated [52-55]. It is of great interest to study the acoustic dynamics of these novel noble metal nanocrystals. BLS is particularly suitable to investigate the acoustic modes of these nanocrystals because of its capability of measuring anisotropic nanoparticles of any shape.

According to Lamb's theory, the eigenvibrations of a sphere contains spheroidal and torsional modes. It is known that not all these confined modes of a sphere are experimentally observable. Selection rules from eigenvibrations of a sphere proposed by Li *et al.* (2008) showed that only spheroidal modes with even l number were Brillouin active [56]. Montagna (2008) developed a method for calculating the intensity of inelastic light scattering spectra of the acoustic vibrations of nanospheres [57]. This method was used by Still *et al.* (2010) to calculate the BLS spectra for polystyrene spheres with diameter of 360 nm as well as silica spheres with diameter of 354 nm [58], giving good agreement between the experiment and theory. In this thesis, this method is applied to estimate the mode intensities of the eigenvibrations of crystalline non-spherical nanoparticles.

1.2 Surface acoustic waves on hypersonic phononic crystals

Acoustic waves travelling in phononic crystals are modified by their periodic variations of densities and elastic constants, giving rise to the formation of phononic bandgaps, within which the propagation of acoustic waves with certain frequencies is forbidden. Phononic crystals in the sonic, ultrasonic and hypersonic ranges have been widely studied during the past 20 years [14,15,59-65]. For example, sonic phononic gaps were first experimentally observed in 2D periodic arrays of stainless cylinders in air by Sánchez-Pérez *et al.* (1998) [59], and by Robertson and Rudy (1998) [60]. A complete ultrasonic bandgap in a 2D periodic square array of mercury cylinders in an aluminium alloy plate for the longitudinal mode has been realized [61]. A number of experiments on the mapping of the dispersion relations of hypersonic phononic crystals have been carried out [14,15, 62-65]. In this section, we first review some of the important recent BLS studies of the dispersion of bulk acoustic waves in hypersonic crystals. This will be followed by a review on similar studies of SAWs.

1.2.1 Hypersonic dispersion of bulk acoustic waves

In 2006, hypersonic phononic bandgap for bulk acoustic waves was first observed by Cheng *et al.* for a 3D assembly of polystyrene (PS) nanospheres infiltrated with refractive index matching fluid [15]. In this work, a gap at the first Brillouin zone boundary which is known as Bragg gap was observed. In addition, the width (and the center) of the gap was tuned by changing the elastic and density contrast of the component materials (and particle size).

Before this study, an experimental attempt to map the hypersonic phononic bandgap for bulk acoustic waves was carried out by Gorishnyy *et al.* (2005) using BLS to examine a 2D system comprising periodic triangular arrays of cylindrical holes in an epoxy matrix [14]. However, no phononic bandgap was observed because, due to the large lattice constant (1.36 μm) of the crystal, the gap was at frequencies below the BLS detection limit. Not surprisingly, their next study dealt with a 2D square lattice of cylindrical holes having a shorter lattice constant of 750 nm in epoxy [62]. The holes were infiltrated with phenylmethyl silicone which served as refractive index matching fluid. A Bragg gap between 1.21 and 1.57 GHz was observed. Despite using air instead of phenylmethyl silicone in their simulations of the dispersion relations, there is qualitative agreement between simulations and experiment.

In 2008, Still *et al.* reported two hypersonic phononic bandgaps of different nature coexisting in 3D colloidal films of PS and polymethyl methacrylate (PMMA) nanospheres [63]. One is a Bragg gap occurring at the first Brillouin zone boundary and the other is a hybridization gap arising from the hybridization of the eigenmodes of a nanosphere and a traveling mode in the phononic crystal.

The sizes of the above-mentioned hypersonic gaps observed, which are of the order of 0.5 GHz, are relatively small. Recently, a BLS study by Gommopoulos *et al.* (2010) of a 1D hypersonic phononic crystal in the form of a periodic multilayered system (SiO_2/PMMA) with a period of 100 nm found that it possesses a broad bandgap of 4.5 GHz [64]. BLS measurements of 1D superlattice structures of 100 and 117 nm lattice constants by Schneider *et al.* (2012) also revealed large bandgaps of several GHz [65], and that the gap position and width can be tuned by a rotation of the sample about the axis normal to the sagittal plane of the film.

In the reviewed experimental studies of the 1D, 2D and 3D systems, the observation of Bragg gaps is limited to the first Brillouin zone boundary. For a better understanding of bulk phonon propagation in hypersonic crystals, information on the band structures in higher-order Brillouin zones is needed. Therefore, to get a dispersion relation in more Brillouin zones should be of great interest and importance to fundamental research.

1.2.2 Introduction to surface acoustic waves

One of the aims of this thesis is to study dispersion of SAWs on phononic crystals. A brief introduction to SAWs is presented below. Surface Brillouin scattering has been widely used as a tool for studying the propagation of SAWs on solid materials [66].

SAWs can exist in a stress-free surface of a semi-infinite medium, as well as in a layered medium which is a film-substrate system. A semi-infinite medium is one in which its thickness is much larger than the penetration depth of the SAW displacement field. The penetration depth is normally of the order of the SAW wavelength. In a semi-infinite medium, there are three typical types of SAWs, namely, the surface Rayleigh wave (RW), the pseudo-surface acoustic wave (PSAW) and the high-frequency pseudo-surface wave (HFPSW) [67-69]. The RW is the only true surface wave as its acoustic Poynting vector is parallel to the surface, and its displacement field decays exponentially into the medium. In contrast, the Poynting vector of a PSAW has a perpendicular component that radiates energy into the bulk of the medium and is thus not parallel to the surface. The bulk acoustic waves at the surface of a semi-infinite medium give rise to a continuum of states lying at frequencies higher than the transverse bulk wave threshold. The continuous spectrum consists of acoustic waves composed of propagating bulk transverse waves and evanescent longitudinal waves. PSAWs, which exist as resonances in the continuum of bulk waves, are leaky waves which suffer attenuation as they propagate [67,68]. The HFPSW, also called longitudinal resonance (LR), has a phase velocity very close to that of the longitudinal bulk wave travelling parallel to the surface (longitudinal bulk wave threshold) [69].

Using surface Brillouin scattering, the RW and the continuum of waves above the transverse threshold, which are referred to as the Lamb shoulder, have been observed in semi-infinite media of semiconductors and metals [70,71]. Sharp resonances within the continuum of modes have also been observed in BLS spectra [66-68] and were assigned to PSAWs and HFPSWs. For example, Carlotti *et al.* (1992) [71] observed the coexistence of RW, PSAW, and HFPSW in GaAs $(1\bar{1}1)$ for propagation directions in the range of [110] to [121].

A common film-substrate system comprises a ‘slow’ film on a ‘fast’ substrate which means the transverse and longitudinal bulk wave velocities of the film are lower than the corresponding velocities of the substrate. In addition to RWs, higher-order Rayleigh modes known as Sezawa waves also exist in this system [72]. Sezawa waves consist of shear vertically and longitudinally polarized partial waves, whose field components propagate parallel to the surface and decay exponentially with distance into the substrate, thus confining the mode energy to the immediate vicinity of the film. Sezawa waves exist below the transverse threshold, and only over a restricted range of qh, where q is the wave number of the Sezawa wave and *h* is the film thickness. Sezawa modes have a low-frequency cutoff at which the phase velocity is equal to the substrate shear velocity.

Attenuated SAWs, called pseudo-Sezawa waves, which exist as resonances with the substrate continuum of modes have also been observed in film-substrate systems by surface BLS [66,73-76]. These pseudo-Sezawa waves lie within the Lamb shoulder near the transverse threshold and arise from shear vertical vibrations of the substrate which reach the film surface amplified, retaining the vertical transverse polarization [73]. As *qh* increases, these waves, would move closer to the transverse threshold of the Lamb shoulder, until a critical value of *qh* is reached, at which stage, a pure Sezawa wave separates from the Lamb shoulder and moves into the non-radiative region below the transverse threshold [76].

Other types of SAWs also exist in film-substrate systems. They include the Stoneley wave at the film-substrate interface, the generalized Love waves, and the longitudinal guided modes (LGMs) [72,77]. An LGM has a velocity in between the longitudinal velocity of the substrate and that of the film, but much larger than the transverse velocity of the substrate [77]. Thus, an LGM is a pseudo-surface mode that radiates energy into the substrate. Generalized Love waves are shear horizontal modes localized in the film which can be observed in *p*-*s* polarization spectra (*p* means **E** component of incident light is in the scattering plane, while *s* means **E** component of the scattered light is perpendicular to the scattering plane) of surface BLS [72].

1.2.3 Surface acoustic waves on phononic crystals

Mapping of the surface wave dispersions in hypersonic crystals was first performed in 1992 by Dutcher *et al.* using BLS, they successfully observed two types of phononic gaps in surface gratings on silicon of 250 nm period [78]. One type, called Bragg gaps appear at Brillouin zone boundaries, and are caused by the zone folding of the surface Rayleigh wave. The size of the Bragg gap was found to increase with zone number. The other type is the hybridization gap due to hybridization between the Rayleigh wave and the folded branch of the longitudinal resonance. A few months later, Giovannini *et al.* (1992) came up with an elasticity theory for the discrete and continuous spectra of phonon normal modes on a shallow grating [79]. This theory was able to provide a quantitative explanation of the experimental data on Si surface gratings of Dutcher *et al.* (1992). In the following years, Lee *et al.* (1994) extended Dutcher's work to higher-order Brillouin zones with Si gratings of a larger period of 350 nm [80]. In addition to the Bragg gaps at the Brillouin zone boundaries, two hybridization gaps within the second and the third Brillouin zone were observed.

In 2000, SAW dispersions in glass gratings, with a period of several micrometers were mapped by Dhar and Roger using the picosecond transient grating method [81]. In this work, two samples with respective groove depths of 300 nm and 1.15 µm produced rather different dispersion behaviors. The two measured branches of the dispersion relations, of the latter sample bend downwards beyond the first Brillouin zone boundary, while those of the other sample continue rising beyond the first zone boundary. This could be due to the fact that the periodic depth modulation of the sample with groove depth of 1.15 μm is more pronounced.

Phononic structures with periodicity created by fabricating a patterned thin film on a substrate are also gaining increasing interest [82-85]. Maznev (2008) studied the SAW dispersions of a periodic array of alternating copper and SiO_2 stripes, with a 3 μm-lattice constant, on a silicon substrate using the laser-induced transient grating technique [84]. The dispersion reveals a Bragg gap at the Brillouin zone boundary formed from the folding and avoided crossing of RWs, and a gap within the Brillouin zone. The latter gap was attributed to the hybridization and avoided crossing of the Rayleigh and Sezawa modes. A year later, the SAW dispersion of periodic arrays of alternating SiO_2 and tungsten stripes on a silicon substrate with a period of 2 μm was measured by Maznev and Wright (2009) [85].

Having reviewed works on SAW dispersion in various 1D phononic structures, we now turn our attention to SAW propagation in 2D phononic systems. These systems may possess complete SAW bandgaps, i.e., bandgaps independent of the direction of propagation of the SAWs. Although much theoretical research has been undertaken on the propagation of SAWs in 2D phononic crystals [86-89], there are few reports of experimentally observed SAW bandgaps [90,91]. They include a complete surface wave bandgap observed by Benchabane *et al.* (2006) in a square-lattice phononic crystal composed of void inclusions etched in a lithium niobate matrix [90]. Even fewer are studies involving the mapping of the SAW dispersion in 2D nanoscale phononic crystals. Very recently, Graczykowski *et al.* (2012) reported the observation of a hypersonic phononic bandgap for thermally excited SAWs in 2D phononic crystals comprising a square lattice of 100nm- or 150nm-high aluminum pillars with a spacing of 500 nm on a Si(001) substrate. The dispersion curves were mapped by BLS [92].

Most experiments on hypersonic phonon dispersions are confined to bulk acoustic waves. Relatively fewer experimental works on SAWs in hypersonic phononic crystals have been reported. Apart from studies of Si gratings, all the other works on mapping SAW dispersions in 1D systems deal with microstructures. It is of interest to extend the studies of periodic patterned structures on a substrate to nanostructured materials. It is also of interest to investigate higher-dimensional periodic structures whose surface phononic dispersions are more complex and richer in features than those of the 1D phononic crystals. Findings on the dispersion of SAWs in such structures may open further prospects for designing a new generation of phononic-crystal-based devices in application areas like acoustic signal processing.

1.3 Objectives

1.3.1 Confined acoustic vibrations in nanoparticles

The literature review in section 1.1 reveals that very few experimental works have been done on the confined acoustic modes of free crystalline non-spherical nanoparticles. Rarer still are experiments on the dependence of confined phonon mode frequencies of nanoparticles on their size. Such size-dependence measurements entail the fabrication of a series of batches of particles having a range of sizes, with each batch being monodisperse in both size and shape. This stringent requirement is difficult to meet. Very often syntheses would yield products with not only a wide size distribution, but also of various geometric shapes, thus rendering them unsuitable for size-dependence experiments. Moreover, no analytical analysis of the eigenmodes of these nanoparticles has been reported. For a comprehensive understanding of how the size of a non-spherical body would affect its acoustic dynamics, both experimental and theoretical work is required. Thus, one objective of the present study is to investigate the size-dependence of hypersonic confined eigenvibrations of non-spherical nanocrystals.

1.3.2 Surface acoustic waves on nanostructured phononic crystals

Pervious experimental investigations into the dispersions of SAWs on 1D hypersonic phononic crystals are confined to surface gratings on Si. There are only a few publications on the experimental mapping of SAW dispersions of periodic arrays of alternating metal and SiO_2 micron-sized wires on a Si substrate. Structures composed of metal wires are of particular practical importance due to their ubiquitous role in microelectronics. Thus, in this thesis, we extend the investigations on surface phononic dispersions to 1D periodic arrays of bi-component nanostripes, as well as 2D periodic arrays of bi-component nanosquares. Findings obtained would be of use not only to fundamental science but also to the development of devices for potential applications in areas like acoustic signal processing.

1.4 Outline of the thesis

In Chapter 2, a brief introduction will be given on the experimental technique used in this thesis, Brillouin light scattering, and its kinematics, as well as the scattering mechanism, followed by the experimental instrumentation and setup. Chapter 3 introduces the fundamental concepts of the theory of elasticity and the Brillouin spectrum intensity calculation method of the eigenmodes of nanoparticles. The experimental and theoretical studies undertaken in this thesis start from Chapter 4.

Chapter 4 presents the study of the size-dependence of the confined vibrational mode frequencies of octahedron-shaped gold nanocrystals. Chapters 5 and 6 investigate the surface acoustic wave dispersions in 1D phononic structures. The samples studied in Chapter 5 are periodic arrays of alternating $Ni_{80}Fe_{20}$ and Fe (or Ni, Cu) nanostripes on a SiO_2/Si substrate, while those in Chapter 6 are periodic arrays of alternating $Ni_{80}Fe_{20}$ and BARC (bottom anti-reflective coating) nanostripes on a Si(001) substrate. Chapter 7 presents the work done on the band structures of the surface acoustic and surface optical waves on a 2D chessboard-patterned phononic crystal, composed of a periodic array of alternating $Ni_{80}Fe_{20}$ and cobalt square nanodots on a SiO_2/Si substrate. Finally, Chapter 8 provides an overall conclusion of all experimental and theoretical research undertaken in this thesis.

References:

1. P. Moriarty, *Nanostructured materials,* Rep. Prog. Phys. **64**, 297 (2001).

2. V. C. Yang and T. T. Ngo, *Biosensors and Their Applications*, (Springer, 2000).

3. G. Merga, N. Saucedo, L. C. Cass, J. Puthussery, and D. Meisel, J. Phys. Chem. C **114**, 14811 (2010).

4. B. R. Cuenya, Thin Solid Films **518**, 3127 (2010).

5. F. J. Himpsel, J. E. Ortega, G. J. Mankey, and R. F. Willis, Adv. Phys. **47**, 511 (1998).

6. J. H. Davis, *The physics of low-dimensional semiconductors: an introduction*, (Cambridge University Press, New York, 1997).

7. A. B. Djurišić and Y. H. Leung, Small **2**, 944 (2006).

8. A. K. Arora, M. Rajalakshmi, and T. R. Ravindran, *Encyclopedia of Nanoscience and Nanotechnology*, (American Scientific Publishers, 2003).

9. H. Lamb, Proc. London Math. Soc. **13**, 189 (1882).

10. E. Duval, A. Boukenter, and B. Champagnon, Phys. Rev. Lett. **56**, 2052 (1986).

11. M. H. Kuok, H. S. Lim, S. C. Ng, N. N. Liu, and Z. K. Wang, Phys. Rev. Lett. **90**, 255502 (2003).

12. C. C. Li, K. L. Shuford, M. H. Chen, E. J. Lee, and S. O. Cho, ACS Nano **2**, 1760 (2008).

13. D. H. Kim, J. W. Heo, M. J. Kim, Y. W. Lee, and S. W. Han, Chem. Phys. Lett. **468**, 245 (2009).

14. T. Gorishnyy, C. K. Ullal, M. Maldovan, G. Fytas, and E. L. Thomas, Phys. Rev. Lett. **94**, 115501 (2005).

15. W. Cheng, J. J. Wang, U. Jonas, G. Fytas, and N. Stefanou, Nat. Mater. **5**, 830 (2006).

16. P. E. Hopkins, C. M. Reinke, M. F. Su, R. H. Olsson, E. A. Shaner, Z. C. Leseman, J. R. Serrano, L. M. Phinney, and I. El-Kady, Nano Lett. **11**, 107 (2010).

17. M. S. Kang, A. Nazarkin, A. Brenn, and P. S. J. Russell, Nat. Phys. **5**, 276 (2009).

18. V. Laude, J.-C. Beugnot, S. Benchabane, Y. Pennec, B. Djafari-Rouhani, N. Papanikolaou, J. M. Escalante, and A. Martinez, Opt. Express **19,** 9690 (2011).

19. Y. El Hassouani, C. Li, Y. Pennec, E. H. El Boudouti, H. Larabi, A. Akjouj, O. Bou Matar, V. Laude, N. Papanikolaou, A. Martinez, and B. Djafari Rouhani, Phys. Rev. B **82,** 155405 (2010).

20. N. Papanikolaou, I. E. Psarobas, and N. Stefanou, Appl. Phys. Lett. **96**, 231917 (2010).

21. Q. Rolland, M. Oudich, S. El-Jallal, S. Dupont, Y. Pennec, J. Gazalet, J. C. Kastelik, G. Leveque, and B. Djafari-Rouhani, Appl. Phys. Lett. **101**, 061109 (2012).

22. A. V. Akimov, Y. Tanaka, A. B. Pevtsov, S. F. Kaplan, V. G. Golubev, S. Tamura, D. R. Yakovlev, and M. Bayer, Phys. Rev. Lett. **101**, 033902 (2008).

23. S. Nikitov, Y. Gulyaev, V. Grigorevsky, A. Grigorevsky, I. Lisenkov, and R. Popov, J. Acoust. Soc. Am. **123**, 3040 (2008).

24. V. L. Zhang, F. S. Ma, H. H. Pan, C. S. Lin, H. S. Lim, S. C. Ng, M. H. Kuok, S. Jain, and A. O. Adeyeye, Appl. Phys. Lett. **100**, 163118 (2012).

25. V. L. Zhang, C. G. Hou, H. H. Pan, F. S. Ma, M. H. Kuok, H. S. Lim, S. C. Ng, M. G. Cottam, M. Jamali, and H. Yang, Appl. Phys. Lett. **101**, 053102 (2012).

26. S. Datta, *Surface Acoustic Wave Devices*, (Englewood Cliffs, NJ: Prentice-Hall, 1986)

27. S. Bhattacharyya and S. Samui, Appl. Phys. Lett. **84**, 1564 (2004).

28. X. Wang, A. Shakouri, B. Yu, X. H. Sun, and M. Meyyappan, J. Appl. Phys. **102**, 6 (2007).

29. C. E. Bottani, A. L. Bassi, M. G. Beghi, A. Podestà, P. Milani, A. Zakhidov, R. Baughman, D. A. Walters, and R. E. Smalley, Phys. Rev. B **67**, 155407 (2003).

30. A. M. Polomska, C. K. Young, G. T. Andrews, M. J. Clouter, A. Yin, and J. M. Xu, Appl. Phys. Lett. **90**, 201918 (2007).

31. M. Hu, X. Wang, G. V. Hartland, P. Mulvaney, J. P. Juste, and J. E. Sader, J. Am. Chem. Soc. **125**, 14925 (2003).

32. P. Zijlstra, A. L. Tchebotareva, J. W. M. Chon, M. Gu, and M. Orrit, Nano Lett. **8**, 3493 (2008).

33. J.H. Hodak, A. Henglein, G.V. Hartland, J. Chem. Phys. **111**, 8613 (1999).

34. M.A. van Dijk, M. Lippitz, and M. Orrit, Phys. Rev. Lett. **95**, 267406 (2005).

35. G.V. Hartland, Annu. Rev. Phys. Chem. **57**, 403 (2006).

36. A. Courty, A. Mermet, P.A. Albouy, E. Duval, and M.P. Pileni, Nat. Mater. **4**, 395 (2005).

37. R.S. Cataliotti, G. Compagnini, A. Morresi, M. Ombellia and P. Sassia, Phys. Chem. Chem. Phys. **4**, 2774 (2002).

38. H. S. Lim, M. H. Kuok, S. C. Ng, Z. K. Wang, Appl. Phys. Lett. **84**, 4182 (2004).

39. W. Cheng, J. J. Wang, U. Jonas, W. Steffen, G. Fytas, R. S. Penciu, and E. N. Economou, J. Chem. Phys. **123**, 121104 (2005).

40. Y. Li, H. S. Lim, S. C. Ng, Z. K. Wang, M. H. Kuok, E. Vekris, V. Kitaev, F. C. Peiris, and G. A. Ozin, Appl. Phys. Lett. **88**, 023112 (2006).

41. Y. Li, H. S. Lim, Z. K. Wang, S. C. Ng, and M. H. Kuok, J. Nanosci. Nanotechnol. **8**, 5869 (2008).

42. Y. Li, S. Lim, S. C. Ng, M. H. Kuok, F. Su, and X. S. Zhao, Appl. Phys. Lett. **90**, 261916 (2007).

43. Y. Li, H. S. Lim, S. C. Ng, M. H. Kuok, M. Y. Ge, and J. Z. Jiang, Appl. Phys. Lett. **91**, 093116 (2007).

44. W. L. Johnson, S. A. Kim, R. Geiss, C. M. Flannery, K. A. Bertness, and P. R. Heyliger, Nanotech. **23**, 495709 (2012).

45. T. Still, R. Sainidou, M. Retsch, U. Jonas, P. Spahn, G. P. Hellmann, and G. Fytas, Nano Lett. **8**, 3194 (2008).

46. J. Y. Sun, Z. K. Wang, H. S. Lim, S. C. Ng, M. H. Kuok, T. T. Tran, and X. Lu, ACS Nano **4**, 7692 (2010).

47. J. Y. Sun, Z. K. Wang, H. S. Lim, V. L. Zhang, S. C. Ng, M. H. Kuok, W. Zhang, S. Firdoz, and X. M. Lu, Solid State Commun. **152**, 501 (2012).

48. H. Portales, N. Goubet, L. Saviot, P. Yang, S. Sirotkin, E. Duval, A. Mermet, and M. P. Pileni, ACS Nano **4**, 3489 (2010).

49. M. Pelton, J. E. Sader, J. Burgin, M. Z. Liu, P. Guyot-Sionnest, and D. Gosztola, Nat. Nanotechnol. **4**, 492 (2009).

50. P. K. Jain, K. S. Lee, I. H. El-Sayed, and M. A. El-Sayed, J. Phys. Chem. B **110**, 7238 (2006).

51. E. Hutter, S. Boridy, S. Labrecque, M. Lalancette-Hebert, J. Kriz, F. M. Winnik, and D. Maysinger, ACS Nano **4**, 2595 (2010).

52. Y. Sun, Y. Xia, Science **298**, 2176 (2002).

53. H. Petrova, C.-H. Lin, S. de Liejer, M. Hu, J.M. McLellan, A.R. Siekkinen, B.J. Wiley, M. Marquez, Y. Xia, J.E. Sader, G.V. Hartland, J. Chem. Phys. **126**, 094709 (2007).

54. X. Lu, M. Rycenga, S.E. Skrabalak, B. Wiley, Y. Xia, Annu. Rev. Phys. Chem. **60**, 167 (2009).

55. C. L. Nehl, H. Liao, J. H. Hafner, Nano Lett. **6**, 683 (2006).

56. Y. Li, H. S. Lim, S. C. Ng, Z. K. Wang, and M. H. Kuok, Chem. Phys. Lett. **461**, 111 (2008).

57. M. Montagna, Phys. Rev. B **77**, 045418 (2008).

58. T. Still, M. Mattarelli, D. Kiefer, G. Fytas, and M. Montagna, J. Phys. Chem. Lett. **1**, 2440 (2010).

59. J. V. Sánchez-Pérez, D. Caballero, R. Mártinez-Sala, C. Rubio, J. Sánchez-Dehesa, F. Meseguer, J. Llinares, and F. Gálvez, Phys. Rev. Lett. **80**, 5325 (1998).

60. W. M. Robertson and J. F. Rudy, J. Acoust. Soc. Am. **104**, 694 (1998).

61. F. R. M. de Espinosa, E. Jiménez, and M. Torres, Phys. Rev. Lett. **80**, 1208 (1998).

62. T. Gorishnyy, J. H. Jang, C. Koh, and E. L. Thomas, Appl. Phys. Lett. **91**, 121915 (2007).

63. T. Still, W. Cheng, M. Retsch, R. Sainidou, J. Wang, U. Jonas, N. Stefanou, and G. Fytas, Phys. Rev. Lett. **100**, 194301 (2008).

64. N. Gomopoulos, D. Maschke, C. Y. Koh, E. L. Thomas, W. Tremel, H.-J. Butt, and G. Fytas, Nano Lett. **10**, 980 (2010).

65. D. Schneider, F. Liaqat, E. H. El Boudouti, Y. El Hassouani, B. Djafari-Rouhani, W. Tremel, H. J. Butt, and G. Fytas, Nano Lett. **12**, 3101 (2012).

66. P. Mutti, C. E. Bottani, G. Ghislotti, M. Beghi, G. A. D. Briggs, and J. R. Sandercock, in *Advances in Acoustic Microscopy*, edited by A. Briggs (Plenum, New York, 1995), Vol. 1, p. 249.

67. B. A. Auld, *Acoustic Fields and Waves in Solids*, Vol. 1 & 2 (Wiley, New York, 1973).

68. G. W. Farnell, in *Physical Acoustics*, edited by W. P. Mason and R. W. Thurston (Academic, New York, 1970), Vol. 6, p. 109.

69. R. E. Camley and F. Nizzoli, J. Phys. C **18**, 4795 (1985).

70. R. Loudon and J. R. Sandercock, J. Phys. C **13**, 2609 (1980).

71. G. Carlotti, D. Fioretto, L. Giovannini, F. Nizzoli, G. Socino, and L. Verdini, J. Phys. C **4**, 257 (1992).

72. G. W. Farnell and E. L. Adler, in *Physical Acoustics,* edited by W. P. Mason and R. N. Thurston (Academic, New York, 1972), Vol. 9, p. 35.

73. V. Bortolani, F. Nizzoli, G. Santoro, A. Marvin, and J. R. Sandercock, Phys. Rev. Lett. **43**, 224 (1979).

74. V. Bortolani, F. Nizzoli, G. Santoro, and J. R. Sandercock, Phys. Rev. B **25**, 3442 (1982).

75. R. C. Birtcher, M. H. Grimsditch, and L. E. McNeil, Phys. Rev. B **50**, 8990 (1994).

76. X. Zhang, J. D. Comins, A. G. Every, P. R. Stoddart, W. Pang, and T. E. Derry, Phys. Rev. B **58**, 13677 (1998).

77. B. Hillebrands, S. Lee, G. I. Stegeman, H. Cheng, J. E. Potts, and F. Nizzoli, Phys. Rev. Lett. **60**, 832 (1988).

78. J. R. Dutcher, S. Lee, B. Hillebrands, G. J. McLaughlin, B. G. Nickel, and G. I. Stegeman, Phys. Rev. Lett. **68**, 2464 (1992).

79. L. Giovannini, F. Nizzoli, and A. M. Marvin, Phys. Rev. Lett. **69**, 1572 (1992).

80. S. Lee, L. Giovannini, J. R. Dutcher, F. Nizzoli, G. I. Stegeman, A. M. Marvin, z. Wang, J. D. Ross, A. Amoddeo, and L. S. Caputi, Phys. Rev. B **49**, 2273 (1994)

81. L. Dhar and J. A. Rogers, Appl. Phys. Lett. **77**, 1402 (2000).

82. G. A. Antonelli, H. J. Maris, S. G. Malhotra, and J. M. E. Harper, J. Appl. Phys. **91**, 3261 (2002).

83. D. M. Profunser, O. B. Wright, and O. Matsuda, Phys. Rev. Lett. **97**, 055502 (2006).

84. A. A. Maznev, Phys. Rev. B **78**, 155323 (2008).

85. A. A. Maznev and O. B. Wright, J. Appl. Phys. **105**, 123530 (2009).

86. M. B. Assouar and M. Oudich, Appl. Phys. Lett. **99**, 123505 (2011).

87. Y. Yao, F. Wu, X. Zhang, and Z. Hou, J. Appl. Phys. **110**, 123503 (2011).

88. D. Yudistira, Y. Pennec, B. D. Rouhani, S. Dupont, and V. Laude, Appl. Phys. Lett. 100, 061912 (2012).

89. M. Oudich and M. B. Assouar, J. Appl. Phys. **111**, 014504 (2012).

90. S. Benchabane, A. Khelif, J. Y. Rauch, L. Robert, and V. Laude, Phys. Rev. E **73**, 065601 (2006).

91. S. Benchabane, O. Gaiffe, G. Ulliac, R. Salut, Y. Achaoui, and V. Laude, Appl. Phys. Lett. **98**, 171908 (2011).

92. B. Graczykowski, S. Mielcarek, A. Trzaskowska, J. Sarkar, P. Hakonen, and B. Mroz, Phys. Rev. B **86**, 085426 (2012).

Chapter 2 Brillouin Light Scattering

Brillouin light scattering (BLS), a non-contact and non-destructive technique which is ideal for studying acoustic phonons in nanostructures, is employed as an experimental tool for investigating the acoustic dynamics of nanoparticles and nanostructured phononic crystals. In this chapter, we will start with a brief introduction to the theory and experimental methodology of BLS.

Brillouin light scattering generally refers to the inelastic scattering of monochromatic laser light by thermally excited acoustic phonons or magnons in the gigahertz (GHz) frequency range. This inelastic scattering of thermal phonons was predicted by Brillouin [1] and independently by Mandelshtam [2] in the 1920s. The first observation of this phenomenon was made by Gross [3] in 1930 who measured BLS from liquids such as toluene and benzene using a low-pressure mercury arc as the light source.

2.1 Kinetics of Brillouin light scattering

In the particle description, the inelastic light scattering process is described in terms of the creation and annihilation of a phonon with wavevector $\boldsymbol{q}$ and angular frequency Ω. This process follows the laws of conservation of total momentum ($\boldsymbol{p} = \hbar \boldsymbol{k}$) and energy ($E = \hbar\omega$) schematically illustrated in Fig. 2.1.

$$\boldsymbol{k}_s = \boldsymbol{k}_i \pm \boldsymbol{q} , \tag{2.1}$$

$$\omega_s = \omega_i \pm \Omega , \tag{2.2}$$

where $\boldsymbol{k}_i$ and $\boldsymbol{k}_s$ are the respective wavevectors of the incident and scattered photons, while ω_i and ω_s are their respective angular frequencies. The "+" sign refers to the anti-Stokes event wherein a phonon is annihilated, with the scattered photon having an energy higher than that of the incident one, while the "–" sign corresponds to the Stokes event wherein a phonon is created, with the scattered photon having an energy lower than that of the incident one.

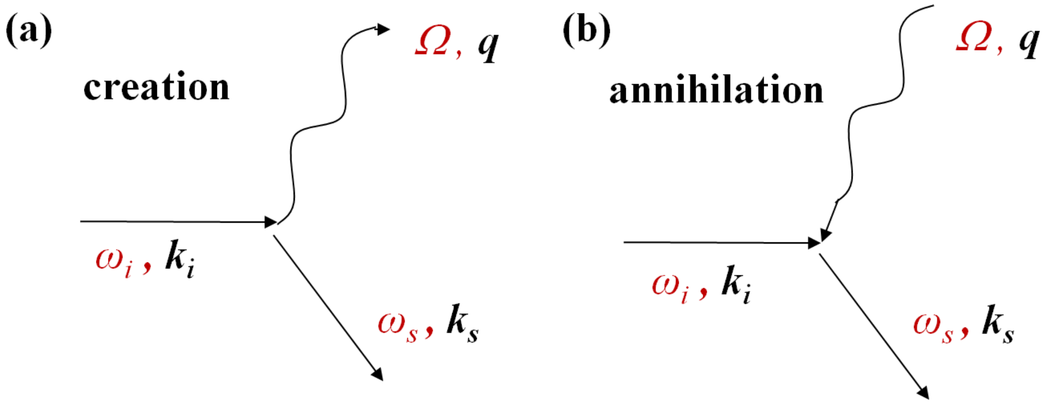

Fig. 2.1 Kinematics of (a) Stokes and (b) anti-Stokes scattering events in Brillouin light scattering.

The thermal phonon wavevector $\boldsymbol{q} = \boldsymbol{k}_s - \boldsymbol{k}_i$, and since its energy is much smaller than that of a visible photon, $\omega_i \approx \omega_s = \omega = 2\pi c/\lambda_0$ and $k_i \approx k_s = k = n\omega/c$, where n is the refractive index of the scattering medium for a given frequency of the light, c is velocity of light and λ_0 the incident laser light wavelength. The magnitude of phonon wavevector is

$$q = 2k\sin\left(\phi/2\right), \tag{2.3}$$

where ϕ is the scattering angle between the incident and scattered light (Fig. 2.2). As the photon wavevector k is of the order of 10^4 cm^{-1} for light in the visible and ultraviolet region, q is far below the distinguishing value of the Brillouin zone wavevectors (~10^8 cm^{-1}). This indicates that Brillouin scattering probes the dispersion curves of acoustic modes with very small wavevectors near the Brillouin zone center. In this region, the dispersion relation is linear for acoustic phonons, that is $\Omega = vq$, where v is the phase velocity of the phonon (in solids, $v \sim 10^3 - 10^4$ m/s). The angular frequency of the phonon is

$$\Omega = 2vk\sin\left(\frac{\phi}{2}\right) = \frac{2v}{c}n\omega\sin\left(\frac{\phi}{2}\right) = \frac{4\pi n}{\lambda_0}v\sin\left(\frac{\phi}{2}\right). \tag{2.4}$$

The maximum frequency shift corresponds to the backscattering geometry for which $\phi = 180^{\circ}$. The magnitude of Ω is of the order of 1 cm^{-1} (~ 30 GHz), which is too small to be recognized by grating spectrometers, which are mainly used in Raman scattering spectroscopy. Therefore, multi-pass tandem Fabry-Pérot (FP) interferometer is used to meet the required high resolution. It is noteworthy that Brillouin spectrum obtained from eigenmodes of nanoparticles is q-independent.

For metals, semiconductors and opaque film-substrate materials, BLS takes place near the sample surface and provides information on SAWs. The scattering geometry for an incident angle of θ_i and the scattered angle θ_s to the surface normal is shown in Fig. 2.2. The scattering plane contains the wavevector of the scattered light and the surface normal to the sample.

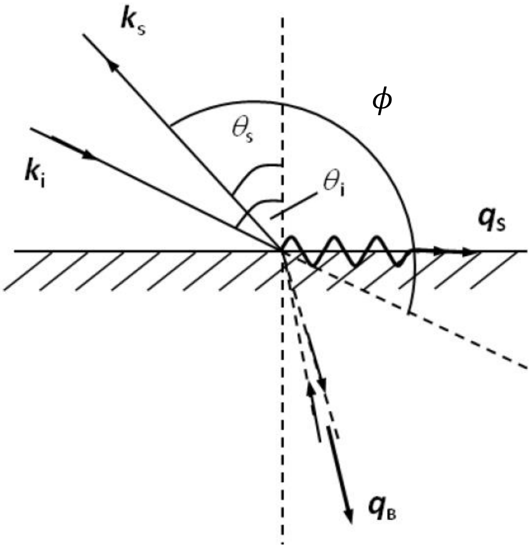

Fig. 2.2 Scattering geometry. $\boldsymbol{k}_i$ and $\boldsymbol{k}_s$ are the respective incident and scattered light wavevectors, $\boldsymbol{q}_S$ and $\boldsymbol{q}_B$ the surface and bulk phonon wavevectors, and θ_i and θ_s the respective incident and scattered angles.

Unlike the wavevector of bulk phonon $\boldsymbol{q}_B$, the surface phonon wavevector $\boldsymbol{q}_S$ is parallel to the sample surface, and thus

$$k\left(\sin\theta_i + \sin\theta_s\right) = \pm q_s . \tag{2.5}$$

In practice, the experiment is performed in the 180$^{\mathrm{o}}$-backscattering geometry for which $\theta_i = \theta_s = \theta$ and thus

$$q_s = \pm 2k\sin\theta = \pm\frac{4\pi}{\lambda_0}\sin\theta . \tag{2.6}$$

Here the magnitude of the surface wavevector is independent of the refractive index of the medium and only depends on the incident angle θ and the wavelength of the laser light λ_0. The frequency of the scattered phonon can be obtained from a recorded Brillouin spectrum, and the dispersion relation of SAWs can be mapped by changing the laser incident angle θ.

2.2 Scattering mechanism

Brillouin scattering is mediated by two principal mechanisms, *viz.* the surface ripple and the elasto-optic effects, depending on the opacity of and the probed volume in the scattering materials [4-6].

Surface ripple mechanism

In this mechanism, the light is scattered by dynamic corrugations in the surface profile. The phonon vibrations cause the surface to appear as a grating, i.e. ripple, traveling in the reverse or forward direction at velocity v_s. The ripple is capable of producing diffraction and changing the frequency of incoming light through Doppler effect, without invoking modulation of dielectric constant in the interior of the medium. Thus, the scattering cross section by ripple effect does not depend on the scattering volume or elasto-optic constants. This is the dominant scattering mechanism for surface acoustic waves in opaque solids, such as Rayleigh wave in metals. The inelastic component of the Brillouin spectrum displays prominent Stokes and anti-Stokes peaks with frequencies of $\Omega = \pm v_s q_s$. In addition to the Rayleigh wave, bulk acoustic waves incident on the surface can also cause dynamic surface corrugations, and these will be detected if the component of their wavevector parallel to the surface is equal to q_s. These are bulk waves with a surface character.

Elasto-optic mechanism

In the case where the material is not totally opaque, the incident light is able to penetrate some distance into the material to probe dynamic fluctuations in the strain field. The strain field of a thermally excited acoustic wave induces, through the elasto-optic effect, a periodic modulation of the dielectric constant or fluctuation in the refractive index. This fluctuation is analogous to a diffraction grating traveling at velocity v_B. An electromagnetic wave can interact with this grating when their wavelengths are properly matched. Inelastic scattering thus occurs. The strength of the scattering depends on the elasto-optic constants, and it is proportional to the scattering volume. In transparent materials, elasto-optic mechanism provides the main contribution to scattering cross section. Both bulk acoustic waves and some types of surface acoustic waves traveling within thin films can scatter the incident light via this mechanism. The line shape for bulk phonons is a Lorentzian profile whose width is proportional to the phonon lifetime.

In materials that are partially opaque, such as semiconductors, both ripple and elasto-optic effects are present, and the total Brillouin cross section is given by the combination of both contributions. In the case of a transparent film supported by opaque substrate, ripple effect at the local surface of the substrate and the interference between the two mechanisms, contribute to scattering by modes localized within the film and at the interface. However, when the film is thick enough compared to the phonon wavelength, this effect is negligible.

2.3 Experiment instrumentation and setup of BLS

The major components of a Brillouin system are an argon-ion laser, and a six-pass tandem Fabry-Pérot interferometer which is equipped with a silicon avalanche diode detector. A schematic of a typical BLS experimental setup is displayed in Fig. 2.3. The whole optical system and the interferometer are supported by an optical bench system which rests on a steel plate.

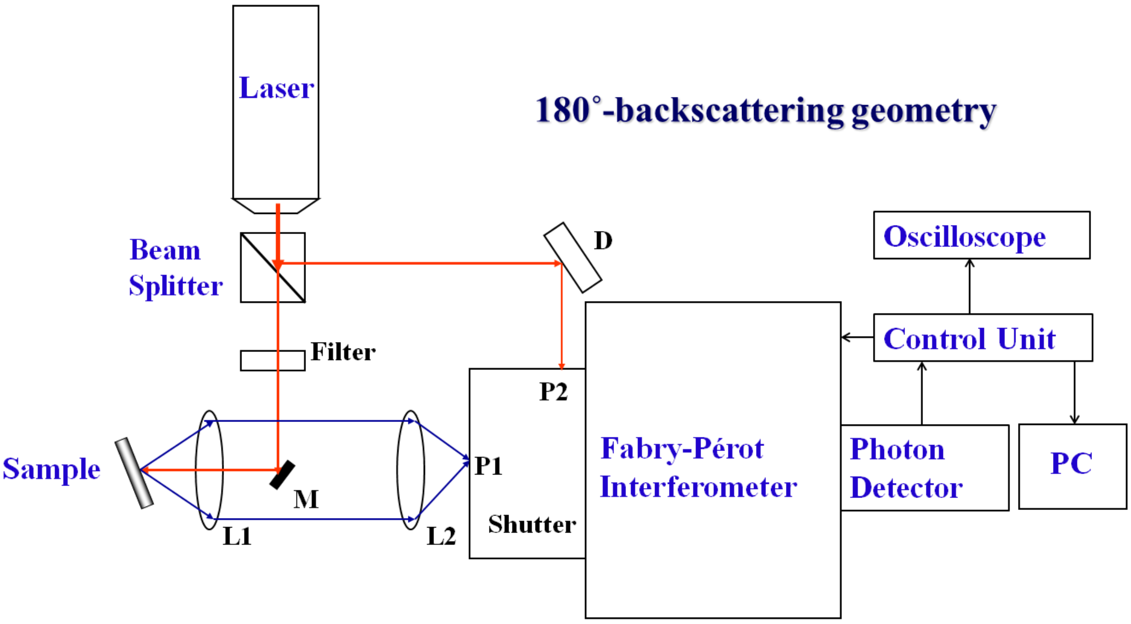

Fig. 2.3 A schematic of BLS set-up in the 180 °-backscattering geometry.

A Spectra-Physics BeamLok 2060-6RS argon-ion laser, equipped with microprocessor-based Model 587 Z-Lok accessory package, and operating in single mode of wavelength of 514.5 nm, was employed. As shown in Fig. 2.3, the vertically-polarized laser beam is split into two perpendicular beams. One beam, which serves as the reference beam, strikes a diffuser (D) and then is reflected into the Fabry-Pérot interferometer through pinhole P2. The other split beam is directed at the sample through a stepped filter which is used to attenuate the laser incident power. The beam is reflected by a small mirror (M) with diameter of 6 mm and then focused by lens L1 onto the sample as the excitation source. A stream of pure argon gas was directed onto the sample surface to cool it and to keep air away from it. Lens L1 also functions as a collection lens for the scattered light. The collected light is then refocused by lens L2 into pinhole P1 of the interferometer. In this thesis, all Brillouin measurements were performed at room temperature.

Multi-pass tandem Fabry-Pérot interferometer

The (3+3)-pass tandem Fabry-Pérot interferometer was obtained from JRS Scientific Instruments [7, 8]. A typical FP interferometer consists of two plane mirrors mounted parallel to one another, with an optical spacing L between them. The light with wavelength λ is transmitted only if $L = n\lambda/2$, with n being an integer, as shown in Fig. 2.4. The spacing $\Delta\lambda$ between two neighboring transmission maxima is called free spectral range (FSR) and can be expressed in terms of frequency:

$$f_{\mathrm{FSR}} = c/2L = [150/L\ (\mathrm{mm})]\ \mathrm{GHz}, \tag{2.7}$$

where c is the velocity of light in vacuum. The finesse (F) of the FP interferometer is related to the line width of a given transmission peak by:

$$F = \frac{\Delta\lambda}{\delta\lambda}\ . \tag{2.8}$$

The transmitted intensity is given by the Airy function T:

$$T(\frac{L}{\lambda}) = \frac{T_0}{1 + 4\frac{F^2}{\pi^2}\sin^2(\frac{2\pi L}{\lambda})}, \tag{2.9}$$

where T_0 (< 1) is the maximum transmission determined by the system.

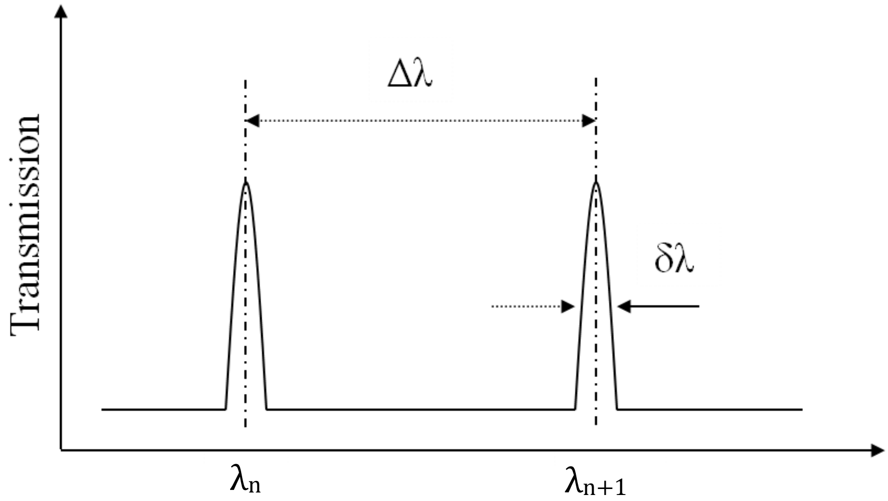

Fig. 2.4 Illustration of the transmission versus wavelength of FP interferometer.

An explicit and clear interpretation of the frequency spectrum is not possible because high transmission orders exist in the transmission spectra of a single FP interferometer which would cause the spectra overlapping. A tandem FP interferometer which has two interferometers in series can solve the problem of spectra overlapping. A diagram of the tandem FP interferometer system is shown in Fig. 2.5. The FP interferometer 1 (FP1) lies in the direction of the translation stage movement, with one mirror on the translation stage and the other on a separate angular orientation device. The FP interferometer 2 (FP2) lies with its axis at an angle θ to the movement direction, with one mirror on the translation stage in proximity to the mirror of FP1, and the other mirror on an angular orientation device. The spacing of two mirrors is L_1 for FP1 and L_2 for FP2. The changes in FP1 δL_1 and in FP2 δL_2 satisfy the synchronization condition:

$$\delta L_1 / \delta L_2 = L_1 / L_2 \tag{2.10}$$

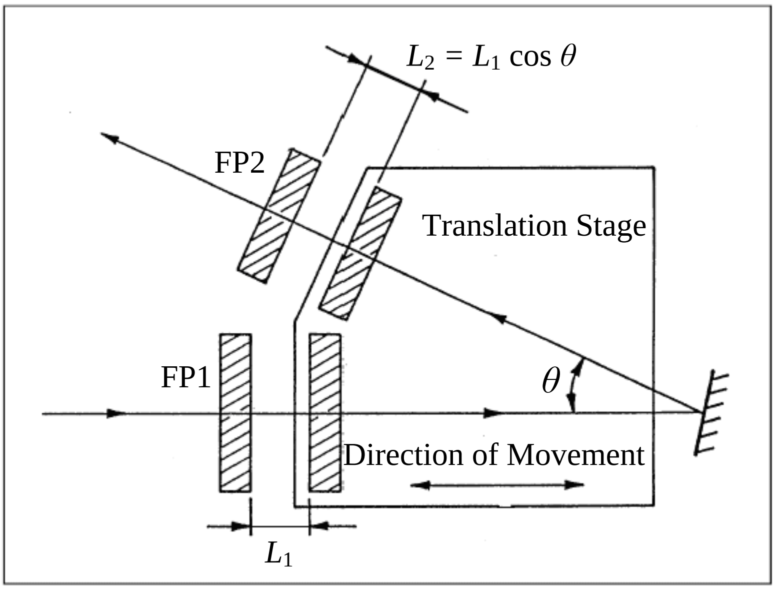

Fig. 2.5 Translation stage allowing automatic synchronization scans of the Fabry-Pérot tandem interferometer.

The two interferometers are arranged in a parallelogram construction which can achieve both statically and dynamically stable synchronization. The optical arrangement in the tandem mode is schematically shown in Fig. 2.6. It can be seen that the scattered light enters the system through the adjustable pinhole P1, and then passes both FP1 and FP2 three times, and finally reaches the output pinhole P3. The advantages of the six-pass tandem FP interferometer are numerous and they include tilt-free scan, high linear scan, continuous change and measurement of mirror spacing, ability to change the mirror spacing moderately without losing alignment, higher contrast and larger effective FSR (10 to 300 GHz).

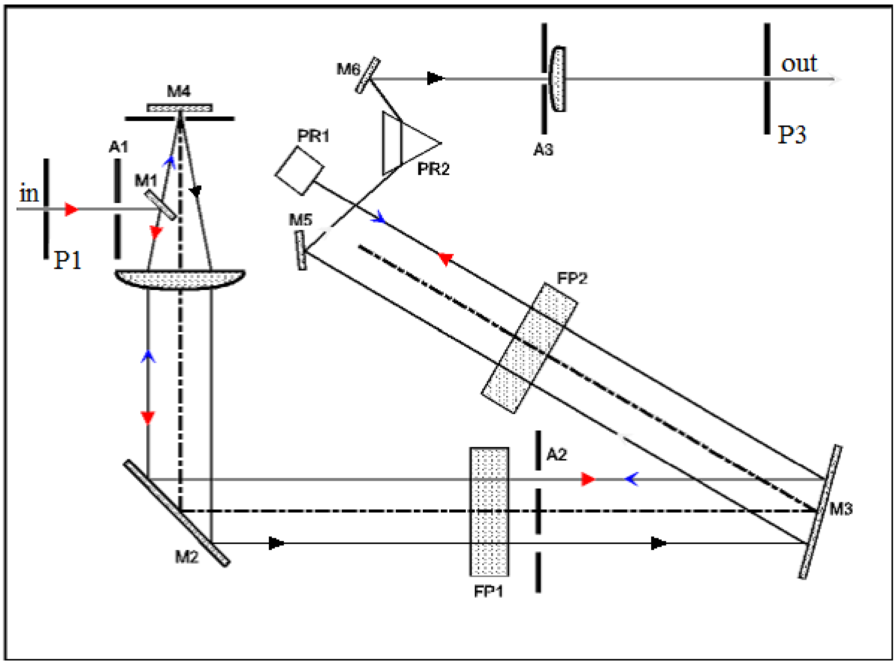

Fig. 2.6 A schematic of the optical arrangement in tandem mode.

Photon detector

The FP interferometer is connected to a highly sensitive single photon counting module, Model SPCM-AQR-16 from EG&G, by which the photons pulses are collected and displayed as spectra on a monitor. This detector is very sensitive to photons of wavelength ranging from 400 to 1600 nm, and its quantum efficiency is slightly over 60% around 500 nm. In addition, the detector utilizes a silicon avalanche photodiode which is both thermoelectrically cooled and temperature controlled, ensuring a stable performance despite changes in the ambient temperature.

2.4 Micro-Brillouin setup

A micro-Brillouin system was used in the study of eigenvibrations of nanoparticles. Fig. 2.7 shows a photo of the micro-Brillouin system. A DM/LM

Leica microscope is modified for the observation of the tiny samples. The constructions of the modified microscope are displayed in Fig. 2.8. The optical arrangement of the micro-Brillouin system is schematically illustrated in Fig. 2.9. In this figure, the incident laser light (red lines) is reflected by a tiny mirror (2 mm × 3 mm) and then focused onto the sample. The objective lens functions as both the focusing and collection lens. The scattered light collected (blue lines) is sent via a periscope to a focusing lens which focuses the scattered light into pinhole P1 of the FP interferometer. A CCD camera connected to the microscope displays the real-time image of the samples on a monitor.

Fig. 2.7 Photo of micro-Brillouin light scattering setup.

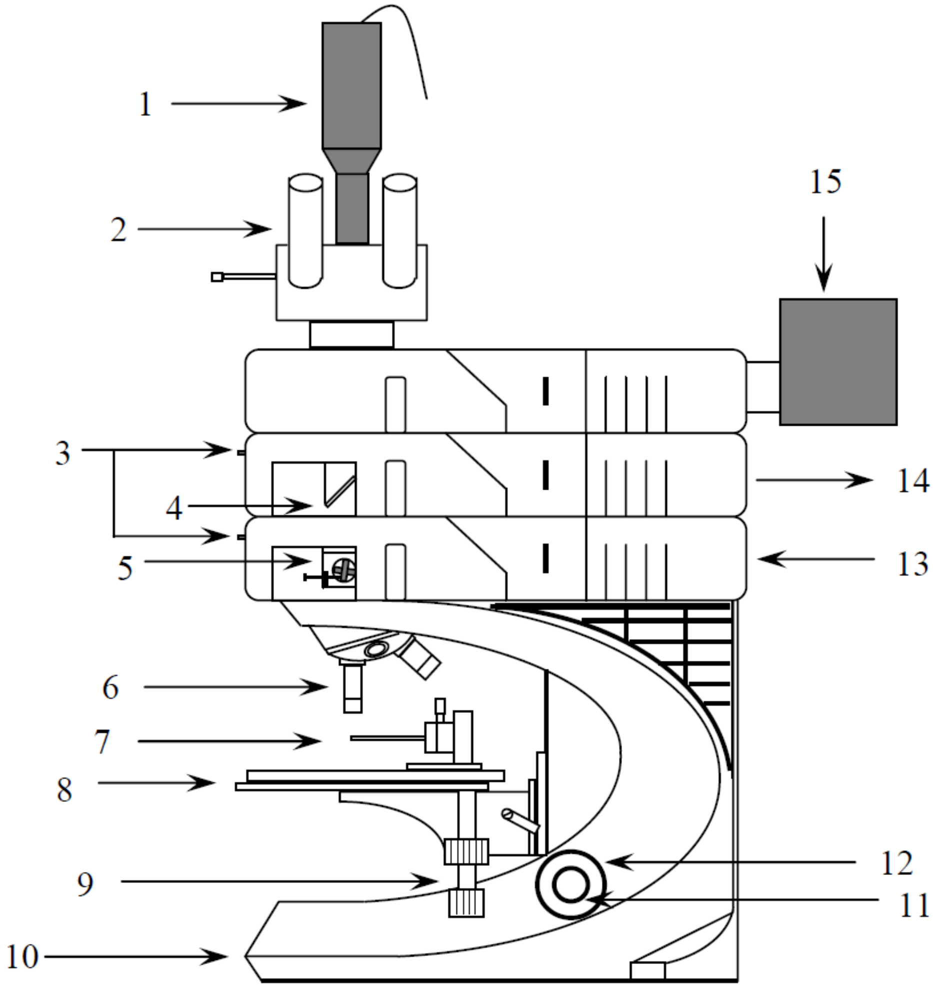

1. CCD Camera
2. Eyepiece
3. Turrets for rotating 4 and 5
4. Mirror for reflecting the scattered light
5. Brass housing & tiny mirror
6. Objective lenses (Magnification: 10X, 20X, 50X and 100X)
7. Sample holder
8. Translation stage
9. X-Y stage adjustment knob
10. Base
11. Fine focusing knob
12. Coarse focusing knob
13. Entrance for incident light
14. Outlet for scattered light
15. Halogen lamp housing

Fig. 2.8 Modified microscope for Brillouin light scattering from nanoparticles.

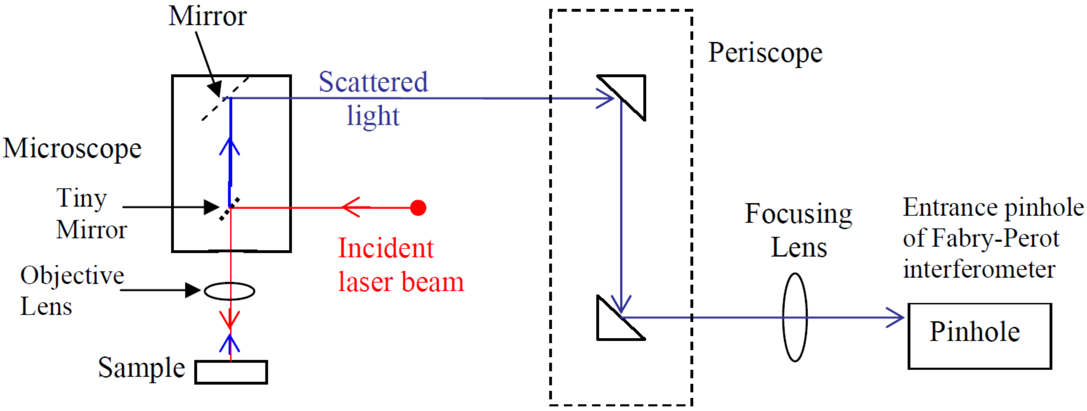

Fig. 2.9 A schematic diagram of the optical components.

This micro-Brillouin system is particularly useful for the study of confined phonons in single nanoparticle. Li *et al.* (2006) has succeeded in recording the Brillouin spectrum of a single SiO_2 sphere with diameter of only 260 nm [9]. It is noteworthy that 260 nm is only half of the laser wavelength. The feasibility of recording Brillouin spectra from a single particle as tiny as this further enhances the capabilities of BLS as a powerful experimental tool.

References:

1. L. Brillouin, Ann. Phys. (Paris), **17**, 88 (1922).

2. L. I. Mandelshtam, Zh. Russ. Fiz. Khim. Ova. **58**, 381 (1926).

3. E. Gross, Nature, **126**, 201 (1930).

4. R. Loudon, Phys. Rev. Lett. **40**, 581 (1978).

5. V. Bortolani, F. Nizzoli, and G, Santoro, Phys. Rev. A **68**, 342 (1978).

6. K. R. Subbaswamy and A. A. Maradudin, Phys. Rev. B **18**, 4181 (1978).

7. J. R. Sandercock, “The design and use of a stabilized mutipass interferometer of high contrast ratio”, *Proc. 2nd Int. Conf. on Light Scattering in Solids*, ed. M Balkanski (Flammarion, Paris, 1971).

8. J. R. Sandercock, Solid State Commun. **26**, 547 (1978).

9. Y. Li, H. S. Lim, S. C. Ng, Z. K. Wang, M. H. Kuok, E. Vekris, V. Kitaev, F. C. Peiris, and G. A. Ozin, Appl. Phys. Lett. **88**, 023112 (2006).

Chapter 3 Elasticity Theory in Condensed Matter

In this chapter, some basic theoretical concepts and calculation methods will be introduced. These concepts and methods lay the foundation for the interpretation of the experimental results and are used for the simulations in this thesis. There are three sections in this chapter. In the first section, some fundamental concepts of the theory of elasticity are briefly introduced. This is followed by the derivation of the general equation of motion. Finally, the Brillouin intensity calculation of the eigenmodes of nanoparticles is introduced in the last section.

3.1 Basic concepts in elasticity

Essential concepts in elasticity pertain to the strain and stress tensors and their relationship.

3.1.1 Strain and stress

Consider a solid body undergoing an elastic distortion starting from an initial undistorted equilibrium state. The displacement $\boldsymbol{u}$ of each point in this body, with its original position $\boldsymbol{x} = (x_1, x_2, x_3)$ with respect to a Cartesian coordinate system and its new location $\boldsymbol{x'}$, can be written as

$$\boldsymbol{u} = \boldsymbol{x'} - \boldsymbol{x}. \tag{3.1}$$

The original distance between two infinitesimally adjacent points dl is given by

$$dl^2 = dx_1^2 + dx_2^2 + dx_3^2, \tag{3.2}$$

using the Einstein summation convention, Eq. (3.2) becomes

$$dl^2 = dx_k dx_k;\ k = 1, 2, 3. \tag{3.3}$$

The separation of the points after a deformation

$$dl'^2 = dx_k^{'} dx_k^{'} = \frac{\partial x_k^{'}}{\partial x_i}\frac{\partial x_k^{'}}{\partial x_j} dx_i dx_j\,. \tag{3.4}$$

In the last step, Taylor expansion is used for ***x'***. Then we get

$$dl'^2 - dl^2 = 2\eta_{ij} dx_i dx_j\,, \tag{3.5}$$

where

$$\eta_{ij} = \frac{1}{2}\left(\frac{\partial x_k^{'}}{\partial x_i}\frac{\partial x_k^{'}}{\partial x_j} - \delta_{ij}\right), \tag{3.6}$$

is called the Lagrangian strain, and δ_{ij} is the Kronecker delta. We can express the strain in terms of the displacement field gradients

$$\eta_{ij} = \frac{1}{2}\left(\frac{\partial u_j}{\partial x_i} + \frac{\partial u_i}{\partial x_j} + \frac{\partial u_k}{\partial x_i}\frac{\partial u_k}{\partial x_j}\right). \tag{3.7}$$

As we are dealing with infinitesimal displacements, the second order terms can be neglected. We get the infinitesimal strain

$$\varepsilon_{ij} = \frac{1}{2}\left(\frac{\partial u_i}{\partial x_j} + \frac{\partial u_j}{\partial x_i}\right); \quad i, j = 1, 2, 3. \tag{3.8}$$

It is evident that $\varepsilon_{ij} = \varepsilon_{ji}$, and this symmetry with respect to interchange of indices indicates that there are only six independent components of strain.

Consider an infinitesimal cube centered on the point ***x*** in a medium, the state of stress at point ***x*** is characterized by the forces per unit area acting across the faces of the cube. The nine components of the Cauchy stress tensor $\{\sigma_{ij}\}$ are

$$\sigma_{ij} = \lim_{dA \to 0} \frac{dF_i^j}{dA}; \quad i, j = 1, 2, 3, \tag{3.9}$$

where dF_i^j is the i'th component of the force acting across the surface facing outwards along the x_j direction and dA is the area of that face.

3.1.2 Elastic constants of solids

For an ideal elastic body subjected to infinitesimal stresses and undergoing infinitesimal strains, the components of the stress tensor (σ_{ij}) and strain tensor (ε_{kl}) are linear functions of each other.

$$\sigma_{ij} = c_{ijkl}\,\varepsilon_{kl}\ . \tag{3.10}$$

The elastic behaviour of the material is characterized by the components of the elastic stiffness tensor (c_{ijkl}), which represents a measure of the resistance of the material to elastic deformation, or equivalently those of the compliance tensor (s_{ijkl}), which represents a measure of the ease of elastic deformation of the material.

As both the strain and stress tensors have six independent strain and stress components, the stiffness tensor has thirty-six independent components. This simplification [1] is exploited by replacing each pair of indices $i\ j$ with a single index 1, 2, 3, … 6 as follows:

11 → 1, 22 → 2, 33 → 3, 23 ≡ 32 → 4, 31 ≡ 13 → 5, 12 ≡ 21 → 6.

In a matrix form, the stiffness tensor can be expressed as

$$\begin{pmatrix} C_{11} & C_{12} & C_{13} & C_{14} & C_{15} & C_{16} \\ C_{21} & C_{22} & C_{23} & C_{24} & C_{25} & C_{26} \\ C_{31} & C_{32} & C_{33} & C_{34} & C_{35} & C_{36} \\ C_{41} & C_{42} & C_{43} & C_{44} & C_{45} & C_{46} \\ C_{51} & C_{52} & C_{53} & C_{54} & C_{55} & C_{56} \\ C_{61} & C_{62} & C_{63} & C_{64} & C_{65} & C_{66} \end{pmatrix}. \tag{3.11}$$

As the stiffness matrices are symmetric, only twenty-one stiffness components are actually independent in Hooke's law. The number of independent elastic constants is reduced further by the crystal symmetry. For example, by assuming homogeneity and isotropy, the number of independent elastic constants is reduced further from twenty-one to two

$$\begin{pmatrix} C_{11} & C_{12} & C_{12} & 0 & 0 & 0 \\ C_{12} & C_{11} & C_{12} & 0 & 0 & 0 \\ C_{12} & C_{12} & C_{11} & 0 & 0 & 0 \\ 0 & 0 & 0 & \frac{1}{2}(C_{11}-C_{12}) & 0 & 0 \\ 0 & 0 & 0 & 0 & \frac{1}{2}(C_{11}-C_{12}) & 0 \\ 0 & 0 & 0 & 0 & 0 & \frac{1}{2}(C_{11}-C_{12}) \end{pmatrix}, \tag{3.12}$$

and the elastic constants matrix of a solid with cubic crystal symmetry can be shown as:

$$\begin{pmatrix} C_{11} & C_{12} & C_{12} & 0 & 0 & 0 \\ C_{12} & C_{11} & C_{12} & 0 & 0 & 0 \\ C_{12} & C_{12} & C_{11} & 0 & 0 & 0 \\ 0 & 0 & 0 & C_{44} & 0 & 0 \\ 0 & 0 & 0 & 0 & C_{44} & 0 \\ 0 & 0 & 0 & 0 & 0 & C_{44} \end{pmatrix}. \tag{3.13}$$

In the case of an isotropic solid, as its mechanical properties are the same in all orientations, engineering constants such as Young's modulus (Y), shear modulus (*G*), bulk modulus (*K*), and Poisson's ratio (*v*) are favoured. The Young's modulus and Poisson's ratio are related to the elastic constants as follows:

$$Y = \frac{\left(C_{11} - C_{12}\right)\left(C_{11} + 2C_{12}\right)}{\left(C_{11} + C_{12}\right)}, \tag{3.14}$$

$$\nu = \frac{C_{12}}{C_{11} + C_{12}}. \tag{3.15}$$

3.2 Dynamic motions of an elastic solid

In a uniform stress field and in the absence of body forces and torques, the particles in a solid experience no resultant forces, and hence no accelerations. Accelerated motion is brought about by nonuniformity in the stress field or stress gradient. Consider the two forces in the x_1 direction acting on a small cube of side δx depicted in Figure 3.1. These forces acting across the two faces normal to the x_1 direction are not exactly equal and opposite, since they depend on the stress σ_{11} evaluated at slightly different positions $x_1 = \pm \frac{\delta x}{2}$. They are thus given by

$$\sigma_{11}(x_1 = \pm \delta x) = \sigma_{11}(0) \pm \frac{\partial \sigma_{11}}{\partial x_1} \frac{\delta x}{2}. \tag{3.16}$$

The resultant of these two forces, taking into account the areas δx^2 of the two faces, is $\frac{\partial \sigma_{11}}{\partial x_1} \delta x^3$. Considering the pairs of faces normal to the x_2 and x_3 directions, forces $\frac{\partial \sigma_{12}}{\partial x_2} \delta x^3$ and $\frac{\partial \sigma_{13}}{\partial x_3} \delta x^3$ can be obtained. Therefore, the resultant force in the

x_1 direction is $F_1 = \frac{\partial \sigma_{1j}}{\partial x_j} \delta x^3$, summed over *j* according to the Einstein summation convention [2].

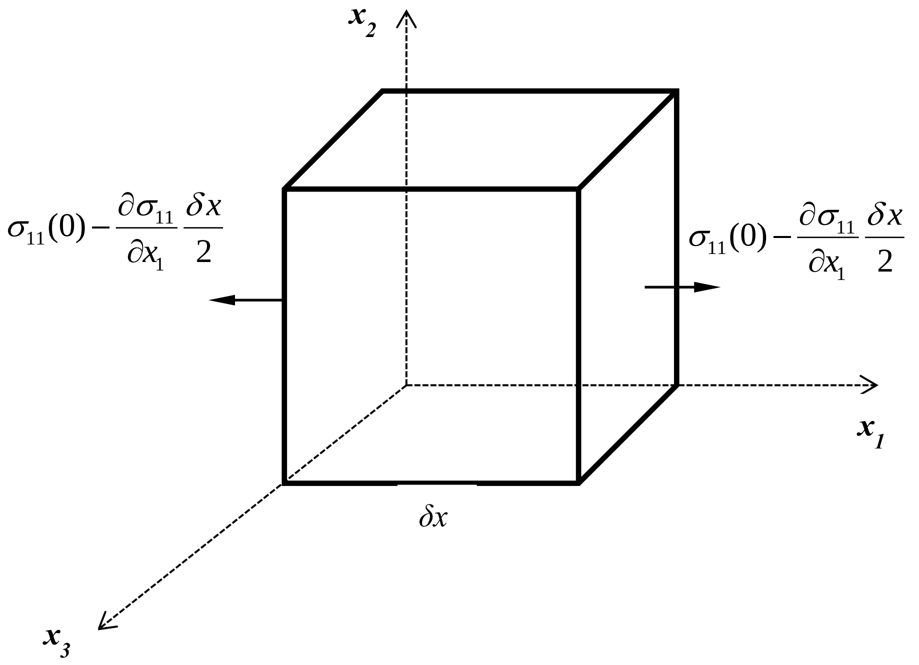

Fig. 3.1 Forces exerted on an infinitesimal cube by the surrounding material in the presence of a stress gradient.

The same argument can be applied to the x_2 and x_3 components of force, and the *i*'th component of the resultant force is therefore

$$\delta F_i = \frac{\partial \sigma_{ij}}{\partial x_j} \delta x^3. \tag{3.17}$$

This force causes acceleration, according to Newton's second law, which is given by

$$\delta F_i = m \frac{\partial^2 u_i}{\partial t^2} = \rho \delta x^3 \frac{\partial^2 u_i}{\partial t^2}, \tag{3.18}$$

where $m = \rho \delta x^3$ is the mass of the cube, ρ is the density. From equations (3.17) and (3.18), it follows that [3,4]

$$\rho \frac{\partial^2 u_i}{\partial t^2} = \frac{\partial \sigma_{ij}}{\partial x_j}. \tag{3.19}$$

Expressing the stress in terms of stress-strain relations (see Eq. (3.1)) and the strain in terms of the displacement field, and making use of the symmetry of the elastic stiffness tensor with respect to interchange of indices, the wave equation can be expressed as

$$\rho \frac{\partial^2 u_i}{\partial t^2} = \frac{\partial}{\partial x_j}(c_{ijkl} \frac{\partial u_k}{\partial x_l}). \tag{3.20}$$

This is the wave equation for a general, even for a heterogeneous solid, in the limit of small displacements. This equation will be used to simulate the eigenmode frequencies of octahedron-shaped gold nanocrystals studied in this thesis.

If the propagation of elastic waves in homogeneous media is considered, Eq. (3.20) can be written as

$$\rho \frac{\partial^2 u_i}{\partial t^2} = c_{ijkl} \frac{\partial^2 u_k}{\partial x_j \partial x_l}. \tag{3.21}$$

The simplest solutions of the above wave equation are plane waves given by the real part of:

$$u_i = U_i \exp[i(\boldsymbol{q} \cdot \boldsymbol{x} - \omega t)], \tag{3.22}$$

where $\boldsymbol{U}$ is the polarization vector, $\boldsymbol{q}$ the wavevector ($|\boldsymbol{q}| = 2\pi / \lambda$, λ is the wavelength), and ω the angular frequency. On substituting into Eq. (3.21), a set of three linear equations relating these quantities results:

$$(c_{ijkl}q_jq_l - \rho\omega^2\delta_{ik})U_k = 0\,. \tag{3.23}$$

In the case of an isotropic solid, it can be, without loss of generality, assumed that the propagation direction is along the x_1 axis, i.e., the only nonzero component of $\boldsymbol{q}$ is $q_1 = q$. Introducing the Lamé coefficients λ and μ:

$$\lambda = C_{12},\ \mu = C_{44}, \text{ and } C_{11} = \lambda + 2\mu. \tag{3.24}$$

Eq. (3.22) becomes:

$$\begin{aligned}
\rho\omega^2U_1 &= (\lambda + 2\mu)q^2U_1,\\
\rho\omega^2U_2 &= \mu q^2U_2,\\
\rho\omega^2U_3 &= \mu q^2U_3.
\end{aligned} \tag{3.25}$$

Here, the displacements in three orthogonal directions are completely uncoupled. Nontrivial solutions take the form of either U_1, U_2 or U_3 being nonzero, and the other two being zero. The mode with U_1 nonzero has its polarization vector parallel to its wavevector and is called the longitudinal mode. The phase velocity of this wave (longitudinal velocity) is

$$V_{\mathrm{L}} = \frac{\omega}{q} = \sqrt{C_{11}/\rho}\,. \tag{3.26}$$

The other two modes have their polarization vectors perpendicular to their wavevector, and are known as transverse modes. They both have the same phase velocity (transverse velocity)

$$V_{\mathrm{T}} = \frac{\omega}{q} = \sqrt{C_{44}/\rho}\,. \tag{3.27}$$

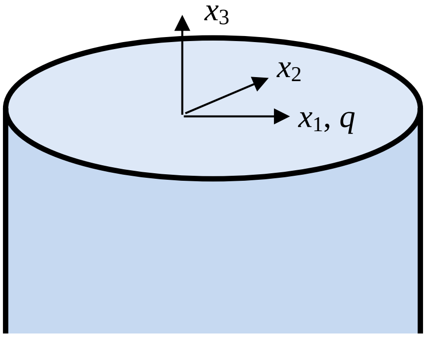

Fig. 3.2 Coordinate system for the surface wave problem.

The solution for Rayleigh waves to Eq. (3.21) is a linear combination of the partial waves of the form

$$u_i = \alpha_i \exp(iqx_3)\exp[iq(x_1 - Vt)]. \tag{3.28}$$

The phase velocity of the Rayleigh wave, V, is measured along the propagation wavevector $\boldsymbol{q}$ (x_1 direction in Fig. 3.2). Conceptually, the x_3-dependence is regarded as part of the "amplitude" of the term and the wave like properties are taken to be contained in the common propagation part of the terms, $\exp[iq(x_1 - Vt)]$. Thus, the propagation vector is always assumed to be parallel to the surface.

To solve the wave equation after substituting Eq. (3.28) to Eq. (3.21), one must consider the boundary conditions [5]: zero-valued stresses at the free surface plane and vanishing of displacement at large depths. In the case of homogeneous isotropic media, the above procedure results in an implicit equation for the velocity of Rayleigh wave [6]

$$\left[2-\left(\frac{V}{V_T}\right)^2\right]^2 = 4\left[1-\left(\frac{V}{V_L}\right)^2\right]^{\frac{1}{2}}\left[1-\left(\frac{V}{V_T}\right)^2\right]^{\frac{1}{2}}, \qquad (3.29)$$

where V_L and V_T are the respective velocities of the longitudinal and transverse bulk wave in the same medium.

3.3 Intensity calculation

Using the finite element analysis, the frequencies of the confined acoustic modes can be calculated for nanoparticles with an arbitrary shape. However, not all the simulated modes are observable in Brillouin light scattering experiments. Identification of the observed modes can be aided by information on their Brillouin scattering intensities. For this reason, the scattering cross-sections of the modes of a gold nano-octahedron have been computed to identify those observed modes with significant Brillouin scattering intensities.

The general equation of the scattering intensity for contribution of the *p*th mode, with frequency ω^p, to the Stokes part of the spectrum for a one-phonon light scattering [7] can be expressed as

$$I^p_{\alpha\beta}(\boldsymbol{q}) \propto \frac{n(\omega^p)+1}{\omega^p}\left|\sum_i e^{-i\boldsymbol{q}\cdot\boldsymbol{x}^i}\left[-i\boldsymbol{q}\cdot\boldsymbol{e}(i,p)\pi^i_{\alpha\beta}+Q^i_{\alpha\beta}\right]\right|^2, \qquad (3.30)$$

where α and β are the respective directions of polarization of the incident and scattered photon, $n(\omega,T)=[\exp(h\omega/kT)-1]^{-1}$ the Bose-Einstein factor, and $\boldsymbol{q}=\boldsymbol{k}_s-\boldsymbol{k}_i$ the exchanged wavevector.

The first term, $\sum_i e^{-i\boldsymbol{q}\cdot x^i}\left[-i\boldsymbol{q}\cdot\boldsymbol{e}(i,p)\pi^i_{\alpha\beta}\right]$, is referred to as the Brillouin term. It describes the polarization fluctuations due to the displacement of the units from their equilibrium position: the density of the microscopic polarization units is modulated by the acoustic vibrations. The second term, $\sum_i e^{-i\boldsymbol{q}\cdot x^i}Q^i_{\alpha\beta}$ is referred to as the Raman term. It is due to two kinds of induced effects. One is the local field changes due to the motion of the surrounding dipoles. The other one is the electronic polarizability changes with the change of the atomic distances.

In a continuum approximation, the equilibrium macroscopic polarizability density tensor $P_{\alpha\beta}(\mathbf{x})$ can be used instead of the microscopic polarizability $\pi^i_{\alpha\beta}$ and the sum in Eq. (3.30) is transformed into a space integral. Furthermore, if the material is homogeneous and isotropic, $P_{\alpha\beta}(\mathbf{x})$ can be expressed as

$$P_{\alpha\beta}(\mathbf{x}) = P\delta_{\alpha\beta}\,. \tag{3.31}$$

Neglecting the Raman term, the Brillouin intensity [8] of the *p*th mode of angular frequency ω_p becomes

$$I_p \propto \frac{1}{\omega_p^2}\left|\int e^{-i\boldsymbol{q}\cdot\boldsymbol{r}}\boldsymbol{q}\cdot\boldsymbol{e}_p dV\right|^2, \tag{3.32}$$

where $\boldsymbol{e}_p$ is the normalized eigenvector, and $\boldsymbol{q}$ the exchanged wavevector. I_p is averaged over various $\boldsymbol{q}$'s ranging from 0 to 0.05 nm^{-1} (= $4\pi n/\lambda$, where n is the refractive index, and λ is the laser wavelength).

As an illustration, we calculated the Brillouin spectrum of silica spheres with diameter of 360 nm using Eq. (3.32). The parameters used are V_L = 3954 m/s,

V_T = 2391 m/s and ρ = 1960 kg/m^3 [9]. The resultant spectrum is shown in Fig. 3.3 together with the BLS data. It can be seen that the agreement between the calculated and experimental spectra is reasonably good.

Equation (3.32) will be used in the next chapter to estimate the Brillouin scattering intensity of eigenmodes of non-spherical gold nanocrystals. The computed size-dependence of frequencies of modes with significant intensities based on this estimation is compared with experimental data, which reveals that experiment accords well with calculations (see Chapter 4).

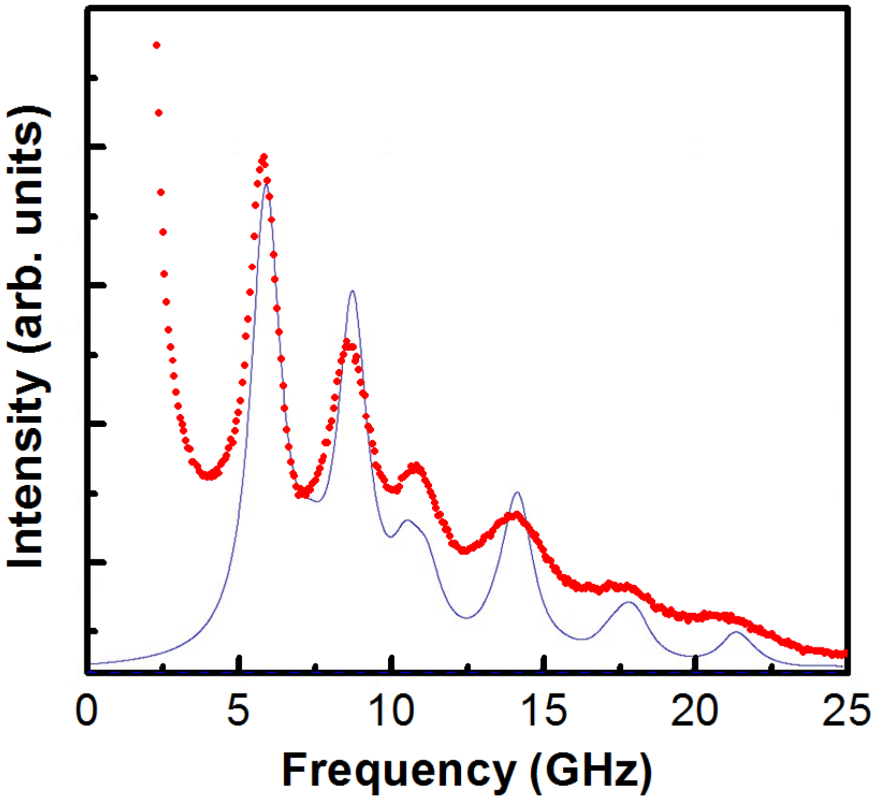

Fig. 3.3 Brillouin spectrum of silica nanospheres of diameter of 360 nm. Experimental data are denoted by dots. Calculated spectrum of 360nm-diameter silica nanospheres using Eq. (3.32) is represented by the solid curve which is the summation of all calculated mode intensities.

References:

1. J. F. Nye, *Physical Properties of Crystals*, (Oxford University Press, London, 1957).

2. M. Levy, H. E. Bass, and Richard R. Stern, *Handbook of Elastic Properties of Solids, Liquids, and Gases*, (Academic Press, New York, 2001).

3. L. D. Landau, E. M. Lifshitz, *Theory of Elasticity*, 3rd ed., (Pergamon Press, Oxford England, 1986).

4. A. E. H. Love, *A Treatise on the Mathematical Theory of Elasticity*, 4th ed., (Dover publications, New York, 1944).

5. G. W. Farnell, in *Physical Acoustics*, Edited by W. P. Manson and R. N. Thurston (Academic, New York, 1970), Vol. 6, p. 109.

6. I. A. Viktorov, *Rayleigh and Lamb waves: Theory and Applications* (Plenum, New York, 1967), p. 26.

7. M. Montagna, Phys. Rev. B **77**, 045418 (2008).

8. T. Still, M. Mattarelli, D. Kiefer, G. Fytas, and M. Montagna, J. Phys. Chem. Lett. **1**, 2440 (2010).

9. H. S. Lim, M. H. Kuok, S. C. Ng, Z. K. Wang, Appl. Phys. Lett. **84**, 4182 (2004).

Chapter 4 Hypersonic Confined Eigenvibrations of Gold Nano-octahedra

4.1 Introduction

The acoustic phonon spectrum of nanoparticles, arising from confined phonons, in the gigahertz range, differs from acoustic waves propagating in their corresponding bulk structures because of their low dimensionality. For instance, experiments carried out on nano-sized isotropic spheres reveal that their confined vibrational modes possess distinct frequencies that are inversely proportional to their diameter [1-4]. Such a relationship was predicted by Lamb who analytically established that the modes of an isotropic sphere are classified into two categories, *viz*., spheroidal and torsional modes [5]. It is important to study the confined acoustic phonon modes of nanoparticles for an understanding of the thermal and mechanical properties of these nano-objects. For example, knowledge of the confined vibrational modes of nanoparticles permits the calculation of their properties such as the specific heat due to phonons [6].

Extensive experimental work has been carried out on the acoustic dynamics of free isotropic spherical nanoparticles [1-4,7,8]. In contrast, very few experimental studies of the vibrations of free crystalline non-spherical nanoparticles have been reported [9-12]. Among them are the studies of cube-shaped GeO_2 nanoparticles of hexagonal crystal symmetry by Li *et al.* (2007), and crystalline gold nanorods by Hu *et al.* (2003) [9,10]. Rarer still are experimental works on the dependence of confined phonon mode frequencies of nanoparticles on their size. Such size-dependence measurements entail the fabrication of a series of batches of particles having a range of sizes, with each batch being monodisperse in both size and shape. This stringent requirement is difficult to meet. Very often syntheses would yield products with not only a wide size distribution, but also of various geometric shapes, thus rendering them unsuitable for size-dependence experiments.

Among the types of materials studied, nanoparticles composed of noble metals have been the focus of extensive studies due to their unique properties and numerous applications such as catalysis, surface plasmonics, chemical sensing, bioimaging, and photothermal therapy [12-17]. In this chapter, we study the confined acoustic phonons in single-crystal gold octahedron-shaped nanoparticles having face-centered cubic structure. The fabrication of batches of monodisperse gold octahedra in various sizes ranging from 42 to 120 nm allowed the experimental determination of the dependence of the frequencies of the phonon modes of octahedron-shaped objects on their size. The nondestructive and noncontact technique of Brillouin light scattering (BLS) was employed, as it is an excellent tool for detecting vibrational modes of nanostructures in the gigahertz frequency range [1-4,7-9,18-20]. The frequencies and displacement profiles of these modes were also evaluated using numerical simulations based on the finite element approach. To aid in the identification of the observed Brillouin peaks, the scattering cross-sections of the modes were also estimated.

4.2 Sample fabrication and BLS measurements

A series of aggregates of high-quality gold octahedra with respective mean edge lengths l = 42, 55, 78, 81, 84, 90, 99 and 120 nm was synthesized following the procedure detailed in Ref. 14. These samples were designed by us and fabricated by Assistant Professor Lu Xianmao of the Department of Chemical and Biomolecular Engineering, National University of Singapore. The fabrication procedure is described below.

Materials used for fabrication

Ethylene glycol (EG, Sigma-Aldrich), chloroauric acid trihydrate ($HAuCl_4 \cdot 3H_2O$, Alfa Aesa), poly(diallyldimethylammonium chloride) solution (PDDA, 20 wt% in H_2O, MW = 200 000-350 000, Aldrich) and hydrochloric acid (HCl, 37%, Merck) were used as received without any further purification. The water used throughout this work was 18.2 MΩ ultrapure deionized water.

Synthesis of Au octahedra

Gold octahedra were prepared using a PDDA-mediated polyol process as follows:

In a typical reaction, 0.2 mL of 20% PDDA solution and 10 mL of EG were well mixed in a glass vial. To this mixture, 10 μL of $HAuCl_4$ aqueous solution (0.5 M) and a given volume of 0.5 M HCl were then added before the vial was capped and placed in an oil bath. The volumes of HCl solution were 200, 50, 25, 10 and 5 μL for the syntheses of 120, 99, 90, 84 and 80 nm Au octahedra, respectively. The reaction was allowed to continue for 30 min at 195 ℃ under vigorous stirring.

Afterwards, the Au particles were precipitated from EG using 10 ml of acetone with centrifugation at 10000 rpm for 10 min, followed by washing with water for five times (9000 rpm, 10 min). For 78, 55 and 42 nm Au octahedra, the reactions were carried out without adding HCl for 30, 15 and 10 min, respectively. The concentrations of the reactants and reaction times are also listed in Table 4.1.

Table 4.1 Synthesis data of Au nano-octahedra.

Octahedra edge length (nm)	**$HAuCl_4$ (M)**	**HCl (M)**	**Additional HCl (μL)**	**Reaction time (min)**
120	0.5	0.5	200	30
99	0.5	0.5	50	30
90	0.5	0.5	25	30
84	0.5	0.5	10	30
80	0.5	0.5	5	30
78	0.5	0.5	0	30
55	0.5	0.5	0	15
42	0.5	0.5	0	10

Size determination and characterizations of Au nano-octahedra

The particle sizes were determined by field-emission scanning electron microscopy (SEM) and transmission electron microscopy (TEM). The size polydispersity for each batch is only ~ 4%. A typical SEM image of the 78 nm octahedra and a TEM image of 120 nm octahedra, shown in Fig. 4.1 and 4.2 respectively, reveal that the resulting particles are monodisperse and have a well-defined octahedral crystal habit. Selected area electron diffraction (SAED) patterns taken of single gold particles, such as the one shown in Fig. 4.3 from the [111] zone axis, indicate that the particles are single-crystals.

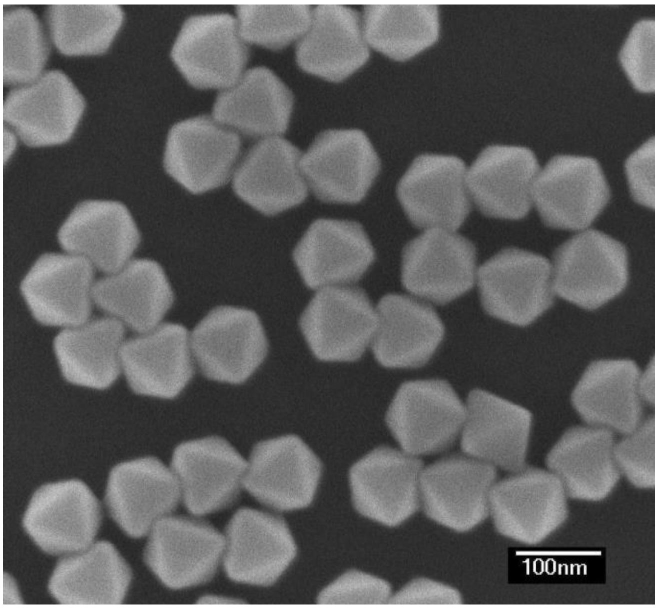

Fig. 4.1 SEM image of gold octahedral nanoparticles with mean edge length *l* = 78 nm.

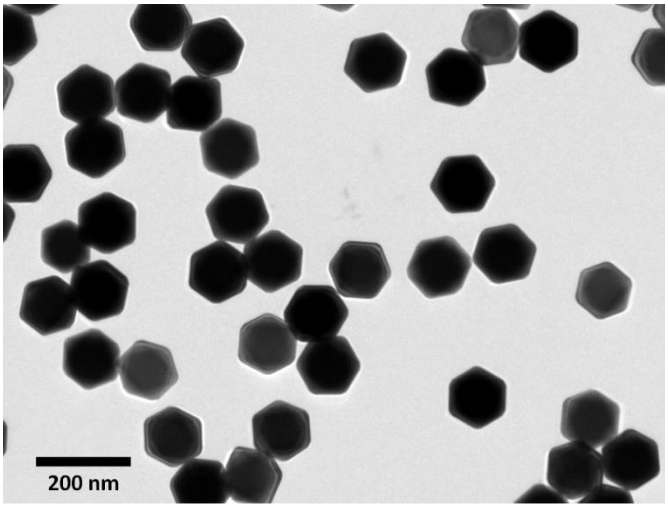

Fig. 4.2 TEM image of gold octahedral nanoparticles with mean edge length *l* = 120 nm.

Preparation of samples for Brillouin study

The gold octahedral nanoparticles came in water suspensions. Prior to the Brillouin measurements, various aggregates of loose gold nano-octahedra were prepared by eye dropping colloidal solutions of the nanoparticles onto respective clean pieces of silicon wafers. This is followed by vacuum drying for several hours at room temperature.

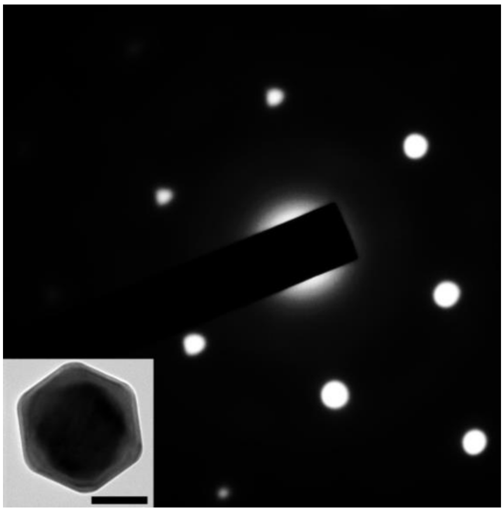

Fig. 4.3 SAED pattern of an *l* = 120 nm gold octahedron. The inset shows its TEM image, with the scale bar representing 50 nm.

Brillouin measurements

The phonon spectra of the gold nanoparticles were recorded by a micro-Brillouin system whose major components were an argon-ion laser, and a six-pass tandem Fabry-Pérot interferometer which was equipped with a silicon avalanche diode detector, and optically interfaced to a modified DM/LM Leica microscope (see Chapter 2). The 180°-backscattering geometry was employed, with a microscope ×10 objective lens serving as both the focusing and collection lens. A CCD camera, attached to the microscope, allowed the viewing of the samples under study. Spectra were excited with the 514.5 nm radiation, with the laser power incident on the samples limited to just a few milliwatts to prevent damage due to overheating. The free spectral range was chosen to be 60 GHz for the particle sizes ranging from 42 to 80 nm, 40 GHz for 84 to 99 nm, and 30 GHz for 120 nm. The measured Brillouin spectrum of these eigenmodes of nanoparticles is independent of the laser incident angle. As the inelastic scattering from the samples was weak, each spectral scan typically lasted 20 hours.

Fig. 4.4 An optical microscope image (×10 magnification) displayed on a monitor, of an aggregate of octahedral particles, with a mean edge length of *l* = 78 nm, illuminated by white light. The microscope is optically interfaced with the BLS system. The gold particles appear as yellow regions, while the other regions represent the exposed silicon wafer which served as the sample holder.

A typical optical microscope image of the sample of 78 nm octahedra is shown in Fig. 4.4. The red circle indicates the spot where the laser light irradiated on the sample. The exact location of the laser spot on the sample was noted so that the same spot can be imaged using SEM. SEM images of the gold particles, of mean edge lengths larger than 70 nm, recorded after the Brillouin measurements confirmed the absence of geometric shape deformation due to laser heating. In contrast, the SEM images taken from 42 and 55 nm Au nanoparticles reveal that they have melted and their shape deformation, due to laser heating at laser powers as low as 1 mW, is quite obvious. Because of their severe shape deformation, it is not possible to obtain proper BLS spectra of the confined vibrational modes. Figure 4.5 shows the SEM images of the 42 nm gold octahedra exposed under different laser powers for 10 min.

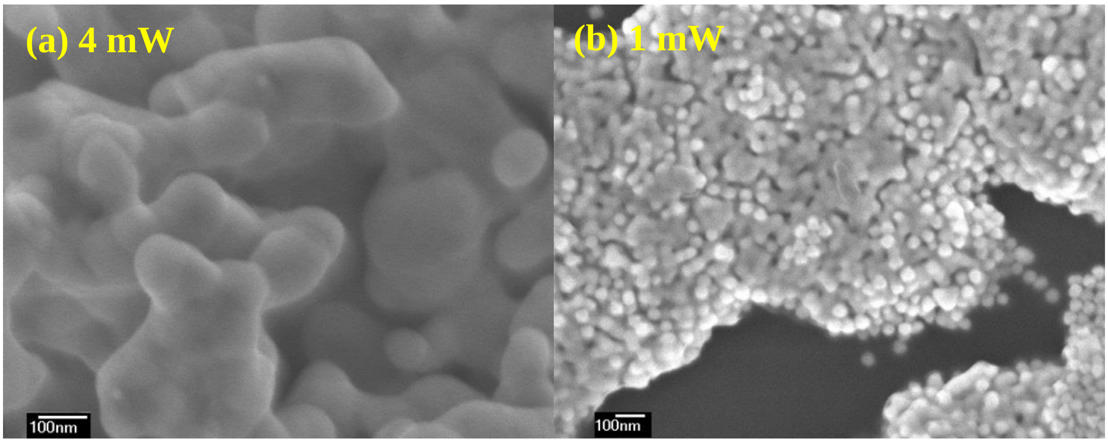

Fig. 4.5 SEM images of l = 42 nm gold octahedra recorded after 10 min laser exposure under laser powers of (a) 4 mW and (b) 1 mW.

4.3 Results and discussions

Experimental results

Figure 4.6 shows respective Brillouin spectra of gold octahedra of mean edge lengths 78 – 120 nm. All spectra recorded were fitted with Lorentzian functions (dashed curves).

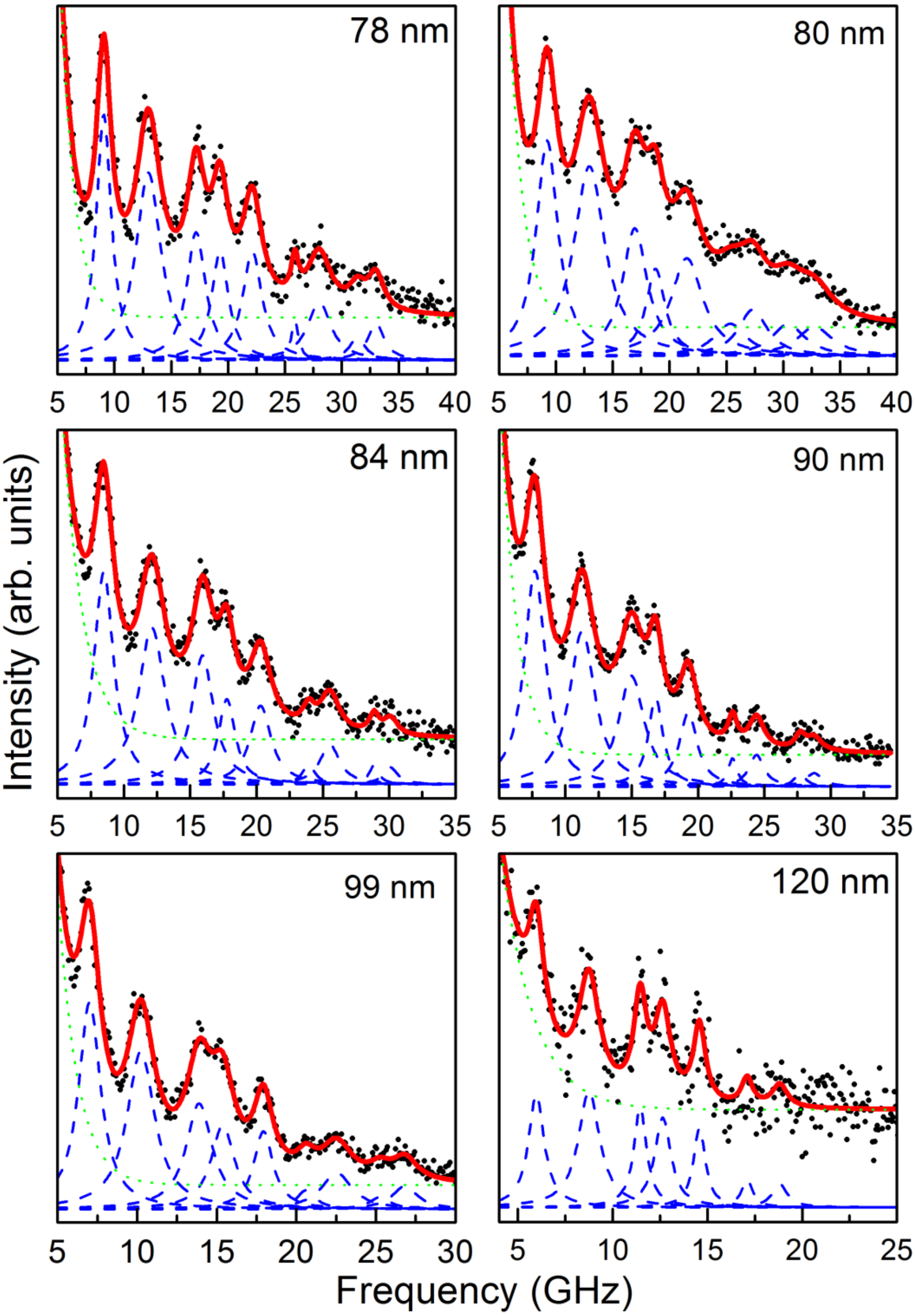

Fig. 4.6 Brillouin spectra of six batches of gold octahedra of sizes *l* = 78 – 120 nm. Experimental data are denoted by dots. The spectrum is fitted with Lorentzian functions (dashed curves) and a background (dotted curves), while the resultant fitted spectrum is shown as a solid curve.

Each spectrum features up to nine well-resolved peaks lying below 35 GHz whose intensities, in general, progressively decrease with frequency, characteristic of the confined acoustic modes of a nano-object [1-4,9]. The measured peak frequencies were plotted as a function of inverse octahedron diagonal ($=\sqrt{2}l$, where l is the octahedron edge length) in Fig. 4.7, which reveals that the peak frequencies are blue shifted with decreasing particle size.

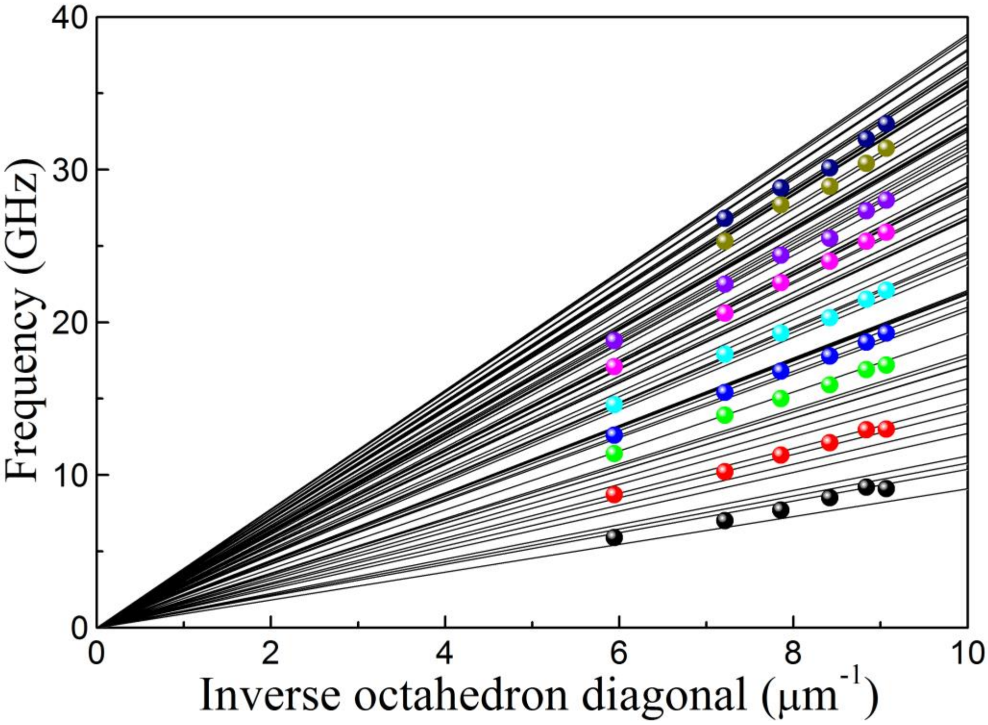

Fig. 4.7 Dependence of measured and calculated vibrational mode frequencies of single-crystal gold nano-octahedra on inverse octahedron diagonal. Experimental data are denoted by dots, while calculated data are represented by solid lines.

Calculation of eigenmode frequencies

The vibrational eigenmodes of an object can be numerically calculated from the following equation:

$$\rho \frac{\partial^2 u_j}{\partial t^2} = \frac{\partial}{\partial x_i}\left(C_{ikjl} \frac{\partial u_k}{\partial x_l} \right), \tag{4.1}$$

where $\boldsymbol{u}(\boldsymbol{x}, t)$ is the displacement field of an elastic medium, C_{ikjl} the elastic tensor, and ρ the mass density. The values of the three independent elastic constants and density used in the calculations, for the gold nanocrystals of cubic crystal symmetry, are taken from Ref. 21 for bulk gold crystals, *viz*., C_{11} = 191 GPa, C_{12} = 162 GPa, C_{44} = 42.4 GPa, and ρ = 19.283 g/cm^3. A finite element analysis was performed to solve Eq. (1), with the imposition of stress-free boundary condition at the particle surface, to yield the vibrational modes of a gold octahedron.

The size-dependence of frequencies of the calculated modes is also shown in Fig. 4.7. It is noteworthy that the mode frequencies of experimental Brillouin data scale with inverse octahedron diagonal. The observed Brillouin peaks are thus attributed to eigenvibrations of individual gold nano-octahedra arising from spatial confinement. However, there are more theoretical modes than the measured ones, implying that not all the calculated vibrational modes contribute to the Brillouin spectra.

Brillouin intensity estimation

The scattering cross-sections of the modes were also calculated to identify those modes with significant Brillouin scattering intensities. For this purpose, a simple model based on the following equation [8,22], was used to estimate the intensity of the *p*th mode of angular frequency ω_p,

$$I_p \propto \frac{1}{\omega_p^2} \left| \int e^{-i\boldsymbol{q}\cdot\boldsymbol{r}} \boldsymbol{q} \cdot \boldsymbol{e}_p \, d\boldsymbol{r}^3 \right|^2, \tag{4.2}$$

where $\boldsymbol{e}_p$ is the normalized eigenvector, and $\boldsymbol{q}$ the exchanged wavevector. The integration was taken over the skin depth of the metallic octahedron rather than over its entire volume, and I_p was averaged over various q's ranging from 0 to 0.05 nm^{-1} (= $4\pi n/\lambda$, where n is the refractive index, and λ the laser wavelength).

While Eq. 4.2 is appropriate for isotropic nanospheres, we shall, nevertheless, use it to estimate the scattering intensity of crystalline gold octahedra. As shown in Table 4.2, the lowest and second lowest observed Brillouin peaks, of the 78 nm gold octahedron, with respective frequencies of 9.2 and 13.0 GHz, agree well with the calculated larger intensity modes.

Table 4.2 Calculated mode frequencies and intensities of the ten lowest-energy modes of the 78 nm gold octahedron.

Brillouin peak frequency (GHz)	Calculated mode	
	Frequency (GHz)	Scattering intensity (a. u.)
9.2	8.2	0.2
	9.3	23.9
	9.7	21.2
	10.1	0.0
	11.5	0.0
	12.1	0.0
13.0	12.8	18.7
	13.2	25.6
	14.1	0.0
	14.7	0.0

The size-dependence of selected modes with significant intensities is compared with experimental Brillouin data in Fig. 4.8, which reveals that experiment accords well with simulations. The good agreement between measurements and theory suggests that the elastic constant values of the nanosized gold octahedra studied are comparable to those of bulk crystalline gold structures.

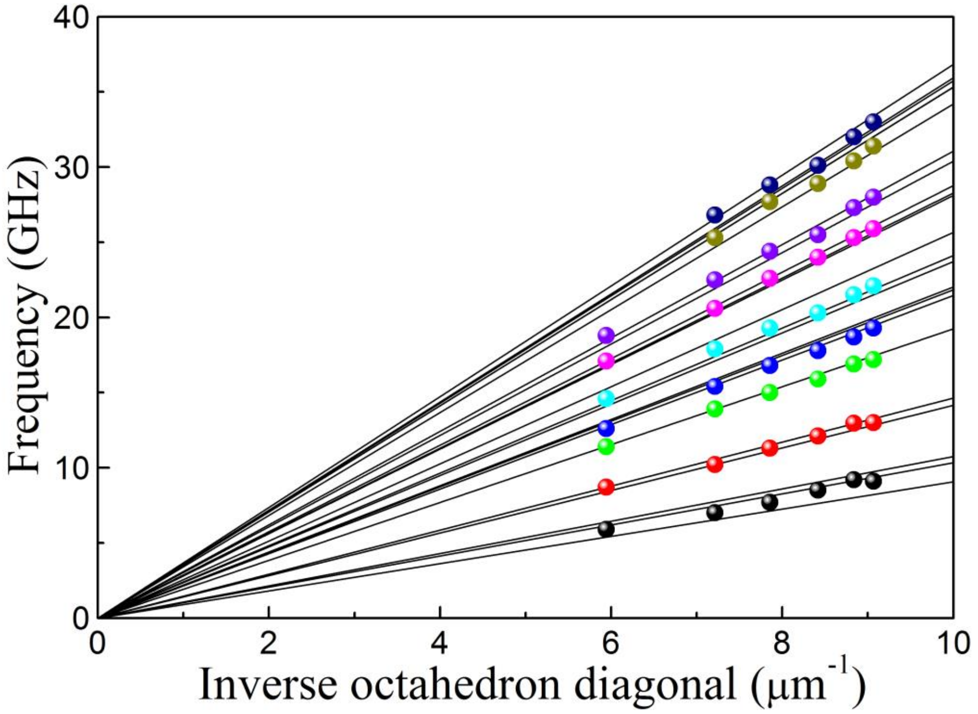

Fig. 4.8 Dependence of measured and calculated vibrational mode frequencies with large scattering intensities of single-crystal gold nano-octahedra on inverse octahedron diagonal.

Discussions

The calculated frequencies of the three lowest-energy modes, which are also among those with larger intensity as shown in Table 4.2, of the 78 nm octahedron are 8.2, 9.3 and 9.7 GHz. Now, its lowest-energy Brillouin peak measured, which has a full width at half maximum (FWHM) of 1.6 GHz, is centered at about 9.1 GHz. This peak is thus a multi-mode one arising from the three aforementioned modes. Similarly, it can be seen from Fig. 4.8, that each measured peak is due to contributions from more than one eigenmode. The proximity of the modes contributing to each peak and the linewidth broadening due to the size polydispersity of the samples preclude the resolution of these separate modes [4].

Multi-mode spectral peaks were also observed by Still *et al*. in their study of isotropic polystyrene and silica nanospheres [8]. Numerical simulations were also performed to determine the displacement profiles of the three modes that contribute to the lowest-energy peak. Simulated profiles of the two maximal displacements for each of these modes, within a cycle of oscillations, are illustrated in Fig. 4.9.

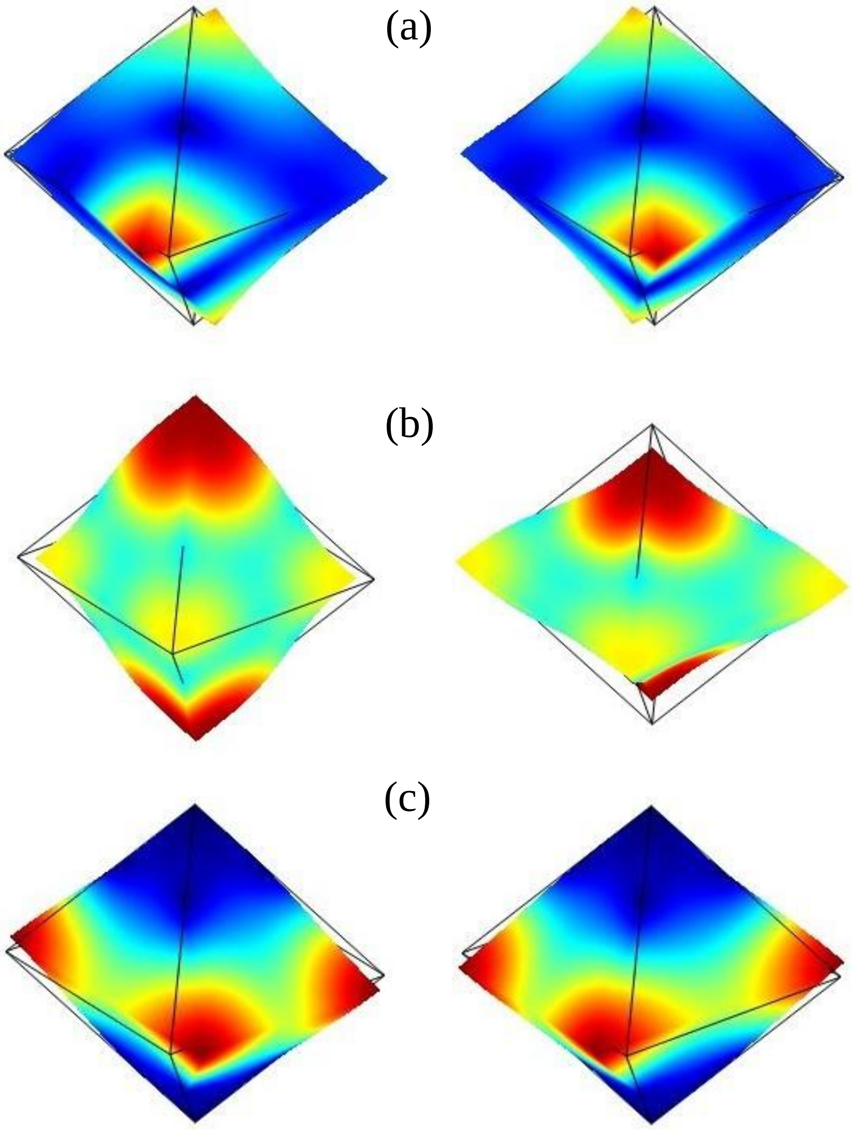

Fig. 4.9 Simulated displacement profiles of (a) the lowest-energy mode, (b) the second lowest-energy mode and (c) the third lowest-energy mode of a gold nano-octahedron of cubic crystal symmetry. For each mode, profiles of its two maximal displacements, within a cycle of oscillations, are presented. The displacement magnitudes are color-coded, with red denoting the maximal value. The outlines of the undeformed octahedra are represented by solid lines.

Aside from the highly symmetrical sphere, no analytical analysis of the confined acoustic vibrations of objects of other geometric shapes has been reported. It is not clear how the size and shape of a non-spherical body would affect its acoustic dynamics. Our results on the size-dependence, together with similar ones reported for spheres and cubes [1-4,9,20], imply that the frequencies of the confined acoustic modes of any free regular-shaped homogeneous object always scale with its inverse linear dimension. Additionally, they suggest that this universal relationship is valid for objects of any size in the classical regime, and is not dependent on other factors such as their elastic properties. These findings would provide guidance to theorists studying the confined acoustic vibrations of such objects. A deviation from linearity was recently reported by Sun *et al.* in their study of cubic Ag core-silica shell nanospheres [19]. However, as these are heterostructures and hence non-homogeneous objects, they are not governed by the above-mentioned universal relationship.

The vibrational modes of our gold octahedra are more complicated than those of isotropic spheres which are either spheroidal or torsional modes. These modes, of a homogeneous free sphere, are classified by their angular momentum l ($l \geq 0$) and its z component m ($-l \leq m \leq l$) which indicates the degree of degeneracy. The number of m values is $2l + 1$, which means these modes are ($2l+1$)-fold degenerate. These eigenmodes, in increasing order of frequency, are also indexed by n [$n \geq 1$, $n = 1$ corresponds to the first harmonic (fundamental mode), $n = 2$ to the second harmonic and so on].

The lowering of spherical symmetry, either by changing the particle shape or its crystallinity (crystal symmetry), would result in the lifting of mode degeneracy, and thus the mode with angular momentum l would split into a maximum of $2l + 1$ components. The eigenvibrations of gold octahedra with cubic crystal symmetry studied in this work generally contain more modes than those of isotropic spheres. However, the gold nanocrystals still exhibit sufficiently high symmetry such that some modes are degenerate. For instance, we found that, from the results of the simulations, the lowest-energy mode of the 78 nm octahedron, with frequency of 8.2 GHz, is two-fold degenerate.

It is of interest to ascertain the trend of mode splitting arising from the lowering of the crystal symmetry [23]. It is possible to track the frequencies of the different modes as the elastic constants progressively vary from those of an isotropic material ($x = 0$) to those for an anisotropic material ($x = 1$):

$$C(x) = (1-x)C^{iso} + xC^{ani}\,;\ 0 \le x \le 1, \tag{4.3}$$

where C^{iso} and C^{ani} are the elastic constants for the isotropic and anisotropic materials. In particular, we calculated the evolution of mode frequencies of a gold sphere of 68 nm in diameter and an octahedron with 78 nm edge length as each of them progressively transforms from an isotopic symmetry to a cubic crystal symmetry.

The elastic constants used for the isotropic gold, *viz.*, C_{11} = 200.7 GPa and C_{12} = 149.7 GPa, is taken from the experimentally fitted ones for polycrystalline gold nano-objects [24]. We refer to the curve representing the variation of a mode frequency as a ‘branch’. It should be noted that such branches are made of fictitious materials except for $x = 1$ and $x = 0$, where the real elastic parameters of the bulk material and experimentally fitted values of polycrystalline gold are used.

The branches of the calculated vibrational modes of the gold sphere corresponding to the lowering of the symmetry in going from the isotropic to the anisotropic case are plotted in Fig. 4.10a, while those of the gold octahedron are plotted in Fig. 4.10b. The figures present the trend of mode splitting due to the lowering of the crystal symmetry. It can also be seen from these figures that the eigenmodes of an octahedron of cubic crystal symmetry are complicated, making the classification of these modes difficult. Further theoretical work should be performed to identify and classify the vibrational modes of non-spherical crystalline particles using group theory, which will make it possible to ascertain the nature of experimentally observed modes.

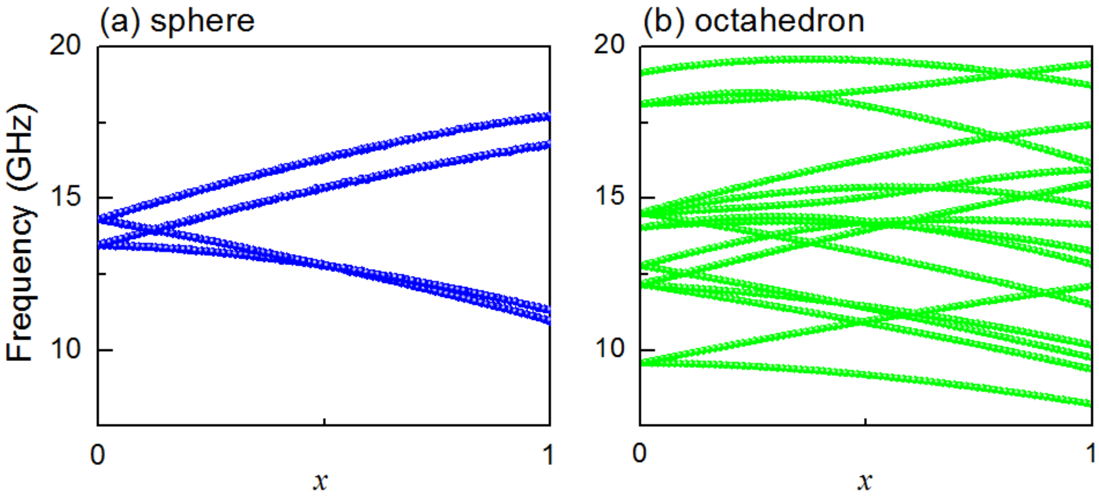

Fig. 4.10 The evolution of the mode frequencies of (a) a gold sphere of diameter of 68 nm and (b) a 78 nm gold octahedron with varying elastic anisotropy.

4.4 Conclusions

In summary, the micro-Brillouin light scattering from a series of high-quality octahedron-shaped gold nanocrystals has been measured. A finite element analysis reveals that the nine peaks observed are due to eigenvibrations of individual nano-octahedra resulting from spatial confinement, with each peak arising from more than one vibrational mode. It is established that the mode frequencies of the gold nanocrystals are inversely proportional to the octahedron diagonal, and that their elastic constants are comparable to those of bulk gold crystals. The findings, together with similar ones reported for spheres and cubes [1-4,9,20], suggest that the frequencies of the confined eigenvibrations of any free regular-shaped homogeneous object always scale with its inverse linear dimension. Additionally, they imply that this universal relationship is valid for such objects of any size in the classical regime, and is not dependent on their elastic properties. These findings would provide guidance to theoretical investigations into the confined acoustic eigenmodes of such objects. Knowledge of confined acoustic modes can be employed in areas such as potential detection of gravitational waves by resonant-mass detectors [25].

References:

1. M. H. Kuok, H. S. Lim, S. C. Ng, N. N. Liu, and Z. K. Wang, Phys. Rev. Lett. **90**, 255502 (2003); **91**, 149901(E) (2003).

2. W. Cheng, J. J. Wang, U. Jonas, W. Steffen, G. Fytas, R. S. Penciu, and E. N. Economou, J. Chem. Phys. **123**, 121104 (2005).

3. H. S. Lim, M. H. Kuok, S. C. Ng, and Z. K. Wang, Appl. Phys. Lett. **84**, 4182 (2004).

4. Y. Li, H. S. Lim, S. C. Ng, Z. K. Wang, M. H. Kuok, E. Vekris, V. Kitaev, F. C. Peiris, and G. A. Ozin, Appl. Phys. Lett. **88**, 023112 (2006).

5. H. Lamb, Proc. London Math. Soc. **13**, 189 (1882).

6. I. -C. Chen, C. -L. Weng, and Y. -C. Tsai, J. Appl. Phys. **103**, 064310 (2008).

7. R. S. Penciu, G. Fytas, E. N. Economou, W. Steffen, and S. N. Yannopoulos, Phys. Rev. Lett. **85**, 4622 (2000).

8. T. Still, M. Mattarelli, D. Kiefer, G. Fytas, and M. Montagna, J. Phys. Chem. Lett. **1**, 2440 (2010).

9. Y. Li, H. S. Lim, S. C. Ng, M. H. Kuok, M. Y. Ge, and J. Z. Jiang, Appl. Phys. Lett. **91**, 093116 (2007).

10. M. Hu, X. Wang, G. V. Hartland, P. Mulvaney, J. P. Juste, and J. E. Sader, J. Am. Chem. Soc. **125**, 14925 (2003).

11. H. Petrova, C. H. Lin, S. de Liejer, M. Hu, J. M. McLellan, A. R. Siekkinen, B. J. Wiley, M. Marquez, Y. N. Xia, J. E. Sader, and G. V. Hartland, J. Chem. Phys. **126**, 094709 (2007).

12. H. Portalès, N. Goubet, L. Saviot, P. Yang, S. Sirotkin, E. Duval, A. Mermet, and M. P. Pileni, ACS Nano **4**, 3489 (2010).

13. M. Pelton, J. E. Sader, J. Burgin, M. Z. Liu, P. Guyot-Sionnest, and D. Gosztola, Nat. Nanotechnol. **4**, 492 (2009).

14. C. C. Li, K. L. Shuford, M. H. Chen, E. J. Lee, and S. O. Cho, ACS Nano **2**, 1760 (2008).

15. D. H. Kim, J. W. Heo, M. J. Kim, Y. W. Lee, and S. W. Han, Chem. Phys. Lett. **468**, 245 (2009).

16. P. K. Jain, K. S. Lee, I. H. El-Sayed, and M. A. El-Sayed, J. Phys. Chem. B **110**, 7238 (2006).

17. E. Hutter, S. Boridy, S. Labrecque, M. Lalancette-Hebert, J. Kriz, F. M. Winnik, and D. Maysinger, ACS Nano **4**, 2595 (2010).

18. T. Still, R. Sainidou, M. Retsch, U. Jonas, P. Spahn, G. P. Hellmann, and G. Fytas, Nano Lett. **8**, 3194 (2008).

19. J. Y. Sun, Z. K. Wang, H. S. Lim, S. C. Ng, M. H. Kuok, T. T. Tran, and X. M. Lu, ACS Nano **4**, 7692 (2010).

20. J. Y. Sun, Z. K. Wang, H. S. Lim, V. L. Zhang, S. C. Ng, M. H. Kuok, W. Zhang, S. Firdoz, and X. M. Lu, Solid State Commun. **152**, 501 (2012).

21. Hearmon, R.F.S., The elastic constants of crystals and other anisotropic materials, in *Landolt-Börnstein Tables*, **III/18**, pp. 1-154, edited by K.H. Hellwege and A.M. Hellwege, Springer-Verlag, Berlin, 559 pp., 1984.

22. M. Montagna, Phys. Rev. B **77**, 045418 (2008).

23. L. Saviot, and D. B. Murray, Phys. Rev. B **79**, 214101 (2009)

24. A. Crut, P. Maioli, N. D. Fatti, and F. Vallee, Phys. Chem. Chem. Phys. **11**, 5882 (2009).

25. M. Bianchi, E. Coccia, C.N. Colacino, V. Fafone, F. Fucito, Class. Quantum Grav. **13**, 2865 (1996).

Chapter 5 Surface Phononic Dispersions in One-dimensional Bi-component Nanostructured Crystals

5.1 Introduction

The propagation of surface acoustic waves is of great importance to both fundamental physics and technology. Although the early research into SAWs is mainly confined to seismological applications, these days it extends to applications such as electro-acoustic devices. As was reviewed in Chapter 1, SAW propagation in periodic patterned films on a substrate has been the subject of increasing interest for their potential applications in microelectronics and SAW phononic-crystal-based devices [1-3]. As stated above, one of the objectives of this project is the study, by Brillouin light scattering, of the surface phononic dispersions of 1D periodic arrays of bi-component nanostripes and 2D arrays of bi-component nanosquares.

The SAW dispersion relation of a film-substrate structure depends on the elastic properties of the film material, the film thickness and the elastic properties of the substrate material. Therefore, for a 1D bi-component phononic structure in the form of a periodic array of alternating nanostripes on a substrate, the SAW dispersion is dependent on the elastic properties of the component materials of the film, the lattice parameters, the filling fraction, the thickness of the film as well as the elastic properties of the substrate. Thus, the frequency bandgap can be tunable by changing any of these parameters.

Two groups of 1D phononic crystals were studied. In this chapter, we will focus on the SAW dispersions of 1D phononic crystals comprised of linear periodic arrays of alternating $Ni_{80}Fe_{20}$ (Permalloy, Py) and Fe (or Ni, Cu) nanostripes on a SiO_2/Si substrate. For brevity, they will be referred to as the Py/Fe, Py/Ni and Py/Cu phononic crystals. The next chapter will discuss the SAW dispersions of 1D periodic arrays of Py and BARC nanostripes on a Si substrate.

5.2 Sample fabrication and BLS measurements

Three nanostructured crystals with the same structure and dimensions were studied. These crystals were designed by us and fabricated by our collaborator Professor Adekunle Olusola Adeyeye of the Department of Electrical and Computer Engineering, National University of Singapore. The fabrication process is described below.

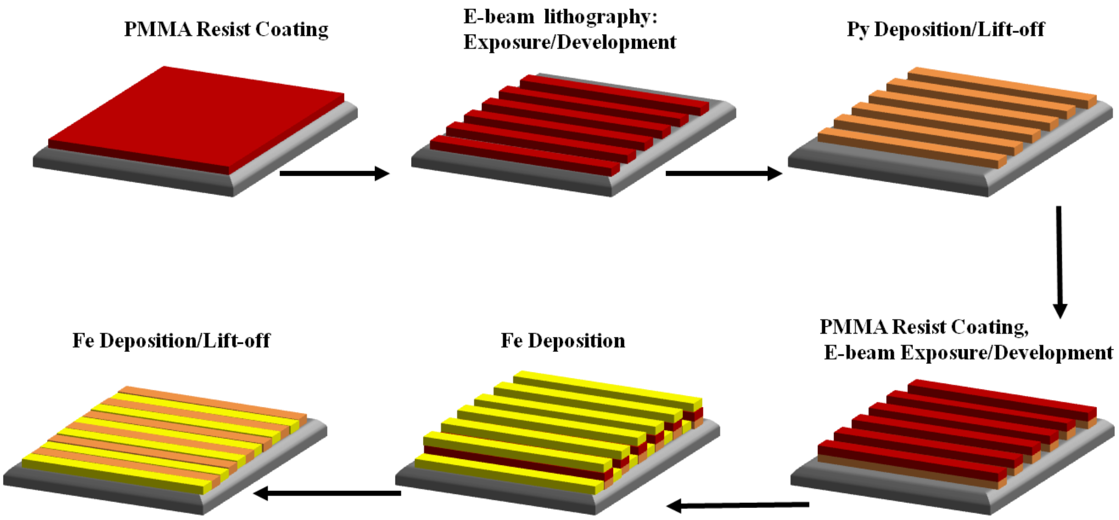

Fig. 5.1 Schematics of fabrication process for 1D nanostructured phononic crystals.

The 30nm-thick 1D periodic array of alternating 250nm-wide Py and Fe (or Ni, Cu) stripes, of lattice constant *a* = 500 nm were fabricated using high-resolution multilevel electron beam lithography (EBL), deposition, and lift-off processes, as depicted in Fig. 5.1 [4]. First, a 120 nm-thick polymethyl methacrylate (PMMA) EBL resist was spin-coated on a SiO_2/Si(001) wafer substrate. The substrate was baked at 180 ^{o}C for 90 s on a hot plate. A 75 kV lithography system (Elionix ELS 7700) with a resist dose of 768 μC/cm^2 was used to pattern the first layer of stripes. Appropriate alignment marks were also patterned for the second stage of lithography process at this stage. After the exposure, a 1:3 solution of methyl isobutyle ketone (MIBK) and isopropyl alcohol (IPA) was used to develop the patterned structure. A 30 nm-thick Py film was then deposited at a rate of 0.12 Å/s on the patterned substrate in an electron beam deposition chamber with a base pressure of 3×10^{-7} torr. After the lift-off process in acetone, the fabricated Py stripes were finished and examined under a JEOL JSM-6700F field emission SEM. The alignment marks fabricated in the first EBL stage were used in exposing the second set of stripes in the gaps between neighboring Py stripes. The fabrication process was then repeated for the deposition of 30 nm-thick iron (or nickel, copper) stripes, followed by a liftoff process. The SEM image of the resulting structures which has a laterally patterned area of 100μm × 100μm is shown in Fig. 5.2.

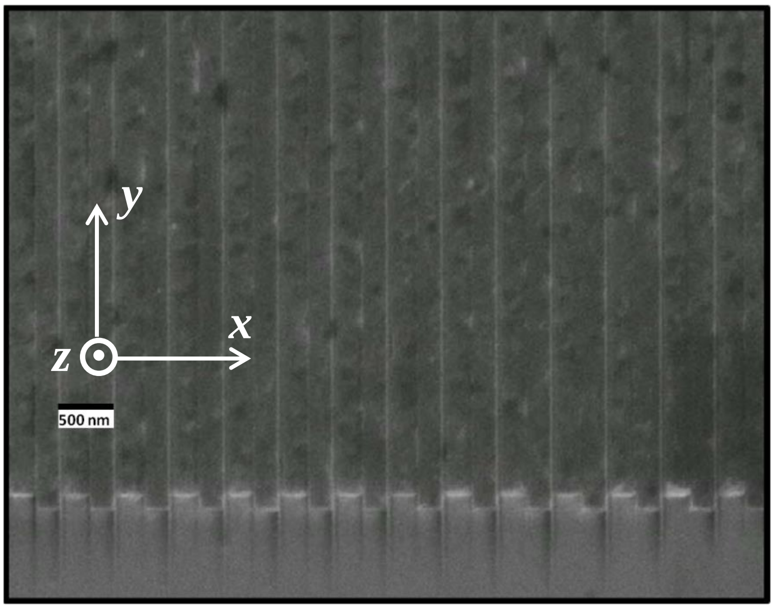

Fig. 5.2 SEM image of the 1D periodic array of alternating Py and Ni nanostripes, each of width 250 nm.

The BLS measurements were performed in the 180°-backscattering geometry, with the scattering plane normal to the sample surface and phonon wavevector ***q*** along the periodicity direction of the phononic crystals (*x* direction in Figs. 5.2 and 5.3). Brillouin spectra of acoustic excitations were recorded in *p*-*p* polarization employing the scattering geometry schematically shown in Fig. 5.3. The dispersion relations were mapped by varying the laser light incidence angle θ to obtain phonon wavevectors q ($= 4\pi\sin\theta/\lambda$, $\lambda = 514.5$ nm) up to the third Brillouin zone (BZ).

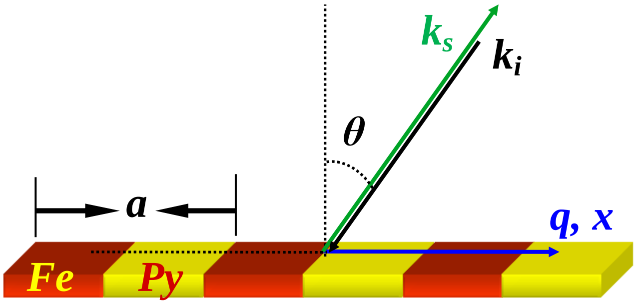

Fig. 5.3 Schematics of Brillouin light scattering geometry showing the light incident angle θ, incident and scattered photon wavevectors $\boldsymbol{k}_i$ and $\boldsymbol{k}_s$, phonon wavevector $\boldsymbol{q}$.

5.3 Experimental results of Py/Fe sample

We will first discuss the experimental results obtained for the Py/Fe sample. Figure 5.4 displays typical *p*-*p* polarization Brillouin spectra recorded at six different q values. We can see that at $q = \pi/a$ and $2\pi/a$ (corresponding to the BZ boundaries), the spectra contain two peaks. For $q = 1.45\pi/a$ and $2.65\pi/a$ (corresponding to the respective second and third BZ), two Brillouin peaks were also observed. Phonon mode frequencies obtained from spectral fits using Lorentzian functions were plotted against wavevector to yield dispersion relations shown in Fig. 5.5. The dispersion relation reveals four phononic forbidden bands (first, second, third and fourth bandgaps with respective widths of 0.4, 0.6, 0.6 and 0.5 GHz).

The dispersion of the unpatterned Py reference film on the same SiO_2/Si substrate was also measured by BLS. Only one peak which corresponds to the surface Rayleigh wave was observed, and the resultant data were plotted in Fig. 5.5 as red open squares.

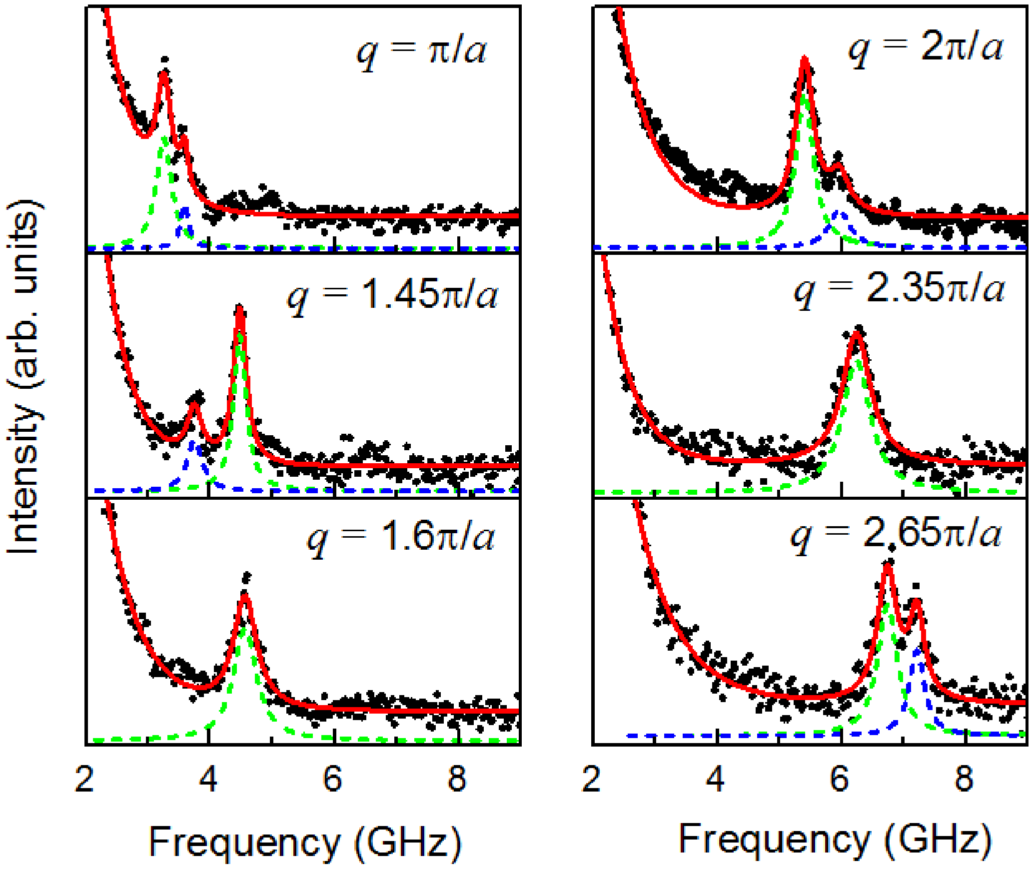

Fig. 5.4 Brillouin *p*-*p* polarization spectra of the Py/Fe phononic crystal measured at various *q*. Spectra were fitted with Lorentzian functions (dashed curves), and the resultant fitted spectra are shown as solid curves.

5.4 Py/Fe sample: simulation results and discussions

Dispersion relations and mode displacement profiles of SAWs propagating in the Py/Fe phononic crystal and the unpatterned reference samples (Py/SiO_2/Si and Fe/SiO_2/Si) were computed within the framework of the finite element approach in COMSOL Multiphysics [5]. To reduce the computational effort, plane-strain approximation is used for the simulation. This approximation assumes that the structure is infinite along one direction (y direction), and the loads are in the x-z plane and are independent of y (i.e. $\frac{\partial}{\partial y} = 0$) which implies that there is no gradient in the displacement along the y direction. We apply periodic boundary conditions as required by the Bloch-Floquet theorem along the x direction,

$$\boldsymbol{u}(x + a) = \boldsymbol{u}(x)e^{iqa} \tag{5.1}$$

where $\boldsymbol{u}$ is the displacement vector.

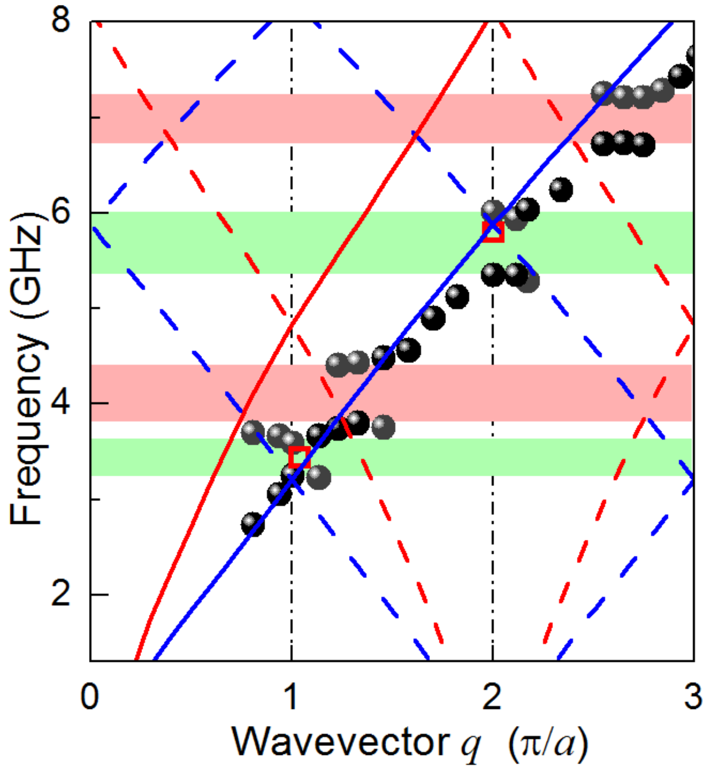

Fig. 5.5 Phonon dispersion relations. Experimental data of Py/Fe phononic crystal are represented by dots. Squares denote the measured Rayleigh mode dispersion on the unpatterned Py/SiO$_2$/Si reference sample. Blue and red solid lines represent the simulated Rayleigh and Sezawa wave dispersions for the reference sample, while blue and red dashed lines their corresponding folded dispersions. Measured Bragg and hybridization bandgaps are represented by green and pink bands respectively, and BZ boundaries by dotted-dashed lines.

We will first discuss the calculated SAW dispersions of the unpatterned reference samples. The computational unit cell shown in Fig. 5.6a comprises a 1D 30nm-thick Py or Fe film in contact with an 800nm-thick silica sub-layer atop a Si substrate with its bottom boundary fixed. The thickness of the Si substrate was set to be five times the wavelength of the surface phonon, as convergence has already been achieved for this value of thickness. For example, the Rayleigh modes frequencies at q = 6.28 µm^{-1} (the wavelength of the phonon is 1 µm) for a Py/SiO2/Si film with a 5µm-thick Si substrate and a 10µm-thick Si substrate, are 3.172388 and 3.172395 GHz respectively.

Parameters used in the numerical calculations for Fe, Py, SiO_2 and the [110] direction of Si(001) surface are Young’s moduli = 211, 180, 73, and 169 GPa, Poisson ratios = 0.29, 0.3, 0.17, and 0.064, mass densities = 7870, 8600, 2200 and 2330 kg/m^3 respectively [6-9]. As the simulated dispersions for both Py/SiO_2/Si and Fe/SiO_2/Si samples are very similar, only the results of Py/SiO_2/Si sample are presented in Fig. 5.5. The blue and red solid lines represent the respective calculated dispersions of the Rayleigh and Sezawa modes of the reference sample, while the blue and red dashed lines, those of their corresponding folded modes. It is to be noted that the measured dispersion of the Rayleigh modes, denoted by squares, agrees well with simulations.

The simulated displacement profiles of the Rayleigh and Sezawa waves are shown in Fig. 5.6b [10]. The mode profiles of the Rayleigh and Sezawa waves clearly show that most of their energy is confined within the Py/SiO_2 film. For these waves, the Py/SiO_2 film therefore behaves as an effective film on a Si substrate.

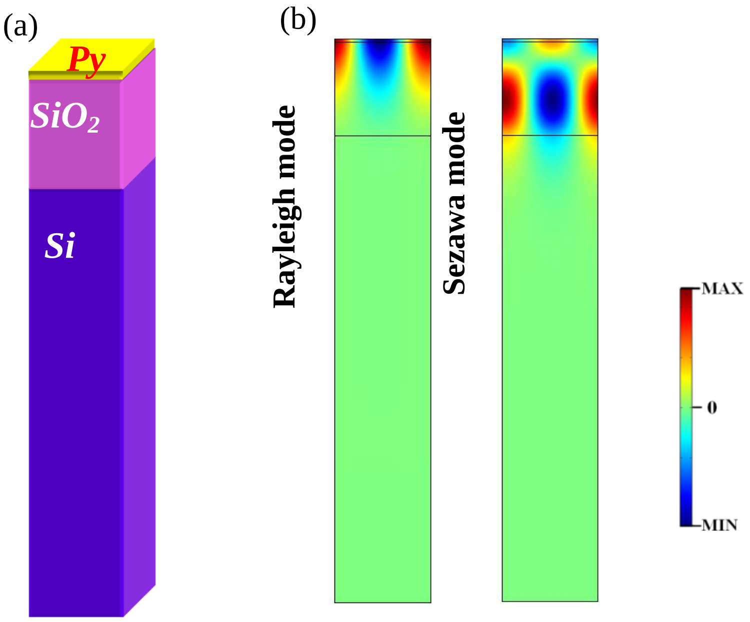

Fig. 5.6 (a) Computational unit cell of the Py reference sample. (b) Displacement profiles of Rayleigh and Sezawa modes of the reference sample. The profiles are color-coded, with red denoting maximal dynamic displacement.

The experimental dispersion relation for the Py/Fe array, represented by dots in Fig. 5.5, generally follows the calculated Rayleigh wave dispersion of the unpatterned reference film. A notable difference is the two gaps at the first and second BZ boundaries and the two gaps within the second and third BZs. The former two gaps at BZ boundaries are Bragg gaps (shown as green bands), whose widths increase with BZ number. They arise from the zone folding of the RW dispersions and avoided crossing at the BZ boundaries [11-13]. These RW modes are standing Bloch waves satisfying the Bragg scattering condition and thus exhibit a non-propagating character.

Interestingly, two additional bandgaps *viz*. hybridization bandgaps (shown as a red band), open up within the second and third BZs at $q \approx 1.3\pi/a$ and $2.7\pi/a$ respectively. As shown in Fig. 5.5, close to these gaps, the Rayleigh wave crosses the zone-folded Sezawa waves. Thus we attribute the origin of these gaps to the hybridization and avoided crossing of the Rayleigh and zone-folded Sezawa modes [12-14].

As for the simulations of the Py/Fe phononic structure, we considered a 1D 30nm-thick periodic array of alternating Fe and Py stripes in contact with an 800nm-thick silica sub-layer atop a 4μm-thick Si substrate (Fig. 5.9a) with its bottom boundary fixed. The top layer of the 500nm-wide cell, as depicted in Fig. 5.7, comprises a 124.5nm-wide Fe stripe, a 249.5nm-wide Py stripe, a 1nm-wide gap, and a 125nm-wide Fe stripe. A gap of width of the order of 1 nm was introduced in the simulations, as misalignment during the two-step lithographic process would result in such a gap at alternate Py/Fe interfaces. Modes with predominant surface displacements were chosen. The simulated phononic dispersion relation, presented in Fig. 5.8**,** captures the features of the Brillouin measured one.

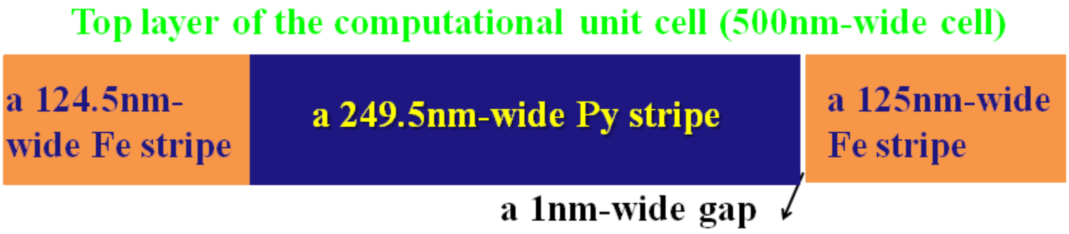

Fig. 5.7 Schematics of the top layer of the computational unit cell.

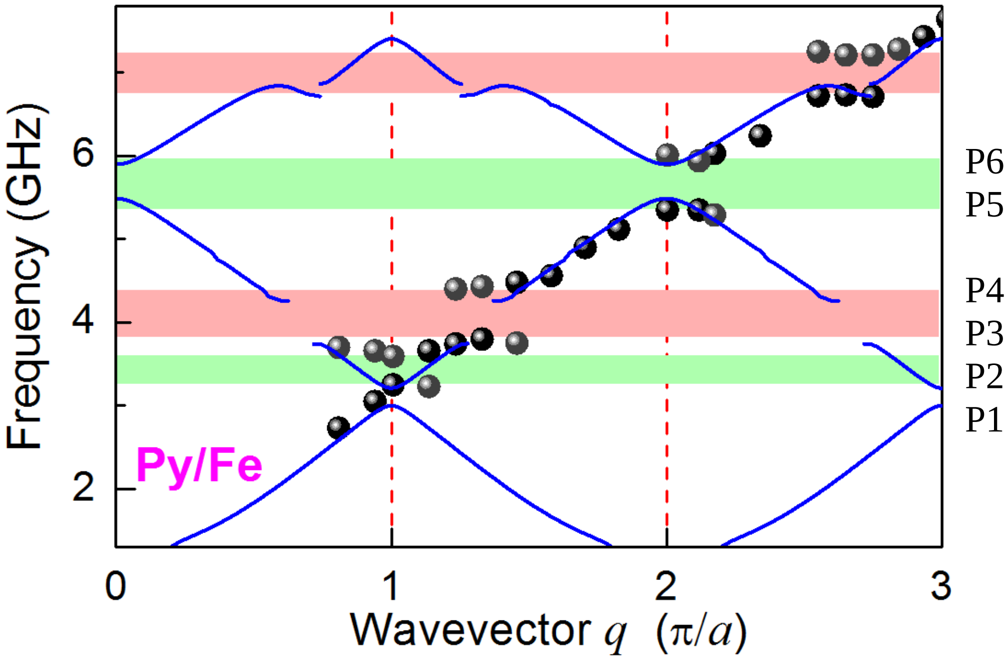

Fig. 5.8 Dispersion relations of surface phonons in the Py/Fe sample. Experimental and theoretical data are denoted by symbols and continuous curves respectively. Measured bandgaps are indicated by shaded bands, and Brillouin zone boundaries by vertical dashed lines. P1 and P2 correspond to the Brillouin peaks measured at $q = \pi/a$, P3 and P4 to the Brillouin peaks measured at $q = 1.3\pi/a$, while P5 and P6 to the Brillouin peaks measured at $q = 2\pi/a$ (see Fig. 5.4).

Mode displacement profiles (vertical displacement, z-component) for $q = \pi/a$, $1.3\pi/a$ and $2\pi/a$ are displayed in Fig. 5.9b. The profiles at two BZ boundaries ($q = \pi/a$ and $2\pi/a$) exhibit characteristics of standing Rayleigh waves. At $q = 1.3\pi/a$, the mode profiles reveal displacement within the Si substrate, thus exhibit bulk wave characteristics indicating that the modes are leaking energy into the substrate due to the mode hybridization.

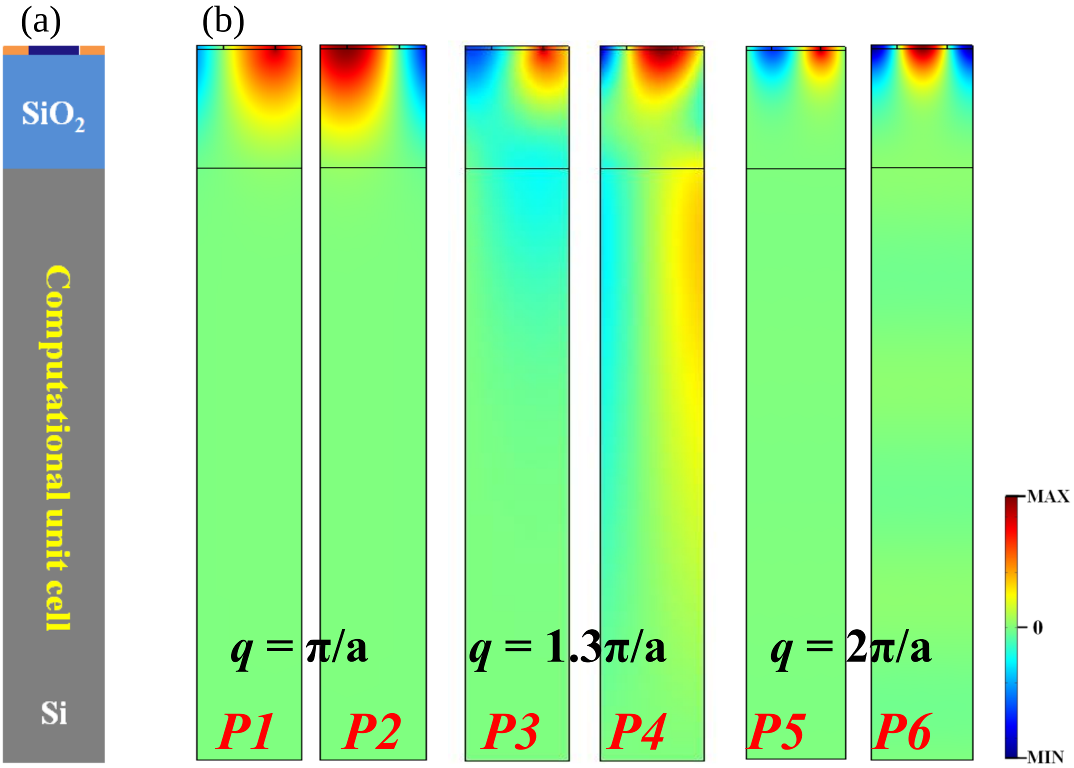

Fig. 5.9 (a) Computational unit cell of the Py/Fe sample, (b) *z*-components of the mode displacement profiles of the observed phonon modes for wavevectors $q = \pi/a$, $1.3\pi/a$ and $2\pi/a$. The profiles are color-coded, with red denoting maximal displacement.

A Rayleigh wave propagating on the surface of a homogeneous film-substrate sample is a pure surface wave, i.e. it does not radiate energy into the substrate. By introducing periodicity on film, the zone-folded Rayleigh dispersion curve which crosses the transverse bulk velocity threshold will leak energy into the substrate [13]. The region above the transverse bulk wave threshold is called the leaky or radiative region [15-16].

5.5 Results of Py/Ni and Py/Cu samples

Typical Brillouin spectra for Py/Ni and Py/Cu samples are shown in Fig. 5.10. Experimental and theoretical dispersion curves for both samples are plotted in Fig. 5.11. The simulations were performed with the same unit cell as that used for the Py/Fe sample. Values of the Young's modulus, Poisson ratio and density of Ni used in the calculations are 186 GPa, 0.29, and 8900 kg/m^3 respectively [18], and those of Cu are 130 GPa, 0.34, and 8960 kg/m^3 respectively [19].

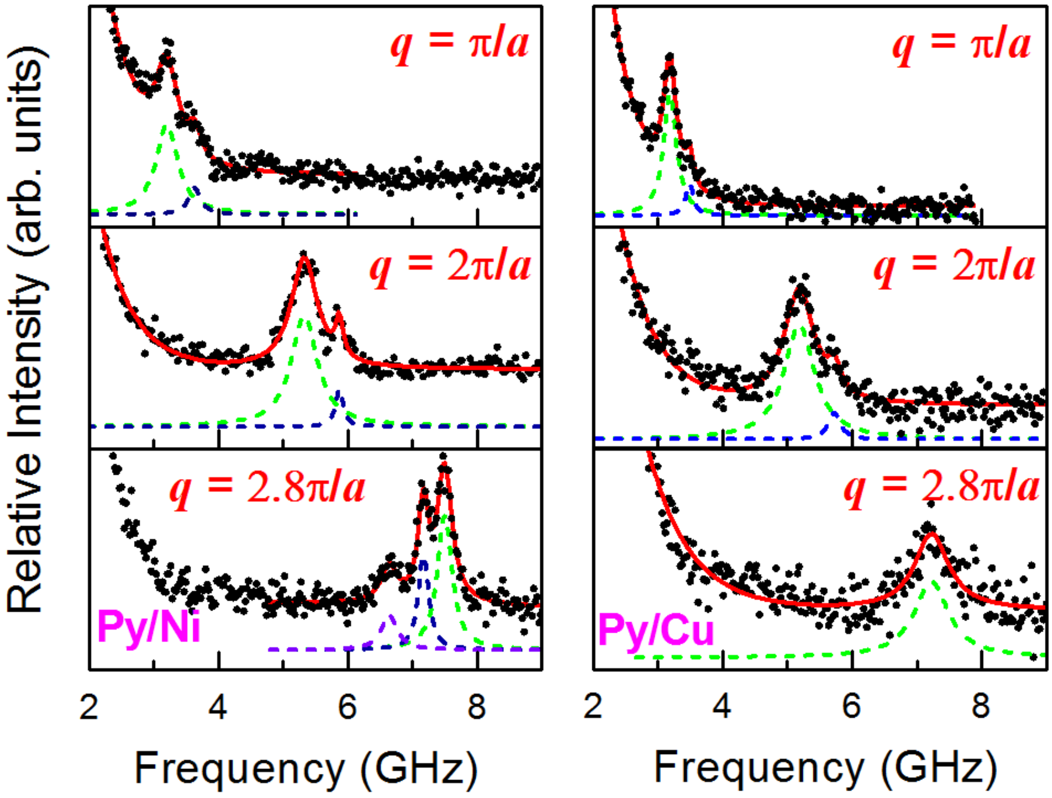

Fig. 5.10 Brillouin *p*-*p* polarization spectra of the Py/Ni (left) and Py/Cu (right) phononic crystals measured at various *q*.

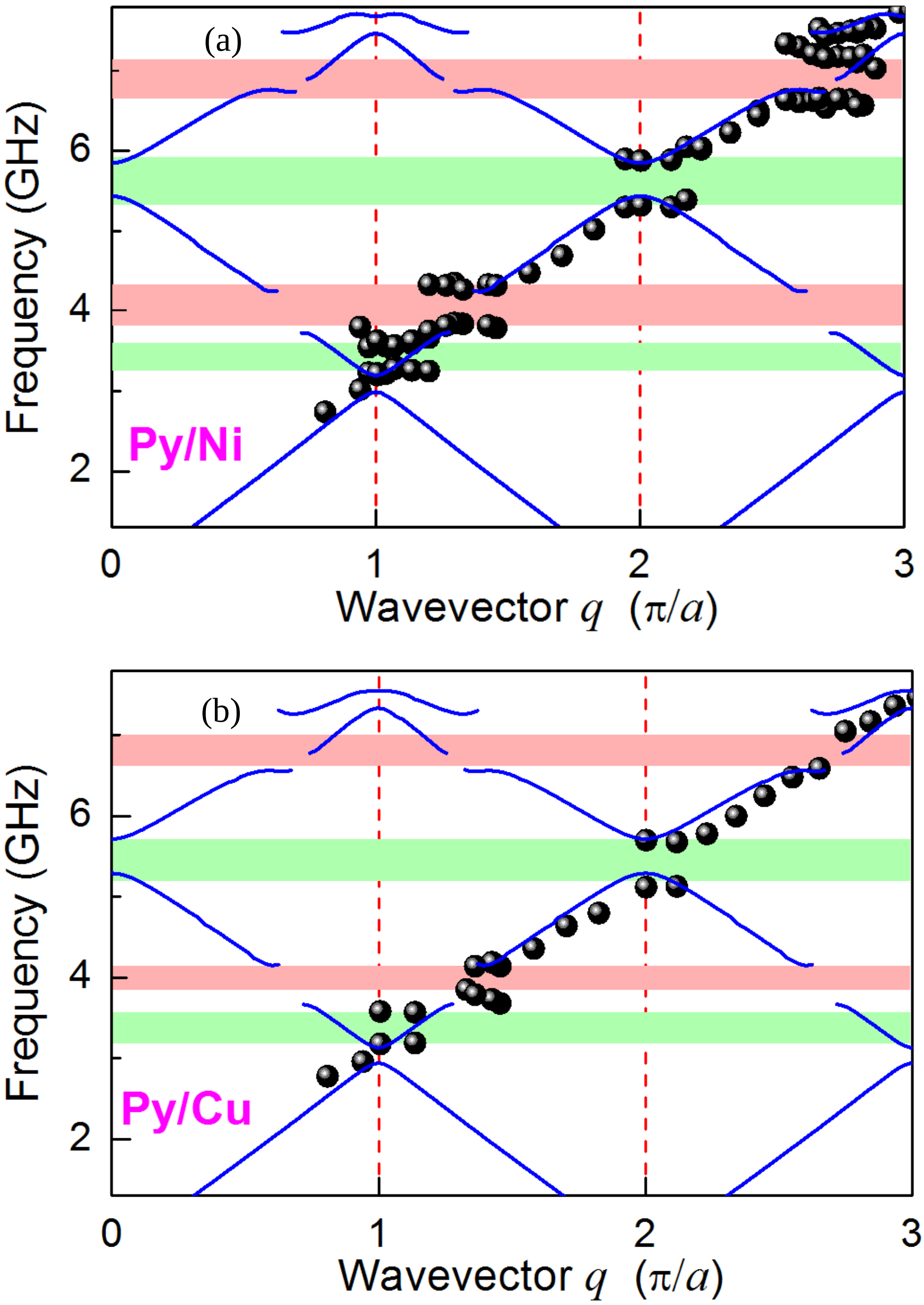

Fig. 5.11 Experimental and theoretical surface phonon dispersion relations in (a) Py/Ni and (b) Py/Cu samples. Experimental and theoretical data are denoted by symbols and continuous curves respectively. Measured bandgaps are indicated by shaded bands, and Brillouin zone boundaries by vertical dashed lines.

The surface phonon band structures of these three phononic crystals are almost identical, a consequence of the similar densities and elastic parameters of their constituent materials. The dispersion of Py/Ni array shown in Fig. 5.11a features two Bragg bandgaps at the first and second BZ boundaries with respective widths of 0.4 and 0.6 GHz, as well as two hybridizations gaps within the second and third BZs with both widths of about 0.5 GHz. The band structure of Py/Cu in Fig. 5.11b also reveals four gaps with respective widths of 0.4, 0.3, 0.6 and 0.4 GHz. The slight differences in bandgap widths could be due to the slight differences of the densities and elastic constants.

There are also some differences in the hybridization gaps of the various phononic crystals examined. These gaps observed in Py/Cu are not as broad as those in Py/Fe and Py/Ni. Three Brillouin peaks were observed at $q = 2.8\pi/a$, where the second hybridization gap occurs, in Py/Ni, while only one peak for Py/Cu. The modes at $q = 2.8\pi/a$ are leaky SAWs, resulting in their observed peaks being broad [20]. In fact the two peaks observed in Py/Fe and the three peaks observed in Py/Ni are all quite sharp, indicating very weak radiative coupling in the substrate, which permits accurate detection of the modes.

It can be seen from Fig. 5.11a that there are three branches at the second hybridization gap. One additional higher frequency calculated branch (the highest branch at the 2nd hybrid gap) is shown in Py/Ni in agreement with experimental observed branch. This branch of Py/Cu is also shown in Fig. 5.11b, but it is not clear why this branch was not observed in the Py/Fe and Py/Cu samples. This could be due to the low BLS intensity of the highest branch in Py/Fe and Py/Cu. Another possible reason for this difference in the observed SAW dispersions could be due to the slight differences in the sample quality. Further work like calculating the BLS spectrum intensity to find out which modes are detectable, could be performed to account for the differences in the observed dispersions for these three samples.

5.6 Summary

The phononic dispersions of a 1D periodic array of Fe (or Ni, Cu) and Py nanostripes on a SiO_2/Si substrate were investigated by Brillouin spectroscopy. The measured phononic band structures of surface elastic waves reveal Bragg and hybridization bandgaps for all three samples. Numerical simulations generally reproduced the experimental dispersion data. Our samples are also 1D magphonic crystals (MPCs), i.e., one possessing dual phononic and magnonic bandgaps [21]. The magnonic dispersions of these samples have been investigated by my fellow student Ma Fusheng (F. S. Ma).

For these MPCs studied, the band structure of magnons is dependent only on the magnetic properties of the constituent materials of the top periodic layer. In contrast, the band structure of SAWs also depends on the elastic properties of the SiO_2/Si substrate. Thus MPCs, exhibiting the same magnonic band structure but different phononic ones, can be engineered by selecting the same pair of constituent magnetic materials, but different underlying substrate materials for fabrication. Conversely, if MPCs possessing the same phononic band structure, but different magnonic ones are desired, then different pairs of constituent magnetic materials atop the same support substrate are to be selected.

It is noteworthy that, for all three samples studied, while application of a magnetic field radically modifies their magnon dispersion spectra, their corresponding phonon ones are found to be independent of magnetic field, suggesting the absence of magnonic-phononic interactions. This has important implications for potential applications. For instance, information carried by magnons and phonons could be separately and simultaneously processed in devices based on such magphonic crystals, with no undesirable cross-talk between the two excitations. Additionally the magnonic bandgaps in such devices can be tuned by the application of a magnetic field, independently of the phononic bandgaps. It is hoped that our studies will spur further interest in these metamaterials which are also of great fundamental scientific interest.

References:

1. G. A. Antonelli, H. J. Maris, S. G. Malhotra, and J. M. E. Harper, J. Appl. Phys. **91**, 3261 (2002).

2. Y. Pennec, J. O. Vasseur, B. Djafari-Rouhani, L. Dobrzyński, and P. A. Deymier, Surf. Sci. Rep. **65**, 229 (2010).

3. I. R. H. Olsson and I. El-Kady, Meas. Sci. and Technol. **20**, 012002 (2009).

4. Z. K. Wang, V. L. Zhang, H. S. Lim, S. C. Ng, M. H. Kuok, S. Jain, and A. O. Adeyeye, ACS Nano **4,** 643 (2010).

5. *COMSOL Multiphysics*, Structural Mechanics, Manual, Comsol, AB, Stockholm, Sweden.

6. A. M. James and M. P. Lord, *Index of Chemical and Physical Data* (The Macmillan Press Ltd., New York, 1992).

7. H. Deng, M. K. Minor, and J. A. Barnard, IEEE Trans. Magn. **32,** 3702 (1996).

8. B. A. Auld, *Acoustic Fields and Waves in Solids*, Vol. 2 (Wiley, New York, 1973).

9. W. A. Brantley, J. Appl. Phys. **44,** 534 (1973).

10. M. G. Beghi, C. E. Bottani, P. M. Ossi, T. A. Lafford, and B. K. Tanner, J. Appl. Phys. **81,** 672 (1997).

11. J. R. Dutcher, S. Lee, B. Hillebrands, G. J. McLaughlin, B. G. Nickel, and G. I. Stegeman, Phys. Rev. Lett. **68,** 2464 (1992).

12. A. A. Maznev, Phys. Rev. B **78,** 155323 (2008).

13. A. A. Maznev and O. B. Wright, J. Appl. Phys. **105**, 123530 (2009).

14. A. A. Maznev and A. G. Every, J. Appl. Phys. **106,** 113531 (2009).

15. N. E. Glass and A. A. Maradudin, J. Appl. Phys. **54**, 796 (1983).

16. L. Giovannini, F. Nizzoli, and A. M. Marvin, Phys. Rev. Lett. **69**, 1572 (1992).

17. B. Djafari-Rouhani, A. A. Maradudin, and F. Wallis, Phys. Rev. B **29**, 6454 (1984).

18. R. Jorna, D. Visser, V. Bortolani, and F. Nizzoli, J. Appl. Phys. **65,** 718 (1989).

19. L.B. Freund, S. Suresh. *Thin Film Materials: Stress, Defect Formation, and Surface Evolution* (Cambridge University Press, Cambridge, UK, 2003).

20. P. Mutti, C. E. Bottani, G. Ghislotti, M. Beghi, G. A. D. Briggs, and J. R. Sandercock, in *Advances in Acoustic Microscopy*, edited by A. Briggs (Plenum,

New York, 1995), Vol. 1, p. 249.

21. V. L. Zhang, F. S. Ma, H. H. Pan, C. S. Lin, H. S. Lim, S. C. Ng, M. H. Kuok, S. Jain, and A. O. Adeyeye, Appl. Phys. Lett. **100**, 163118 (2012).

Chapter 6 Phononic Dispersions of Surface Waves on Permalloy/BARC Nanostructured Arrays

6.1 Introduction

The previous chapter presented our findings on the surface wave dispersion relations of 1D phononic crystals composed of linear periodic arrays of alternating Permalloy and Fe (or Ni, Cu) nanostripes on a SiO_2/Si substrate (henceforth referred to as Py/Fe(Ni, Cu)). As the materials of the elements of these bi-component arrays are both metals, namely either Py/Fe, Py/Ni or Py/Cu, the elastic and density contrast between adjacent elements is low. The phononic bandgaps observed in these structures are small, being of the order of 0.5 GHz.

In general, the phononic bandgap width increases with elastic and density contrast [1,2]. It would be of interest to study the SAW dispersion relations in phononic crystals with large elastic and density contrast. In this chapter, two phononic crystals of 1D linear periodic arrays of alternating Py and BARC (bottom anti-reflective coating) nanostripes on a Si(001) substrate, with 350 nm and 400 nm lattice constants respectively, were investigated. The widths of Py stripes for both samples are 250 nm, and the widths of BARC are 100 and 150 nm respectively; the samples are referred to as Py250/BARC100 and Py250/BARC150. BARC is a polymer with elastic properties similar to those of PMMA and PS. These two materials, Py and BARC, were selected for the high elastic and density contrast between them. Hence, the phonon dispersions are expected to be significantly different from those of Py/Fe(Ni, Cu). The dispersions are also expected to change for Py250/BARC100 and Py250/BARC150.

The band structures of surface acoustic waves for both samples were measured by Brillouin light scattering (BLS) which is a powerful probe of such excitations in nanostructured materials [3-5]. Each of the measured phononic dispersion spectrum features a Bragg gap opening at the Brillouin zone (BZ) boundary, and a large hybridization bandgap, whose origin is different from those reported for other 1D periodic phononic crystals [4-8]. The slow phonons, the third branch of the dispersion relation, reveal near-localization characteristics. In addition, the gaps were tuned by changing the periodicity of the phononic structure. Numerical simulations, carried out within the finite element framework, of the phononic dispersions yielded good agreement with experiments.

6.2 Fabrication of Py/BARC samples and BLS measurements

Both the samples studied in this work were designed by us and fabricated by Professor Adekunle Olusola Adeyeye [9]. We will first discuss our work on Py250/BARC100 with lattice constant a = 350 nm. A 4 × 4 mm^2 patterned area of 63nm-thick 1D periodic array of alternating 250nm-wide Py and 100nm-wide BARC nanostripes was fabricated on a Si(001) substrate using deep ultraviolet (DUV) lithography at 248 nm exposing wavelength. The substrate was first coated with a 63nm-thick bottom BARC layer, followed by a 480nm-thick positive DUV photoresist. A Nikon lithographic scanner with a KrF excimer laser radiation was then used for exposing the resist. To convert the resist patterns into nanostripes, 63nm-thick Py was deposited using electron beam evaporation technique followed by the lift-off in OK73 and isopropyl alcohol. An ultrasonic bath was used to create agitation for easy lift-off of the Py layer. Completion of the lift-off process was determined by the color contrast of the patterned Py regions and confirmed by inspection under a scanning electron microscope (SEM). Figure 6.1 shows an SEM image of the resulting structure.

The 180°-backscattering geometry was used in the BLS experiments, with the scattering plane normal to the sample surface and the phonon wavevector ***q*** along the periodicity direction (*x* direction in Fig. 6.1) which coincides with the [110] direction of the Si substrate. Spectra of the acoustic waves were measured in *p-p* polarization and the SAW dispersion relation mapped by varying the laser light incidence angle.

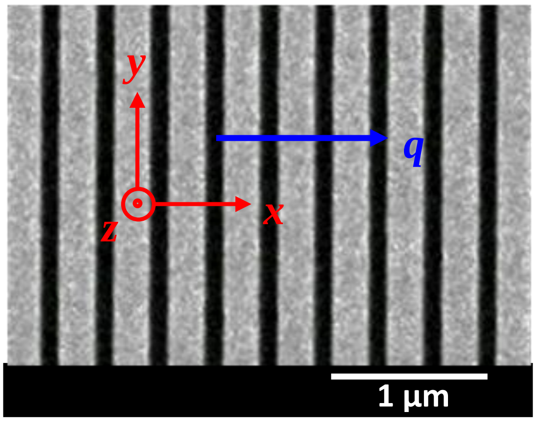

Fig. 6.1 SEM image of the Py250/BARC100 phononic crystal. Orientation of Cartesian coordinate system with respect to nanostripes and phonon wavevector ***q***.

6.3 Results of Py250/BARC100 sample

Figures 6.2 shows typical Brillouin *p*-*p* spectra recorded. For each spectrum, three peaks were observed. Their mode frequencies obtained from spectral fits using Lorentzian functions were plotted against wavevector to yield dispersion relations shown in Fig. 6.3. The measured phononic dispersion spectrum features a 1.0 GHz gap opening centered at 4.8 GHz at the BZ boundary, and a 2.2 GHz bandgap centered at 6.5 GHz.

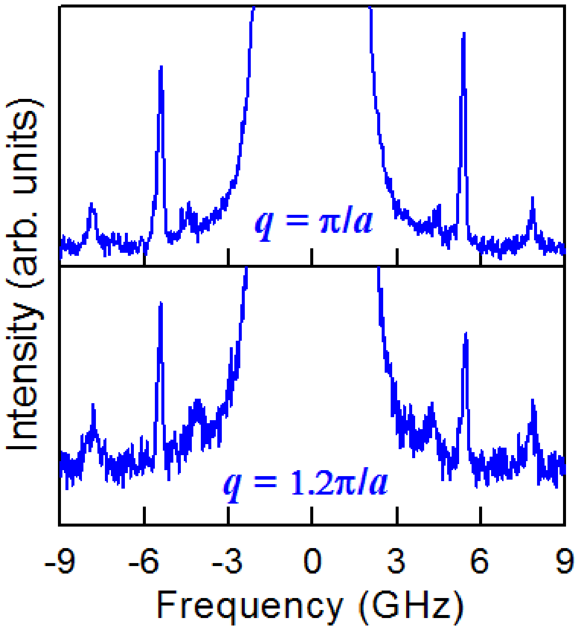

Fig. 6.2 Polarization Brillouin spectra of phonons.

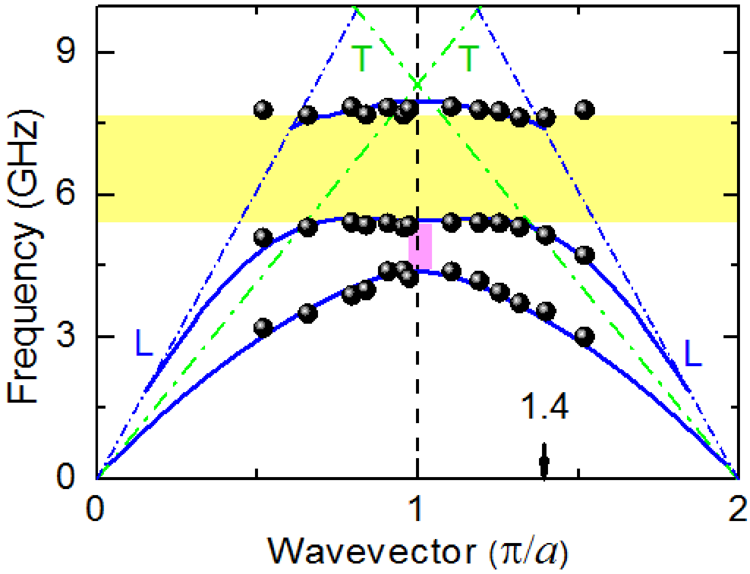

Fig. 6.3 Phonon dispersion relations of the Py250/BARC100 array. Experimental and theoretical data are denoted by dots and solid lines respectively. The transverse (T) and longitudinal (L) bulk wave thresholds are represented by respective green dot-dashed lines and blue short dot-dashed lines. Measured Bragg gap opening and the hybridization bandgap are indicated by a pink rectangle and a yellow band respectively.

Dispersion relations and mode displacement profiles of surface acoustic waves (SAWs) were computed using the finite element approach in COMSOL Multiphysics [10] and the Bloch-Floquet theorem as the periodic boundary condition. The 350nm-wide computational cell used comprises a 63nm-thick layer of a 100nm-wide BARC stripe sandwiched between two 125nm-wide Py stripes, atop a 2 μm-thick Si substrate, with its bottom boundary fixed. It is to be noted that unlike the case of the 1D Py/Fe nanostripe array studied in the Chapter 5, no interfacial air gaps were considered in the calculations, as the fabrication process employed here precludes their formation. Elastic parameters used in the simulations for Py, BARC and Si are Young's moduli = 180, 6.26, and 169 GPa, Poisson ratios = 0.31, 0.34, and 0.064, mass densities = 8600, 1190 and 2330 kg/m^3 respectively [11-13]. The simulated dispersion relations for the lowest three SAW branches, below the longitudinal bulk wave threshold [14,15], presented in Fig. 6.3, accord well with the Brillouin measurements. Also shown in the figure are the dispersion relations of the vertically polarized transverse (T) and longitudinal (L) bulk waves, in the [110] direction, of the Si substrate.

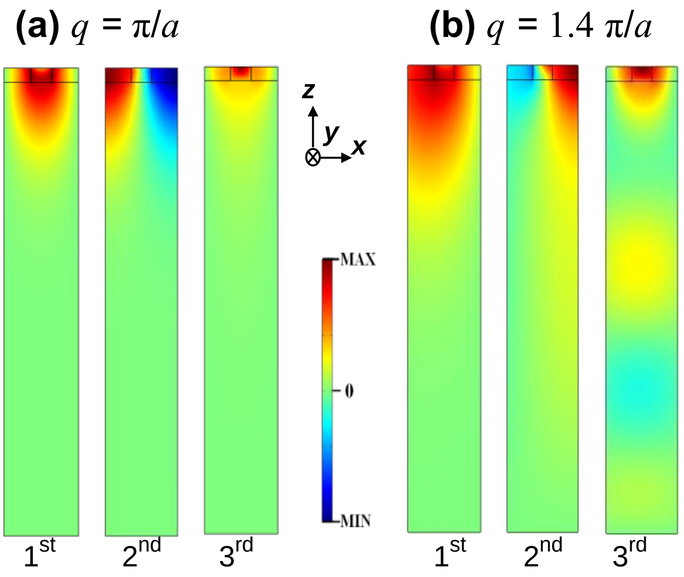

Fig. 6.4 *z*-components of the displacements of observed phonon modes at (a) $q = \pi/a$ and (b) $q = 1.4\pi/a$. The profiles are color-coded, with red denoting maximal displacement.

Simulated mode profiles for $q = \pi/a$, shown in Fig. 6.4a, of the lowest two modes exhibit characteristics of the surface Rayleigh wave (RW). These RWs are standing Bloch waves satisfying the Bragg scattering condition. The mode profile of the third branch at the BZ boundary reveals that it is also a standing wave with most of its energy confined in the BARC stripes. Mode profiles for $q = 1.4\pi/a$, displayed in Fig. 6.4b, indicate that at this wavevector, the first branch has the characteristics of the RW. In contrast, the higher two SAWs leak energy into the Si substrate as their dispersion curves extend beyond the transverse bulk wave threshold [7,14-16].

The vertical surface displacement u_z of an acoustic eigenmode characterized by frequency ω and reduced wavevector q, in a 1D periodic structure can be represented by a superposition of Bloch harmonics,

$$u_z = \sum_{n=-\infty}^{\infty} A_n \exp\left[i\left(q + \frac{2\pi n}{a} \right) x - i\omega t \right], \tag{6.1}$$

At the BZ boundary $q = \pi/a$,

$$u_z = \sum_{n=-\infty}^{\infty} A_n \exp\left[i\frac{\pi}{a}(1+2n)x - i\omega t \right]. \tag{6.2}$$

We set $x = 0$ at the center of a BARC stripe. Due to the symmetry of the structure, an eigenmode should be either symmetric or anti-symmetric [17]:

$$u_z^{sym} = \sum_{n=-\infty}^{\infty} 2A_n^{sym} \cos\left[\frac{\pi}{a}(1+2n)x \right] \exp\left[-i\omega_{sym} t \right], \tag{6.3}$$

$$u_z^{asym} = \sum_{n=-\infty}^{\infty} 2iA_n^{asym} \sin\left[\frac{\pi}{a}(1+2n)x \right] \exp\left[-i\omega_{asym} t \right]. \tag{6.4}$$

At the first BZ boundary when $n = 0$, these eigenmodes are standing waves with symmetric mode having nodes at the centers of Py stripes ($x = a/2 + ma$, $m = 0, 1, 2\ldots$), and antisymmetric mode at the centers of BARC stripes ($x = ma$). The term “nodes” is applied here only to the z-component of the displacement. This analysis agrees with the mode displacement profiles in Fig. 6.4. It should be noted that the description of symmetric and antisymmetric modes depends on our choice of the symmetry plane at $x = 0$.

The dispersion relations of RW and Sezawa wave (SW) were modeled by treating the Py/BARC array as a homogeneous effective medium [17] on a Si substrate. The equations used to calculate the effective elastic constants of the film correspond to a parallel-spring association,

$$C_{eff} = fC_{Py} + (1 - f)C_{BARC}, \tag{6.5}$$

where C_{eff}, C_{Py} and C_{BARC} are the respective elastic constants of the effective medium, pure Py and pure BARC, and f the volume fraction of Py in the periodic structure. The calculated density, Young's modulus and Poisson ratio of the effective film are 6483 kg/m^3, 130 GPa and 0.31 respectively. Simulated phonon dispersions based on these parameters are presented in Fig. 6.5. It can be seen that the gap opening arises from the zone folding of the RW dispersions and avoided crossings at the BZ boundary.

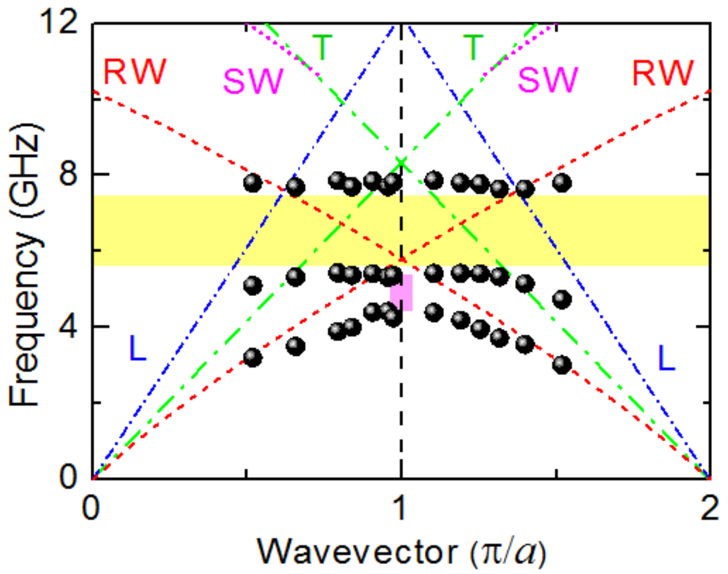

Fig. 6.5 Phonon dispersion relations. Red dashed lines and magenta dotted lines represent the simulated Rayleigh wave (RW) and Sezawa wave (SW) dispersions for the effective medium film on Si(001) substrate. Experimental data of Py250/BARC100 are shown as dots.

A prominent feature of the phonon dispersion spectrum is the large hybridization bandgap. For a structure, such as ours, comprising a “slow” film on a “fast” substrate, Sezawa waves will exist only below the transverse bulk wave threshold, and over a restricted range of qh, where h is the film thickness [6,18]. As shown in Fig. 6.5, within the first BZ, the SW and zone-folded RW do not cross, indicating that the measured bandgap does not originate from the hybridization of these waves. Instead, within the bandgap, the zone-folded RW crosses the transverse bulk wave threshold. The most likely reason for this hybridization gap should be the avoided crossing of the zone-folded RW and a pseudo-SAW whose velocity is close to that of the shear vertical bulk wave of the substrate. Additionally, attenuated SAWs, called pseudo-Sezawa waves, having a velocity larger than that of the shear vertical bulk wave of the substrate have been observed in film-substrate systems [15,18,19]. These pseudo-Sezawa waves lie within the Lamb shoulder near the transverse bulk wave threshold and exist as resonances with the substrate continuum of modes. We thus attribute the origin of the bandgap to the hybridization and avoided crossing of the zone-folded RW and pseudo-Sezawa waves. The modes of the second branch above this threshold should have the characteristics of pseudo-Sezawa waves (see Fig. 6.4b).

The origin of this hybridization bandgap is to be contrasted with those reported for other 1D phononic crystals. For instance, Zhang *et al.* [4] and Maznev [15,16] attributed the origin of the bandgaps they observed in film-substrate samples to the avoided crossings of the RW and zone-folded Sezawa modes. Additionally, hybridization bandgaps in Si and SiO_2 gratings [5,8] have been ascribed to the mixing of the RW and the longitudinal resonance, also referred to as the high-frequency pseudo-surface wave. The unique origin of the gap is of interest to future research on SAW dispersions in phononic crystals.

Another noticeable feature is that the third branch of the band structure has an almost flat dispersion. Total displacement mode profiles of this branch at various wavevector values are shown in Fig. 6.6. We chose to show the total displacement because it is easier to see the total energy localization. The profiles reveal near-localized characteristics of the modes, with most of their energy localized in the BARC stripes. However, these modes are modified by the surrounding Py stripes and Si substrate. These near-localized modes also leak energy via bulk waves above the transverse bulk wave threshold. The band structures of the Py/Fe(Ni, Cu) samples reported in the last chapter, do not contain such flat branches corresponding to mode localization in one material of the stripes. This suggests that such near dispersionless branch may exist only when the density and elastic contrast of the component materials is very high.

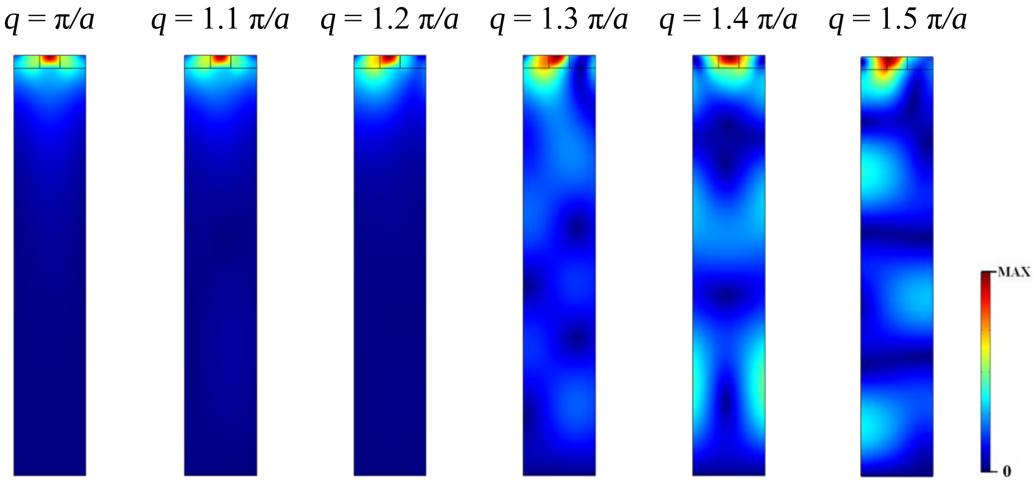

Fig. 6.6 Total displacement mode profiles of the third branch of Py250/BARC100 at various wavevectors. The profiles are color-coded, with red denoting maximal displacement.

6.4 Results of Py250/BARC150 sample

The Py250/BARC150 sample comprises a 63nm-thick 1D periodic array of alternating 250nm-wide Py and 150nm-wide BARC nanostripes on a Si(001) substrate. The spectra recorded at $q < 1.5\ \pi/a$ reveal three peaks just like the Py250/BARC100 sample. The spectra at $q > 1.5\ \pi/a$ contain an additional weak broad peak at high frequencies which is not observed for Py250/BARC100. The spectra were fitted using Lorentzian functions and the resultant phonon frequencies were plotted against wavevector to yield dispersion relations shown in Fig. 6.7.

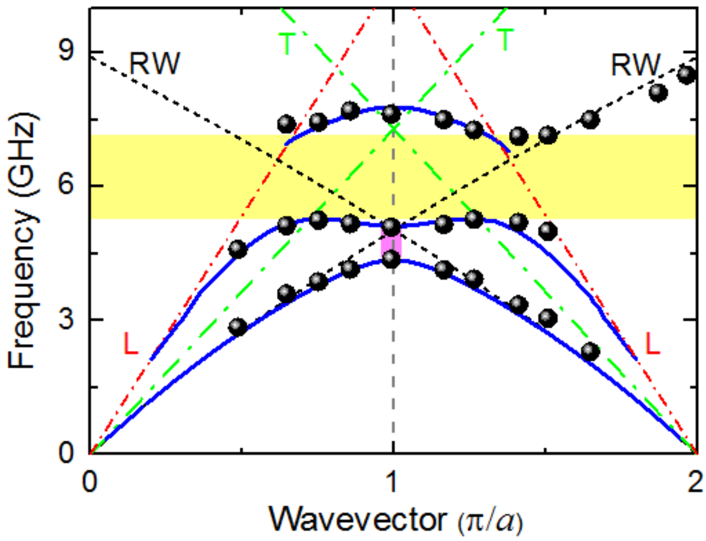

Fig. 6.7 Phonon dispersion relations of Py250/BARC150. Experimental and theoretical data are denoted by dots and solid lines respectively. The transverse (T) and longitudinal (L) bulk wave thresholds are represented by respective green dot-dashed lines and red short dot-dashed lines. The measured Bragg gap opening and hybridization bandgap are shown as a pink rectangle and a yellow band respectively. Black dashed lines represent simulated Rayleigh wave (RW) dispersions for the Py reference film on Si(001) substrate.

The measured surface phonon dispersion spectrum plotted in Fig. 6.7 features a 0.7 GHz gap opening centered at 4.3 GHz at the BZ boundary, and a 1.9 GHz hybridization bandgap centered at 6.2 GHz. It is known that the SAW dispersions and the gaps can be tuned by changing the lattice constant of the phononic structure. Compared to the gaps observed in Py250/BARC100, the sizes of those in Py250/BARC150 are smaller and the gap centers are lower, a consequence of the larger lattice constant of this sample.

The lowest three branches of the simulated SAW dispersions of the phononic structure under the longitudinal bulk wave threshold were also plotted in Fig. 6.7. Except for the third branch at $q > 1.5\ \pi/a$, the agreement between the measured data and simulated ones is good. We calculated the SAW dispersions of a 63nm-thick Py reference film on Si substrate and plotted the Rayleigh wave dispersion in Fig. 6.7. It can be seen that the third branch of the observed modes at $q > 1.5\ \pi/a$ generally follows the RW of Py film, which implies that these modes have the characteristics of the RWs.

Although the SAW dispersions of the two samples studied are similar, the third branch of Py250/BARC150 looks more dispersive than that of Py250/BARC100 even for $q < 1.5\ \pi/a$. As the width of the BARC stripes is 150 nm in the former sample, the localization of the modes is not as strong as that of the 100nm-wide BARC stripes of the latter. In addition, the modes should also have some pseudo-Sezawa characteristics.

6.5 Discussions

For a 1D bi-component phononic structure comprised of a periodic array of alternating nanostripes on a substrate, the SAW dispersion is influenced by the elastic properties of the component materials of the film, the lattice parameters, the filling fraction, the thickness of the film as well as the elastic properties of the substrate. Thus, the frequency bandgap can be tuned by changing any of the above factors.

It is noteworthy that the phonon dispersion spectra of Py/BARC phononic crystals differ substantially from those of the 1D Py/Fe(Ni, Cu) arrays presented in the last chapter. For instance, the main features of the dispersions of these two groups of samples are quite different. In addition, the measured gap openings of 1.0 GHz and 0.7 GHz at the BZ boundary of the former, are wider than the first bandgap of 0.4 GHz observed for the latter. The centers of these two gap openings at 4.8 and 4.3 GHz are also higher than those (≈ 3.4 GHz) of Py/Fe(Ni, Cu). Another notable difference is that the widths of the hybridization bandgaps (about 2 GHz) are considerably larger than those of the Py/Fe(Ni, Cu) arrays, whose maximum gap is only 0.6 GHz.

1. Elastic and density contrast

The differences could be due to various reasons. First, the elastic and density contrast between two metals (Fe, Ni or Cu and Py) is much lower than that between the polymer BARC and the metal Py. In general, the higher the elastic contrast, the larger would be the gap. Simulations were performed with the exact same structure of Py250/BARC100 sample to investigate the changes to the gap parameters by changing only the elastic and density contrast. We simulated the SAW dispersions of a 63nm-thick 1D periodic array of alternating 250nm-wide Py and 100nm-wide Fe (or Cu) nanostripes on Si substrate. Elastic parameters used in the simulations for Fe and Cu are Young's moduli = 211 and 130 GPa, Poisson ratios = 0.29 and 0.34, mass densities = 7870 and 8960 kg/m^3 respectively [20,21]. The lowest three branches of each calculated structure in the reduced BZ below the longitudinal bulk wave threshold are shown in Fig. 6.8. The calculated dispersion of Py/BARC is quite different from those of Py/Cu and Py/Fe for the same film thickness. The widest gap opening at the BZ boundary is that of Py/BARC sample which has the largest density and elastic contrast. It is also shown in Fig 6.8 that the widths of the hybridization gaps are also strongly dependent on the density and elastic contrast.

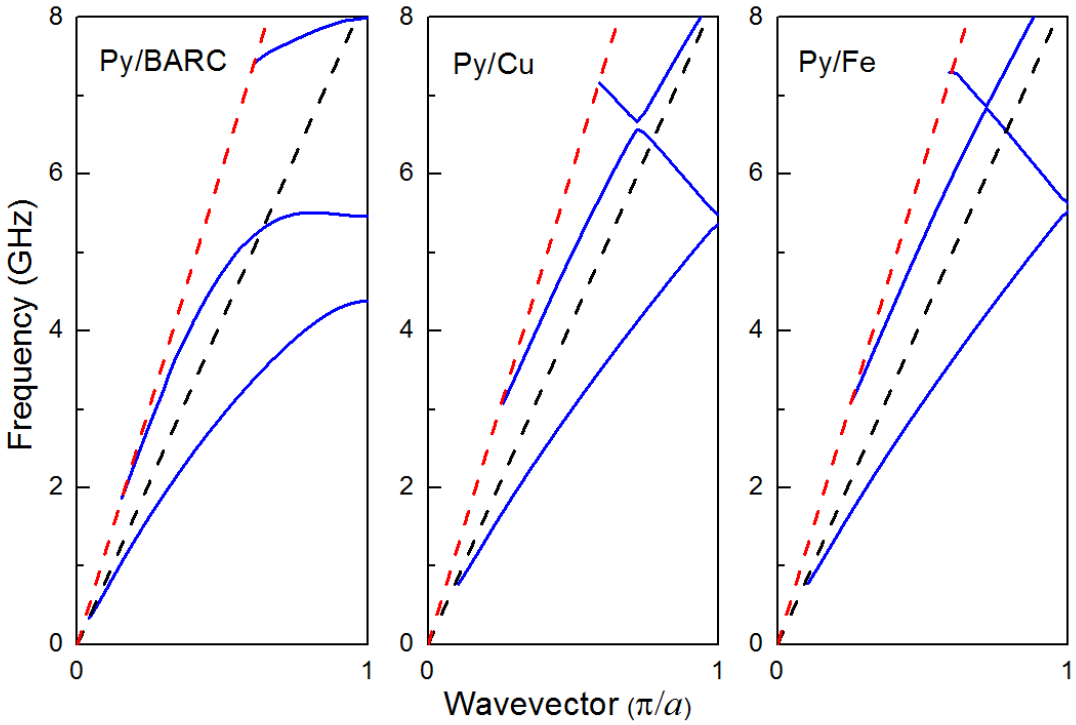

Fig. 6.8 Calculated phonon dispersions of Py/BARC, Py/Cu and Py/Fe phononic crystals with lattice constants of 350 nm. The calculated dispersions are denoted by blue solid curves, and the longitudinal and transverse thresholds of the Si(001) substrate by red and black dashed lines respectively.

2. Thickness of the patterned film

Second, the 63nm-thickness of Py/BARC film arrays is larger than the 30 nm one of the arrays Py/Fe(Ni, Cu). The thickness of the film plays an important role in SAW dispersions. The phonon dispersions in Py250/BARC100 array of the same structure but different array film thicknesses were numerically simulated. Figure 6.9 shows the calculated phonon dispersions of the lowest three branches below the longitudinal threshold in the reduced BZ of respective film thickness of 20, 40 and 63 nm. The dispersions clearly reveal that the centers of the gap opening at BZ boundary as well as the hybridization gap shift down with the increase of the film thickness, while the widths increase accordingly.

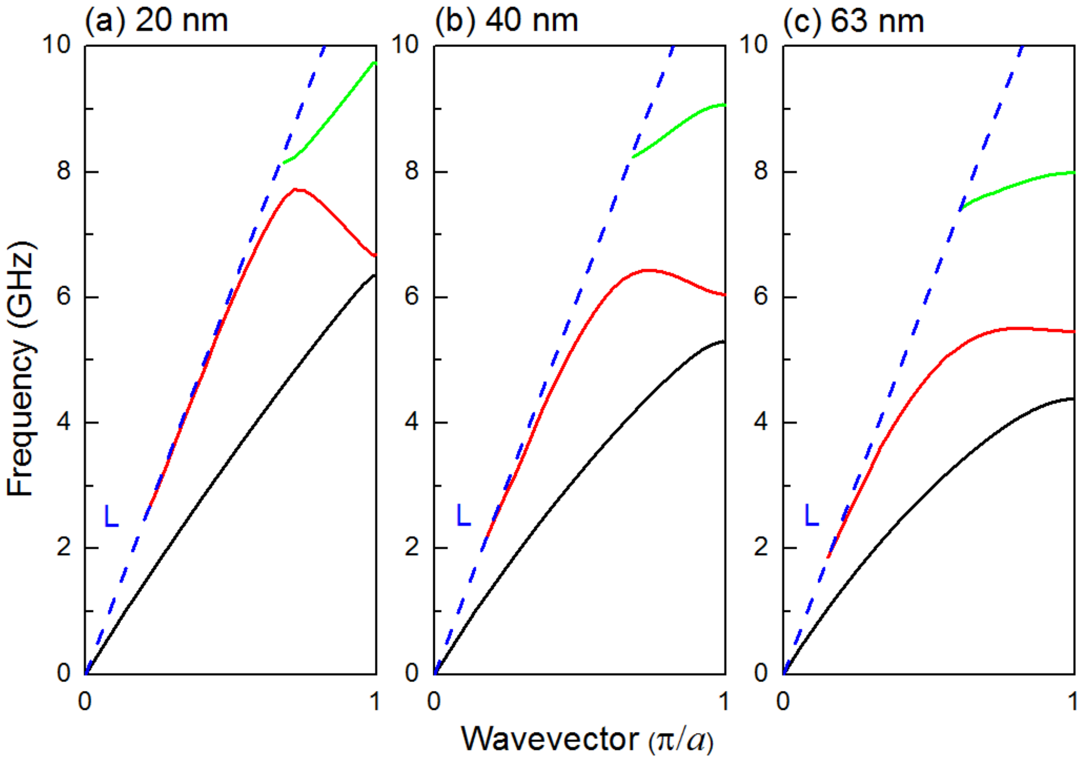

Fig. 6.9 Calculated phonon dispersions of Py/BARC film arrays with respective thicknesses of (a) 20, (b) 40 and (c) 63 nm. The calculated dispersions are denoted by solid curves, while those of the longitudinal bulk wave threshold (L) of the Si substrate by dashed lines.

Dhar and Roger have investigated the SAW dispersions in aluminum-coated glass gratings of different grating depths using the picosecond transient grating method [8]. Their findings generally support our conclusions although their samples were gratings. It should be mentioned the above conclusions will not be valid for all film array thicknesses. Further theoretical work need to be done to give a more comprehensive conclusion of the SAW dispersion dependence on the film thickness.

3. The substrate and sub-layer materials

The third reason is that our Py/BARC is directly patterned on a Si substrate, while the Py/Fe(Ni, Cu) samples contain an 800nm-thick SiO_2 sub-layer between the patterned arrays and the Si substrate which has the effect of red shifting the SAW frequencies. We calculated the band structure of a 63-nm thick Py/BARC film on an 800nm-thick SiO_2 sub-layer atop a Si substrate. The three lowest SAW branches of the calculated dispersion below the longitudinal threshold of the Si substrate are shown in Fig. 6.10. While the main features of the SAW dispersion remain almost the same, the entire band structure shifts lower in frequency when the 800nm-thick SiO_2 sub-layer is taken into account.

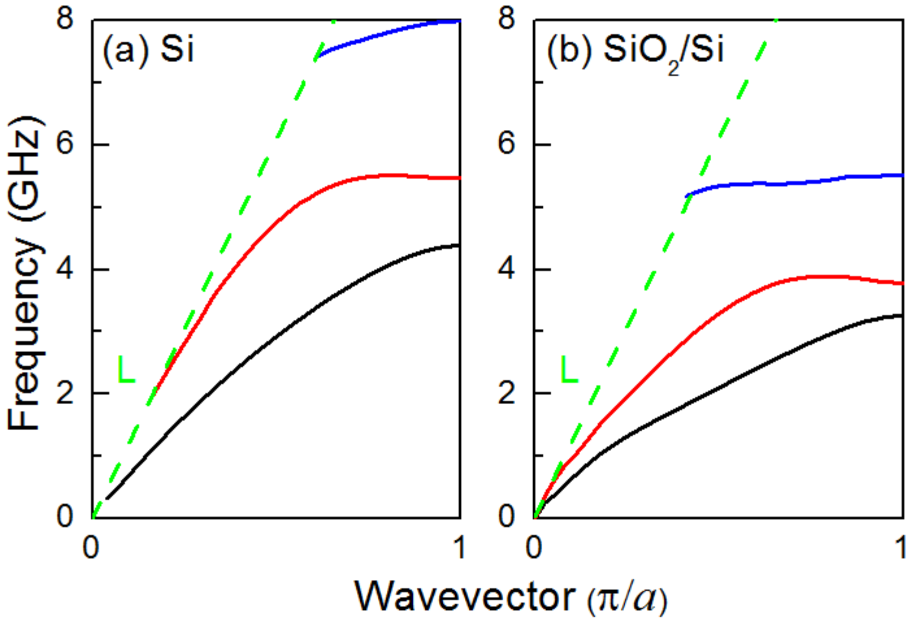

Fig. 6.10 Calculated phonon dispersions of Py/BARC arrays on (a) Si substrate and (b) 800nm-thick SiO_2 sub-layer atop a Si substrate. The calculated dispersions are denoted by solid curves, and the longitudinal bulk wave threshold (L) of the Si substrate by dashed lines.

4. Lattice parameter

Fourth, the periods of our Py/BARC are shorter than the 500 nm one of Py/Fe(Ni, Cu). We also simulated the SAW dispersion of a 63nm-thick periodic array of alternating 250nm-wide Py and 250nm-wide BARC nanostripes on Si substrate as shown in Fig. 6.11c. Our experimental results for two Py/BARC samples studied, as well as the simulated results show that increasing of the lattice constant shifts the centers of the gaps lower and narrows the gaps.

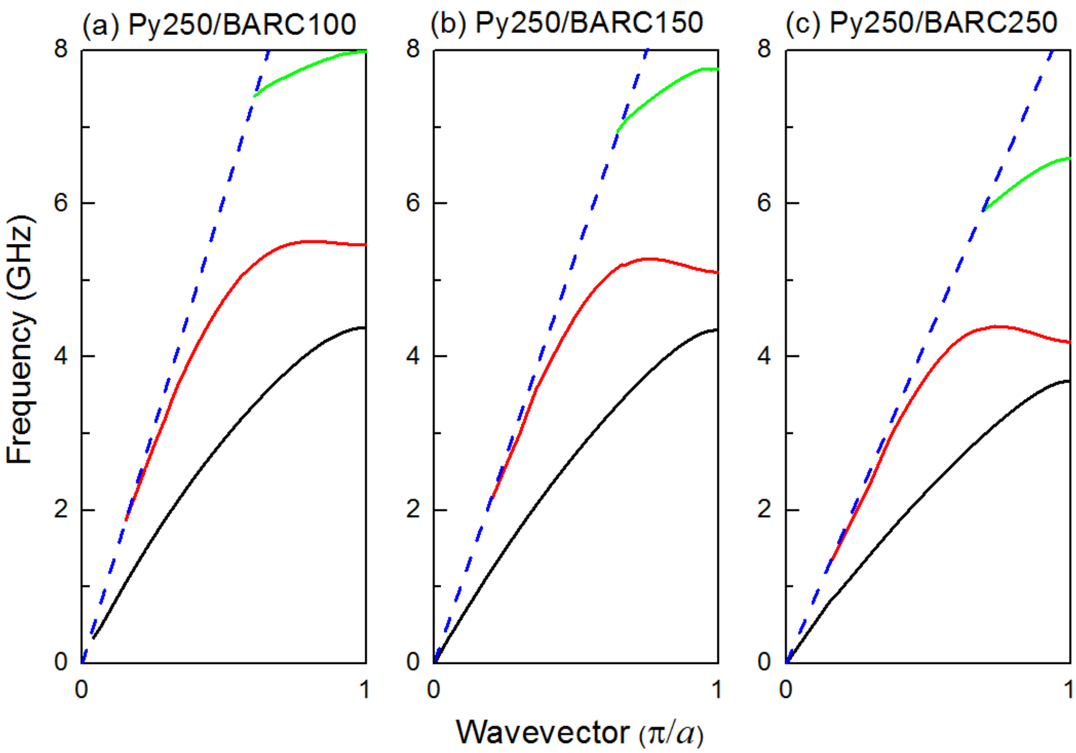

Fig. 6.11 Calculated phonon dispersions of Py/BARC arrays of lattice constant (a) 350, (b) 400 and (c) 500 nm on Si substrate. The calculated dispersions are denoted by solid curves, and the longitudinal bulk wave threshold of Si substrate by dashed lines.

From the above analyses, we deduce that the difference between the SAW dispersions of the Py/BARC and Py/Fe(Ni, Cu) samples mainly arises from the difference in the elastic and density contrast of their respective component materials. The thickness of the patterned film is also found to strongly influence the SAW dispersions. However, the gaps for small elastic and density contrast would not be very big, even for large thicknesses as shown in Fig 6.8. A sufficiently high elastic and density contrast is necessary for the formation of a large bandgap. Moreover, the SAW dispersions are dependent on the lattice parameters and the materials of the sub-layer and/or the substrate.

6.6 Conclusions

In summary, we have measured the SAW dispersions of two Py/BARC phononic crystals with different lattice constants by Brillouin light scattering. The measured phononic Bragg gap openings and hybridization bandgaps are much wider than those previously observed in laterally patterned multi-component phononic crystals. The hybridization bandgap has a unique origin in the hybridization and avoided crossing of the zone-folded Rayleigh and pseudo-Sezawa waves. The third branches of the dispersion relations of both samples exhibit near-localization character. In addition, the gaps can be tunable by varying the lattice constants. Finite element simulations generally reproduced the experimental phonon dispersion relations. Our findings could find applications in areas such as acoustic signal processing.

Refereces:

1. M. S. Kushwaha, P. Halevi, L. Dobrzynski, and B. Djafari-Rouhani, Phys. Rev. Lett. **71**, 2022 (1993).

2. W. Cheng, J. J. Wang, U. Jonas, G. Fytas, and N. Stefanou, Nat. Mater. **5**, 830 (2006).

3. V. L. Zhang, C. G. Hou, H. H. Pan, F. S. Ma, M. H. Kuok, H. S. Lim, S. C. Ng, M. G. Cottam, M. Jamali, and H. Yang, Appl. Phys. Lett. **101**, 053102 (2012).

4. V. L. Zhang, F. S. Ma, H. H. Pan, C. S. Lin, H. S. Lim, S. C. Ng, M. H. Kuok, S. Jain, and A. O. Adeyeye, Appl. Phys. Lett. **100**, 163118 (2012).

5. J. R. Dutcher, S. Lee, B. Hillebrands, G. J. McLaughlin, B. G. Nickel, and G. I. Stegeman, Phys. Rev. Lett. **68**, 2464 (1992).

6. A. A. Maznev, Phys. Rev. B **78**, 155323 (2008).

7. A. A. Maznev and O. B. Wright, J. Appl. Phys. **105**, 123530 (2009).

8. L. Dhar and J. A. Rogers, Appl. Phys. Lett. **77**, 1402 (2000).

9. A. O. Adeyeye, N. Singh, J. Phys. D, **41**,153001 (2008).

10. COMSOL Multiphysics, Structural Mechanics, COMSOL AB, Stockholm, Sweden.

11. H. Deng, M. K. Minor, and J. A. Barnard, IEEE Trans. Magn. **32**, 3702 (1996).

12. W. Cheng, N. Gomopoulos, G. Fytas, T. Gorishnyy, J. Walish, E. L. Thomas, A. Hiltner, and E. Baer, Nano Lett. **8**, 1423 (2008).

13. W. A. Brantley, J. Appl. Phys. **44**, 534 (1973).

14. N. E. Glass and A. A. Maradudin, J. Appl. Phys. **54**, 796 (1983).

15. P. Mutti, C. E. Bottani, G. Ghislotti, M. Beghi, G. A. D. Briggs, and J. R. Sandercock, in *Advances in Acoustic Microscopy*, edited by A. Briggs (Plenum, New York, 1995), Vol. 1, p. 249.

16. L. Giovannini, F. Nizzoli, and A. M. Marvin, Phys. Rev. Lett. **69**, 1572 (1992).

17. A. d. Bernabé, C. Prieto, L. González, Y. González, and A. G. Every, J. Phys. **11**, L323 (1999).

18. X. Zhang, J. D. Comins, A. G. Every, P. R. Stoddart, W. Pang, and T. E. Derry, Phys. Rev. B **58**, 13677 (1998).

19. R. C. Birtcher, M. H. Grimsditch, and L. E. McNeil, Phys. Rev. B **50**, 8990 (1994).

20. A. M. James and M. P. Lord, *Index of Chemical and Physical Data* (The Macmillan Press Ltd., New York, 1992).

21. L.B. Freund, S. Suresh. *Thin Film Materials: Stress, Defect Formation, and Surface Evolution* (Cambridge University Press, Cambridge, UK, 2003).

Chapter 7 Phononic Dispersion of a Two-dimensional Chessboard-patterned Bi-component Array

7.1 Introduction

Hypersonic phononic crystals, which are periodic nanostructured composites composed of two or more materials of different elastic properties and densities, have attracted great attention lately [1-10]. The acoustic counterpart of photonic crystals, phononic crystals are in principle able to control and manipulate the propagation of information-carrying acoustic waves (phonons), a functionality arising from their phononic band structure. As phonons have wavelengths that are several orders of magnitude shorter than those of photons of the same frequency, phononic crystals allow for easier miniaturization than photonic ones. Hypersonic phononic crystals have enormous potential applications in areas ranging from the control of thermal conductivity to heat management and acousto-optical devices [8-10].

As was reviewed in Chapter 1, most experiments on hypersonic phonon dispersions are confined to the study of bulk acoustic waves in phononic samples [4-7]. The few experimental studies that measured surface acoustic waves (SAWs) dispersion curves were based on one-dimensional (1D) structures [3,11-13]. Among them are the determination of the SAW dispersion for a grating etched on a Si(001) wafer by Dutcher *et al.* (1992) [11], and the measurement of the phononic dispersions of 1D periodic arrays of stripes of two alternating materials by Zhang *et al*. (2012) [3]. It is of interest to investigate higher-dimensional periodic structures whose surface phononic dispersions are more complex and richer in features than those of the 1D phononic crystals. Recently, Brillouin light scattering study on SAW dispersion relations in 2D phononic crystals comprising a square lattice of 100nm- or 150nm-high aluminum pillars with a spacing of 500 nm on a Si (001) substrate was reported by Graczykowski *et al.* (2012) [14]. The phononic dispersion of SAWs in 2D bi-component arrayed phononic crystals is expected to be more complicated and hence, the study of it is more interesting and challenging.

In this work, the band structures of the surface acoustic and surface optical waves on a 2D chessboard-patterned phononic crystal were investigated both experimentally and theoretically. The sample studied comprises a periodic array of alternating Permalloy and cobalt square nanodots on a SiO_2/Si substrate. We experimentally observed quasi-Rayleigh and quasi-Sezawa waves, and measured the comprehensive phononic dispersion relations over a full Brillouin zone. We were able to obtain measured dispersion spectra, including the folded branches (over two Brillouin zones). The measured band structures feature a hybridization bandgap in the Γ-X direction, and gap openings due to Bragg reflection at the X point. Of particular interest is the observation of an unusual class of surface elastic waves, arising from the chessboard-like structural nature of the bi-component array studied. We refer to them as “optical-like”, as the vibrations of neighboring nanodots possess out-of-phase characteristics, a motion broadly analogous to the atomic vibrations of the optical mode of a crystal with two different atoms per unit cell.

7.2 Sample fabrication and BLS measurements

The 2D 100 μm × 100 μm structure used in this study is a periodic array of alternating cobalt and Py square dots, each of side length *l* = 250 nm, arranged in a chessboard configuration. The sample was designed by us and fabricated by our collaborator Professor Hyunsoo Yang from the Department of Electrical and Computer Engineering, National University of Singapore.

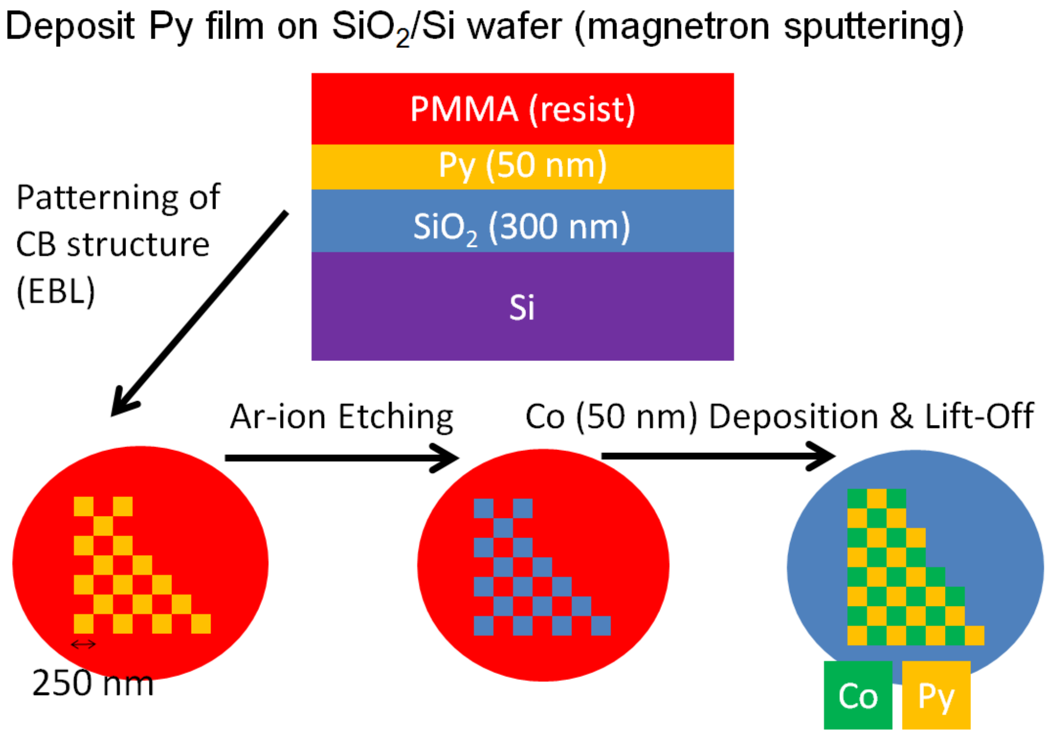

Fig. 7.1 Fabrication process of chessboard patterned structure.

The fabrication process is depicted in Fig. 7.1. First, a 50 nm-thick Py film was deposited on a (300 nm) SiO_2/Si wafer using dc magnetron sputtering. This was followed by the patterning, using high-resolution electron beam lithography, of the chessboard structure on a positive tone polymethyl methacrylate (PMMA) electron beam resist. By argon-ion etching, the developed patterns of the periodic square dots on the PMMA resist were transferred onto the Py film. Finally, a 50 nm-thick cobalt film was deposited by dc magnetron sputtering to fill the square-shaped holes, followed by the lift-off of the PMMA resist. A scanning electron micrograph (SEM) image of the resulting structure shown in Fig. 7.2 clearly reveals its chessboard pattern.

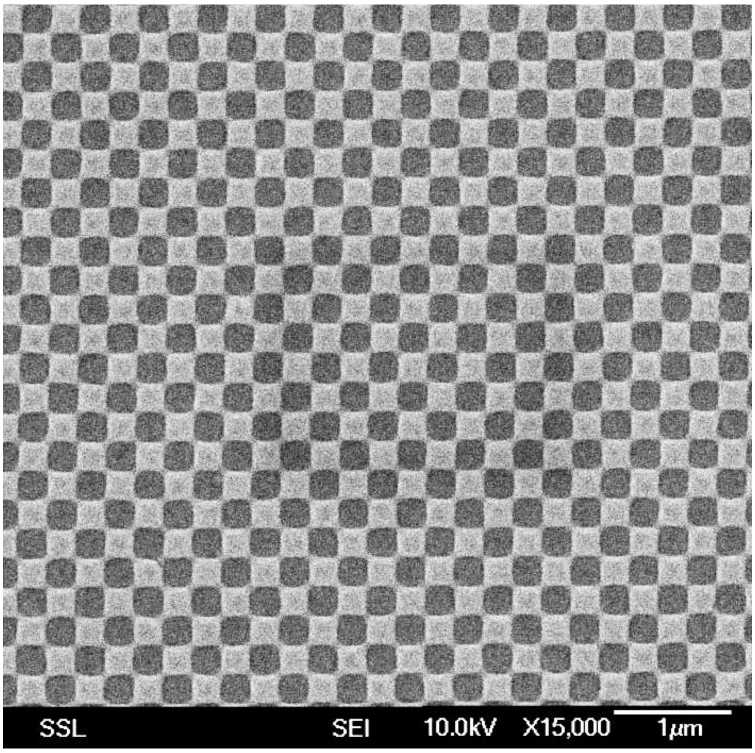

Fig. 7.2 SEM image of the Co/Py chessboard sample, with the Co dots appearing as darker squares.

Measurement of the frequency band structure of the acoustic waves was performed using Brillouin light scattering, a powerful tool for probing these waves in nanostructured materials [3-7,11,12,15]. Brillouin spectra were recorded in both *p-p* and *p-s* polarizations of the 180°-backscattering geometry, as shown in Fig. 7.3, with the scattering plane normal to the sample's metal surface and with the phonon wavevector ***q*** along either the Γ-M or Γ-X directions. The dispersion relations were mapped by varying the laser light incidence angle θ to achieve phonon wavevectors up to the second Brillouin zone.

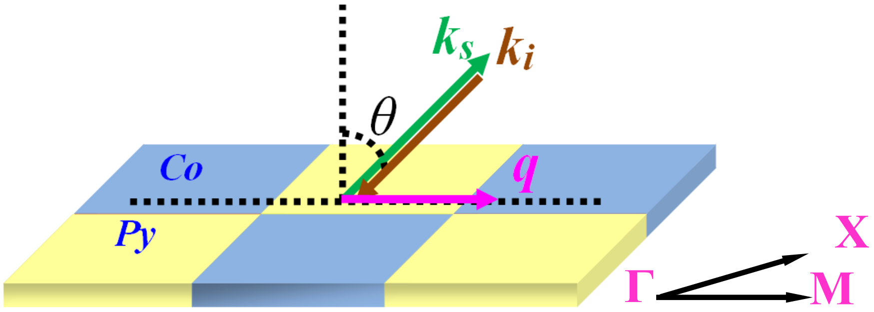

Fig. 7.3 Schematics of Brillouin light scattering geometry showing the light incident angle θ, incident and scattered photon wavevectors $\boldsymbol{k}_i$ and $\boldsymbol{k}_s$, phonon wavevector $\boldsymbol{q}$ along either Γ-M or Γ-X directions.

7.3 Experimental results and theoretical calculations

Typical Brillouin spectra recorded for Γ-X and Γ-M are presented in Figs. 7.4a and 7.4b respectively. The frequencies of the phonon peaks, obtained from a fit with Lorentzian functions, were plotted as a function of wavevector and displayed in Fig. 7.5. The resulting experimental band structures indicate that the observed modes are generally strongly dispersive. Among the notable features of the dispersion spectrum in the Γ-X direction are two gap openings, arising from Bragg reflection, of widths 0.2 and 0.5 GHz at the X point, and a 0.5 GHz-wide hybridization bandgap (see discussion below).

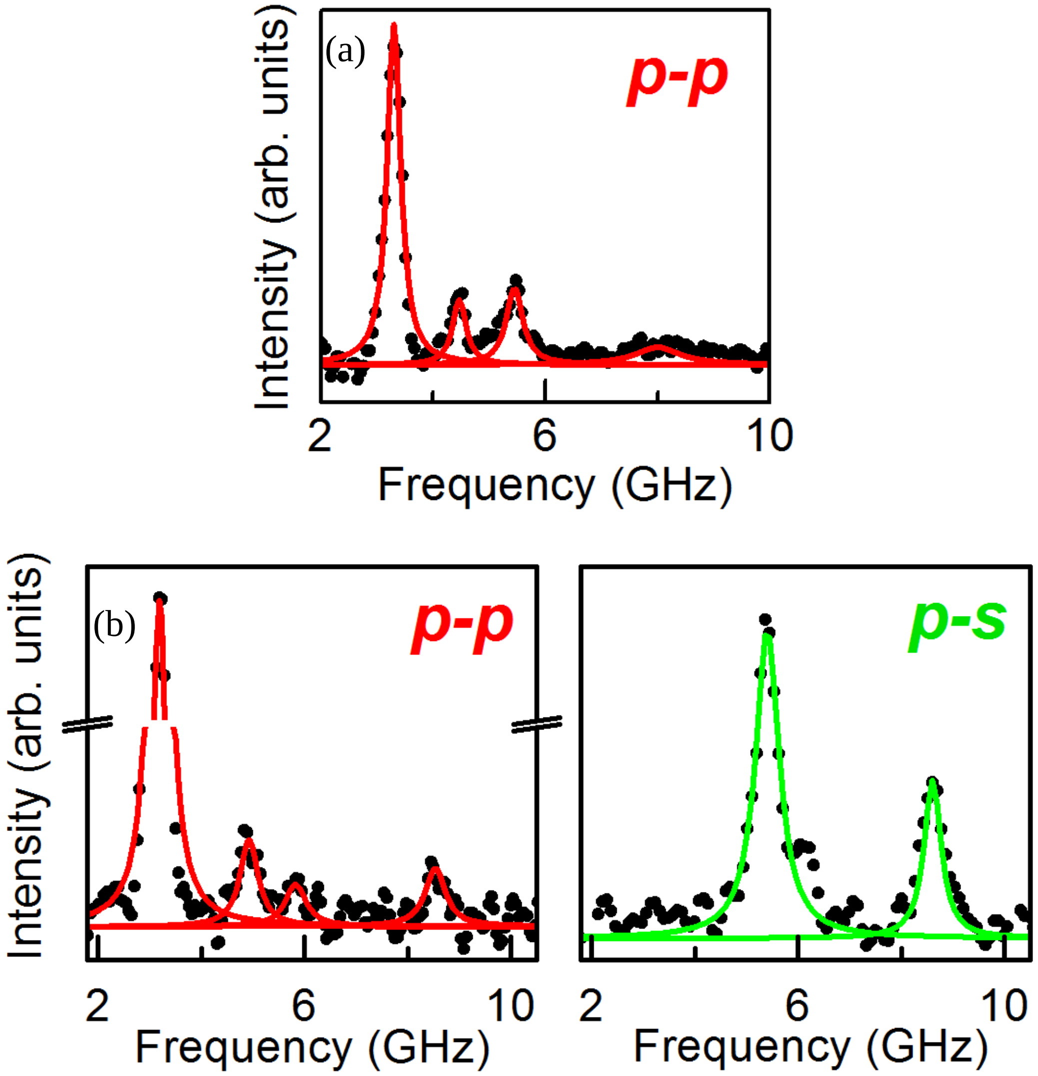

Fig. 7.4 (a) Brillouin *p*-*p* polarization spectrum for wavevector $q = 0.8\pi/a$ along Γ-X. (b) Brillouin *p*-*p* and *p*-*s* polarization spectra for $q = 0.8\pi/a$ along Γ-M.

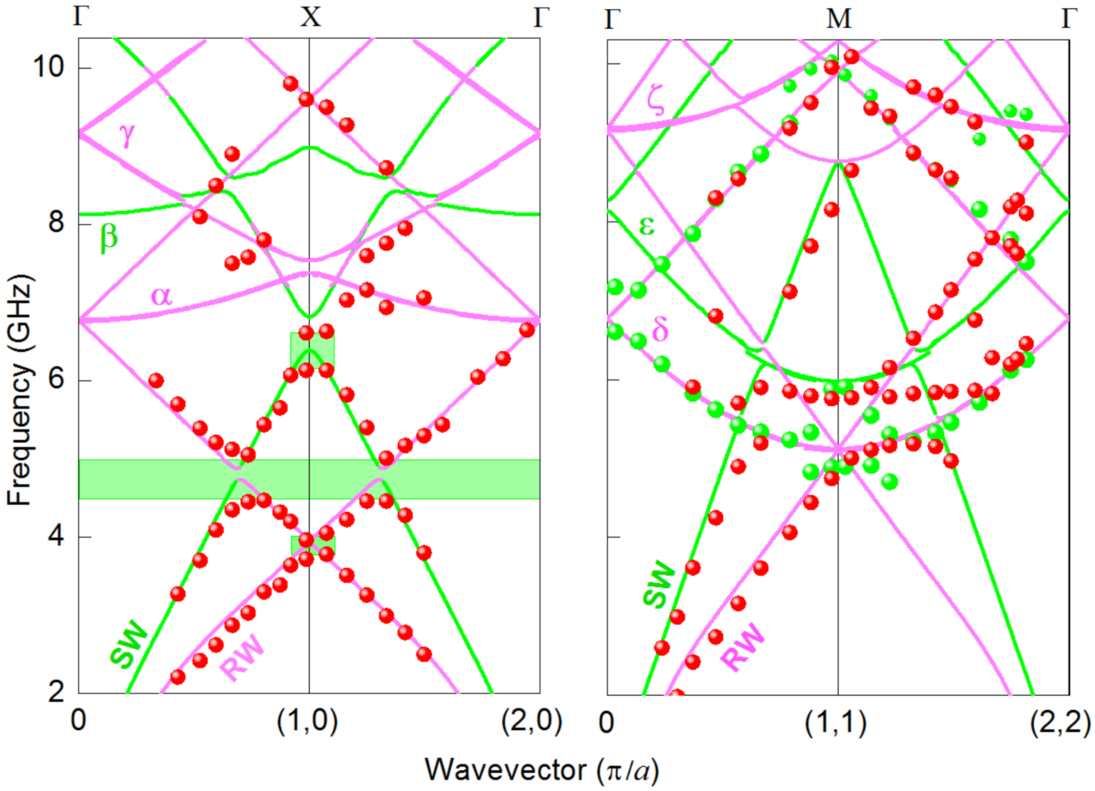

Fig. 7.5 Experimental and calculated phononic dispersion relations of the Co/Py chessboard sample. Measured *p-p* and *p-s* polarization data are denoted by respective red and green dots, and calculated data by pink (shear-vertical-dominated modes) and green (longitudinal-dominated modes) curves. Quasi-Rayleigh and quasi-Sezawa wave branches are denoted by RW and SW respectively, while surface optical-like wave branch by Greek letters. Measured gaps are indicated by green regions.

The dispersion relations and mode displacement profiles were calculated for surface elastic waves propagating along the Γ-M and Γ-X directions, within the framework of the finite element approach in COMSOL Multiphysics, with the Bloch-Floquet theorem applied along the periodicity directions. The simulations proper were performed by Hou Chenguang (H. H. Pan’s fellow PhD student). We considered a 2D 50 nm-thick periodic array of alternating cobalt and Py square dots arranged in a chessboard configuration in contact with a 300 nm-thick silica sub-layer atop a 10 μm-thick Si substrate, with its bottom boundary fixed. The computational unit cell used, with a square cross section of side $a = 250\sqrt{2}$ nm, is illustrated in Fig. 7.6.

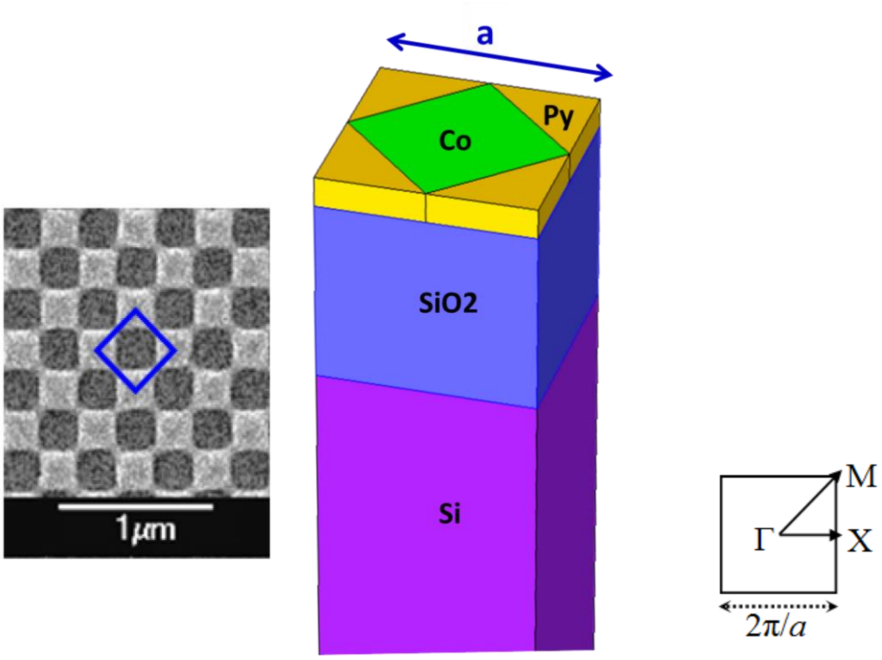

Fig. 7.6 Computational unit cell.

Parameters used in the numerical calculations for Co, Py and SiO_2 are Young's moduli = 209, 113 and 73 GPa, Poisson ratios = 0.31, 0.3 and 0.17 and densities = 8900, 8600 and 2200 kg/m^3 respectively [16-18]. For Si, elastic modulus values of $C_{11} = 166$, $C_{12} = 64$, and $C_{44} = 80$ GPa and density = 2331 kg/m^3 were used [19]. Surface elastic waves were obtained by setting the strain-energy-weighted average depths of energy (DOE) above the SiO_2/Si interface.

$$\mathrm{DOE} = \int z\rho_{\mathrm{E}}\mathrm{d}V \Big/ \int \rho_{\mathrm{E}}\mathrm{d}V \tag{7.1}$$

where z is the depth measured from the top metal surface, ρ_E the strain energy density and dV the volume element [20].

7.4 Results and discussions

Figure 7.7 displays the top view of the *u*-, *v*- and *w*-displacements of the $q = 0.8\pi/a$ surface waves, corresponding to the observed Brillouin peaks in Γ-X and Γ-M directions, which reveal that the simulated profiles have dominant sagittal polarization. Here *u*, *v* and *w* refer to the longitudinal, shear horizontal and shear vertical displacement components, respectively. The mode profiles show that there are broadly two types of surface waves propagating on the sample, namely surface acoustic-like (SAWs) and surface optical-like (SOWs) waves. The chessboard-like structural nature of the bi-component array studied gives rise to an unusual class of surface waves, which we refer to as SOWs as in these excitations. The vibrations of neighboring nanodots have out-of-phase aspects, as mentioned earlier. Based on the simulated displacement profiles for Γ-X, the Brillouin peaks p1 - p3 are assigned to SAWs and p4 to a SOW (Fig. 7.7a). Corresponding profiles for Γ-M indicate that peaks p1’ and p2’ are due to SAWs and p3’ - p6’ to SOWs (Fig. 7.7b).

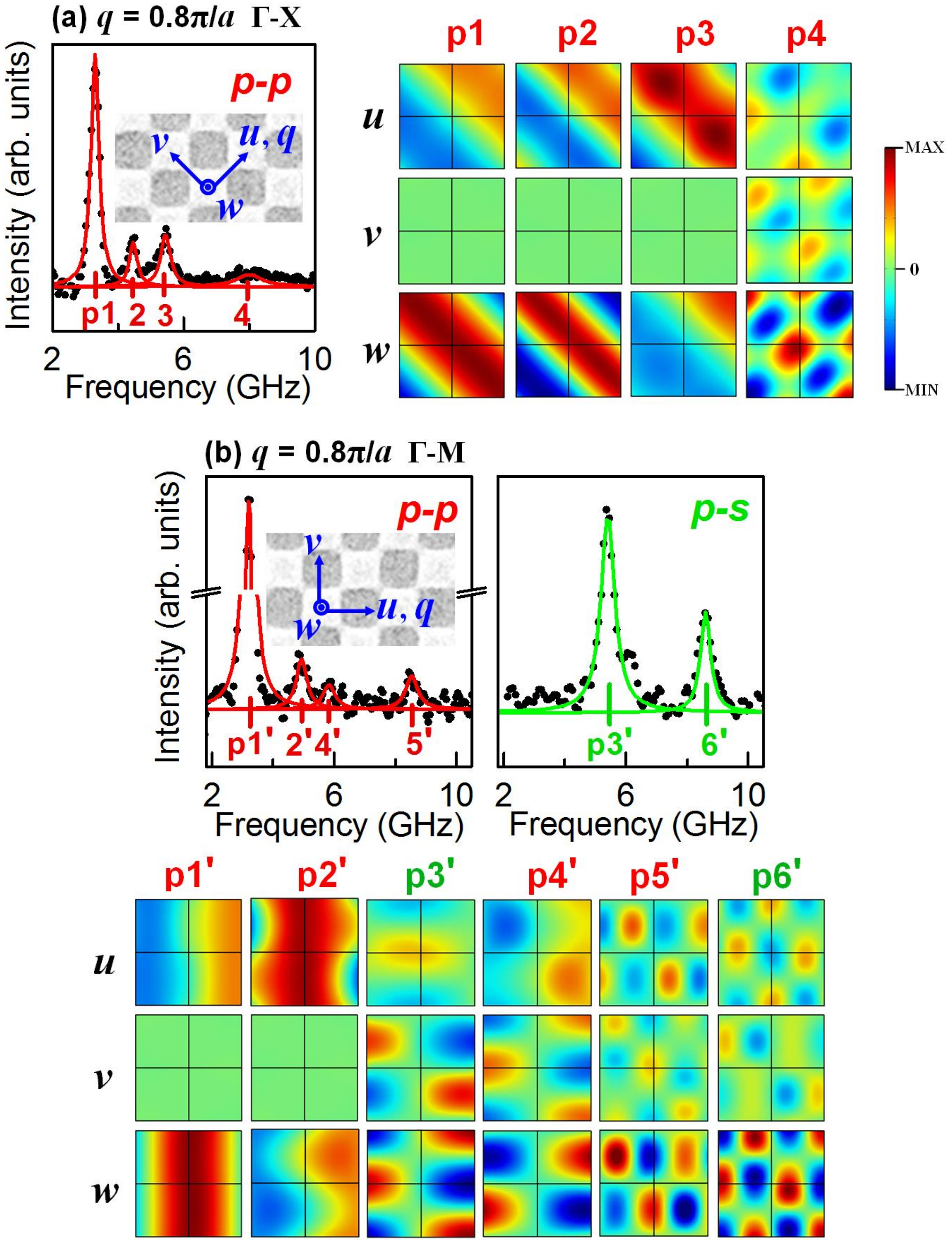

Fig. 7.7 Simulated top-view displacement profiles of observed modes. *u*, *v* and *w* refer to longitudinal, shear horizontal and shear vertical displacement components, respectively.

The calculated dispersion relations of surface waves along X-Γ-M are illustrated in Fig. 7.8, which shows the shear-vertical-dominated and longitudinal-dominated branches represented by pink and green curves respectively. Also presented are the *w*-displacement (shear-vertical) profiles, at the M and X points, of some modes. From an examination of their profiles, modes a, b, k are identified as quasi-Rayleigh waves (RWs), while c, d, p, as quasi-Sezawa waves (SWs). Additionally, the e-h, g-i, f-j, h-l, i-o and h-r branches have SOW character. Hence, Brillouin peaks p1 and p2 are assigned to RWs (propagating in opposite directions) and p3 to SWs (Fig. 7.7a). Also, peaks p1’ and p2’ are due to a RW and a SW respectively (Fig. 7.7b). It is noteworthy that optical and acoustic phonons can mix, resulting in a hybrid mode nature, as is the case for p2’ (SW) and p4’ (SOW) which have very close frequencies. As a consequence, the SW acquires some optical character, while the SOW some acoustic character (Fig. 7.7b).

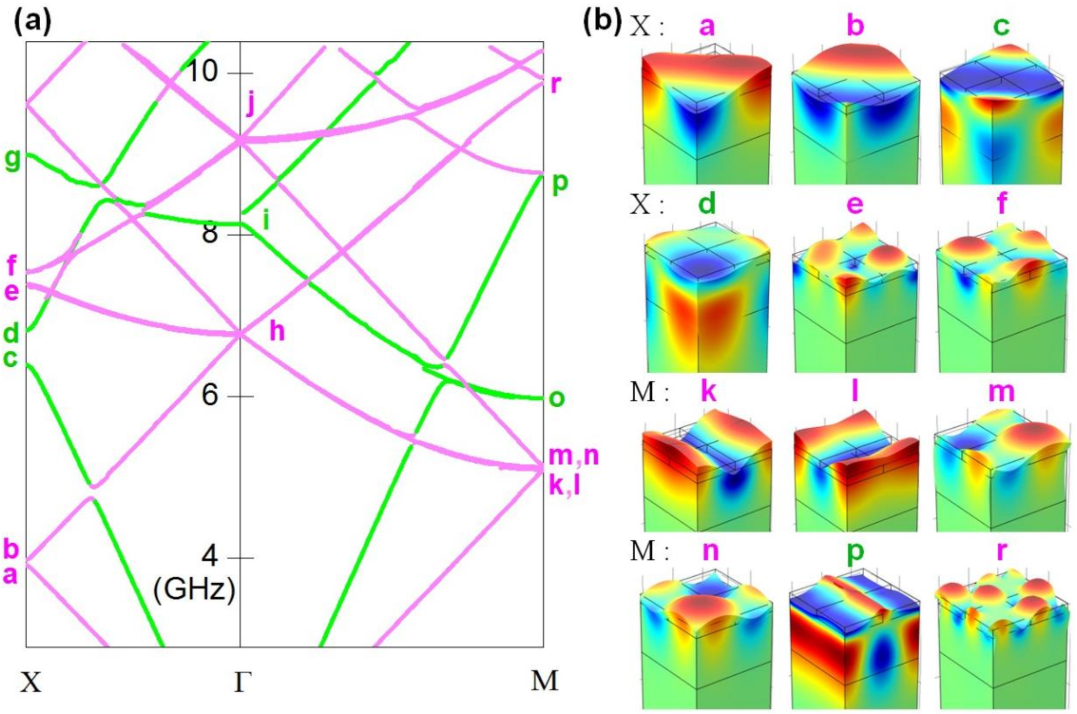

Fig. 7.8 (a) Calculated phononic band structures of the Co/Py chessboard sample. Shear-vertical-dominated and longitudinal-dominated modes are represented by pink and green curves respectively. (b) The *w*-displacements (shear vertical), color-coded according to the scale bar of Fig. 7.7, of selected modes for the M and X points.

The calculated data are also shown as separate Γ-M and Γ-X dispersion spectra in Fig. 7.5, revealing that the calculations generally reproduced the experimental dispersion relations. In particular, good agreement was obtained for the RW and SW branches, as well as the SOW branches labeled as α, δ, and ζ. The Γ-X dispersion spectrum features a 0.12 GHz-wide hybridization bandgap (measured width = 0.5 GHz), which opens up at $q \approx 0.7\pi/a$ and $1.3\pi/a$. This feature arises from the respective hybridization and avoided crossings of the zone-folded RW and SW, and those of the RW and zone-folded SW [21]. Also presented are the two gap openings, at the X point, with respective calculated widths of 0.04 and 0.35 GHz, in fair agreement with the experiment. The first gap is a consequence of the zone folding of the RW dispersions and avoided crossings at the BZ boundaries, while the second gap is due to the zone folding of the SW dispersions and avoided crossings [11]. It should be noted that the elastic parameters used in the simulations were not obtained from a fitting to the measured band structures, but rather from the literature.

7.5 Conclusions

In conclusion, employing Brillouin spectroscopy, we have mapped the Γ-M and Γ-X phononic dispersions of a 2D chessboard-patterned bi-component structure on a SiO_2/Si substrate. The measured phononic band structures of surface elastic waves are rich in features like the partial hybridization bandgap in the Γ-X direction, and gap openings, arising from Bragg reflection, at the X-point. Of note are the unusual surface optical-like modes arising from the out-of-phase vibrations of neighboring square dots, broadly akin to the atomic vibrations of the optical mode of a crystal with two different atoms per unit cell. Numerical simulations, based on the finite element analysis, generally reproduced the experimental dispersion relations. A recent observation has been made of the magnonic dispersion of a similar array of Co and Py square dots made synthesized a different fabrication procedure [22]. Our sample will also exhibit magnonic dispersion and hence is a 2D magphonic crystal, i.e., one possessing dual phononic and magnonic bandgaps [3]. Our findings open prospects for the further understanding and development of phononic-crystal-based devices. Potential devices based on the present quasi-planar structure studied could be suitable for integration in electronic integrated circuits, e.g., for acoustical signal processing, using planar technology.

References:

1. M. Gorisse, S. Benchabane, G. Teissier, C. Billard, A. Reinhardt, V. Laude, E. Defaÿ and M. Aïd, Appl. Phys. Lett. **98**, 234103 (2011).

2. Y. M. Soliman, M. F. Su, Z. C. Leseman, C. M. Reinke, I. El-Kady, and R. H. Olsson III, Appl. Phys. Lett. **97**, 193502 (2010).

3. V. L. Zhang, F. S. Ma, H. H. Pan, C. S. Lin, H. S. Lim, S. C. Ng, M. H. Kuok, S. Jain, and A. O. Adeyeye, Appl. Phys. Lett. **100**, 163118 (2012).

4. W. Cheng, J. J. Wang, U. Jonas, G. Fytas, and N. Stefanou, Nat. Mater. **5**, 830 (2006).

5. T. Gorishnyy, C. K. Ullal, M. Maldovan, G. Fytas, and E. L. Thomas, Phys. Rev. Lett. **94**, 115501 (2005).

6. T. Gorishnyy, J.-H. Jang, C. Koh, and E. L. Thomas, Appl. Phys. Lett. **91**, 121915 (2007).

7. D. Schneider, F. Liaqat, E. H. El Boudouti, Y. El Hassouani, B. Djafari-Rouhani, W. Tremel, H.-J. Butt, and G. Fytas, Nano Lett. **12**, 3101 (2012).

8. P. E. Hopkins, C. M. Reinke, M. F. Su, R. H. Olsson III, E. A. Shaner, Z. C. Leseman, J. R. Serrano, L. M. Phinney, and I. El-Kady, Nano Lett. **11**, 107 (2010).

9. A. V. Akimov, Y. Tanaka, A. B. Pevtsov, S. F. Kaplan, V. G. Golubev, S. Tamura, D. R. Yakovlev, and M. Bayer, Phys. Rev. Lett. **101**, 033902 (2008).

10. N. Papanikolaou, I. E. Psarobas, and N. Stefanou, Appl. Phys. Lett. **96**, 231917 (2010).

11. J. R. Dutcher, S. Lee, B. Hillebrands, G. J. McLaughlin, B. G. Nickel, and G. I. Stegeman, Phys. Rev. Lett. **68**, 2464 (1992).

12. S. Lee, L. Giovannini, J. R. Dutcher, F. Nizzoli, G. I. Stegeman, A. M. Marvin, Z. Wang, J. D. Ross, A. Amoddeo, and L. S. Caputi, Phys. Rev. B **49**, 2273 (1994).

13. A. A. Maznev, Phys. Rev. B **78**, 155323 (2008).

14. B. Graczykowski, S. Mielcarek, A. Trzaskowska, J. Sarkar, P. Hakonen, and B. Mroz, Phys. Rev. B **86**, 085426 (2012).

15. H. H. Pan, Z. K. Wang, H. S. Lim, S. C. Ng, V. L. Zhang, M. H. Kuok, T. T. Tran, and X. M. Lu, Appl. Phys. Lett. **98**, 133123 (2011).

16. D. D. Tang and Y.-J. Lee, *Magnetic Memory* (Cambridge University Press, New York, 2010).

17. X. P. Li, G. F. Ding, H. Wang, T. Ando, M. Shikida, and K. Sato, in *Transducers & Eurosensors '07, The 14th International Conference on Solid-State Sensors, Actuators and Microsystems* (Lyon, France, 2007), p. 555.

18. B. A. Auld, *Acoustic Fields and Waves in Solids*, Vol. 2 (Wiley, New York, 1973).

19. Y. El Hassouani, C. Li, Y. Pennec, E. H. El Boudouti, H. Larabi, A. Akjouj, O. Bou Matar, V. Laude, N. Papanikolaou, A. Martinez, and B. Djafari Rouhani, Phys. Rev. B **82**, 155405 (2010).

20. R. S. Westafer, S. Mohammadi, A. Adibi, and W. D. Hunt, in *Proceedings of the COMSOL Conference* (Boston, 2009).

21. A. A. Maznev and A. G. Every, J. Appl. Phys. **106**, 113531 (2009).

22. G. Gubbiotti, S. Tacchi, M. Madami, G. Carlotti, S. Jain, A. O. Adeyeye, and M. P. Kostylev, Appl. Phys. Lett. **100**, 162407 (2012).

Chapter 8 Conclusions

Nanostructured materials, the foundation of nanoscience and nanotechnology, are attracting increasing interest due to their unique properties and numerous technological applications in a vast variety of areas such as catalysis, nonlinear optics, electronics, and sensing devices [1-3]. Many complex shaped nanoparticles and patterned periodic structures have been fabricated. The former can have confined acoustic modes, while the latter, which could serve as phononic crystals, are able to modify the propagation of sound waves passing through them. An understanding of their acoustic and mechanical properties is of great importance to both fundamental physics and their applications.

In this thesis, Brillouin light scattering (BLS), a powerful technique for probing the elastic properties and phonon propagation in nanostructured materials at hypersonic frequencies [4-9], was employed to investigate the confined acoustic phonons in single-crystal gold nano-octahedra and the surface phonon dispersions in one- and two-dimensional hypersonic phononic crystals. Theoretical investigations, based on finite element analysis, of the acoustic vibrational modes of gold nano-octahedra and the phonon dispersions of the phononic crystals were also undertaken.

A series of high-quality octahedron-shaped gold nanocrystals with face-centered cubic crystal symmetry of different sizes has been examined by BLS to ascertain the size-dependence of their acoustic vibrational modes as detailed in

Chapter 4. Up to nine well-resolved Brillouin peaks were observed for octahedra with edge lengths larger than 70 nm. The intensities of the peaks progressively decrease with frequency, which is a characteristic of the confined acoustic modes of a nano-object [4-8]. A finite element analysis was also performed to calculate the vibrational modes of a gold octahedron. In order to identify modes with large Brillouin scattering intensities [8,10], the scattering cross-sections of the modes were also calculated. The agreement between calculated spectra and the observed ones is fairly reasonable considering that certain approximations and assumptions have been made. The calculation of the intensities of the modes is non-trivial for non-spherical (e.g. octahedron-shaped) metallic anisotropic nanoparticles, and thus the mode intensities were only estimated.

Our analysis reveals that the observed peaks are due to eigenvibrations of individual nano-octahedra resulting from spatial confinement with each peak arising from more than one vibrational mode. This finding of multimode spectral peaks is consistent with an earlier BLS study of isotropic polystyrene and silica nanospheres by Still *et al.* [8]. It was also established that the mode frequencies of the gold nanocrystals are inversely proportional to the octahedron diagonal and that their elastic constants are comparable to those of bulk gold crystals. The findings, together with similar ones reported for spheres and cubes [4–8], suggest that the frequencies of the confined eigenvibrations of any free regular-shaped homogeneous object always scale with its inverse linear dimension. Additionally, they imply that this universal relationship is valid for such objects of any size in the classical regime and is not dependent on their elastic properties. These findings would provide guidance to theoretical investigations into the confined acoustic eigenmodes of such objects.

Further calculations of the Brillouin scattering intensities of the vibrational modes of these non-spherical crystalline particles have to be performed to provide a quantitatively accurate Brillouin spectrum. For a comprehensive assignment of the experimentally observed modes, theoretical work on the mode classification has also to be carried out based on group theoretical methods.

As documented in Chapter 5, the surface acoustic wave (SAW) dispersion relations of periodic arrays of alternating $Ni_{80}Fe_{20}$ (Py) and Fe (or Ni, Cu) nanostripes on a SiO_2/Si substrate have been mapped by Brillouin spectroscopy. For each sample, four gaps were observed. Two of them are assigned to Bragg gaps at the Brillouin zone boundaries, which have their origin in the folding of surface Rayleigh wave dispersion in periodic structures. Moreover, it was found that these gaps increase in size with zone numbers, which agrees with the previous theoretical predictions [11]. Another two gaps observed within the second and third Brillouin zones are assigned to hybridization gaps arising from the avoided crossing of the Rayleigh waves and the zone-folded Sezawa waves, also known as high-order Rayleigh waves. Hybridization gaps were also observed by Maznev in his study of copper lines embedded in SiO_2 film on a Si(001) wafer [12].

Besides experimental work, theoretical surface phonon band structures and mode displacement profiles were calculated within the framework of the finite element approach using the COMSOL Multiphysics software with the Bloch theorem applied along the periodicity direction. The calculated dispersions captures the features of the Brillouin measured ones. The measured dispersion relations of the three samples studied were found to be similar, a consequence of the similar densities and elastic parameters of their constituent materials.

In general, the phononic bandgap width increases with elastic and density contrast [9]. Indeed the phononic gaps of the above-mentioned 1D phononic structures are small, being of the order of 0.5 GHz. In order to achieve high contrast, Py and BARC (bottom anti-reflective coating) were chosen to be the constituent materials. In Chapter 6, two phononic crystals in the form of 1D linear periodic arrays of alternating Py and BARC nanostripes on a Si(001) substrate, with respective 350 nm and 400 nm lattice constants, were investigated by BLS. The measured phononic dispersion spectrum of each sample features a Bragg gap opening at the Brillouin zone boundary, and a large hybridization bandgap. This hybridization bandgap has a unique origin, which is different from those reported for other 1D periodic phononic crystals [12-16], in the hybridization and avoided crossing of the zone-folded Rayleigh and pseudo-Sezawa waves. In addition, the measured phononic Bragg gap openings and hybridization bandgaps are found to be much wider than those previously observed in laterally patterned multi-component phononic crystals. It was observed that the SAW dispersion and gap widths could be experimentally tuned by changing the periodicity of the phononic structure. Our findings could be of use in designing phononic-crystal-based devices for applications in e.g. acoustical signal processing. Modes of the third lowest-energy branch of the dispersion relation of each sample, reveal near-localization characteristics. Such near-dispersionless branches were also observed by Maznev [12], but no explanation was put forward for their existence. Numerical simulations, carried out within the finite element framework, of the phononic dispersions yielded good agreement with experiments.

Most experimental studies that measured SAW dispersion curves in phononic crystals are confined to 1D structures [12-16]. It is thus of interest to investigate higher-dimensional periodic structures whose surface phononic dispersions are more complex and richer in features than those of the 1D phononic crystals. Chapter 7 reports the theoretical and experimental band structures of the surface acoustic and surface optical waves on a 2D chessboard-patterned phononic crystal. The sample studied comprised a periodic array of alternating Permalloy and cobalt square nanodots on a SiO_2/Si substrate. Employing Brillouin spectroscopy, we experimentally observed quasi-Rayleigh and quasi-Sezawa waves, and measured the comprehensive phononic dispersion relations over a full Brillouin zone. We were able to obtain measured dispersion spectra along the Γ-M and Γ-X directions, including the folded branches (over two Brillouin zones). The measured phononic band structures of SAWs are rich in features like the partial hybridization bandgap in the Γ-X direction, and gap openings, arising from Bragg reflection, at the X-point.

Of particular interest is the observation of an unusual class of surface elastic waves, arising from the chessboard-like structural nature of the bi-component array studied. We refer to them as “optical-like”, as the vibrations of neighboring nanodots possess out-of-phase characteristics, a motion broadly analogous to the atomic vibrations of the optical mode of a crystal with two different atoms per unit cell. Numerical simulations, based on the finite element analysis, generally reproduced the experimental dispersion relations. Recently, another BLS study on SAW dispersion relations in 2D phononic crystals comprising a square lattice of aluminum pillars on a Si(001) substrate was reported by Graczykowski *et al.* [17]. The phonon dispersion spectra of our 2D chessboard-patterned bi-component phononic structure exhibit features that are much richer and more interesting than those of their samples.

It should be noted that all the phononic samples studied contain a magnetic component. These samples also exhibit magnonic dispersions and hence are magphonic crystals, i.e., one possessing dual phononic and magnonic bandgaps [16,18]. Because of the possibility of simultaneously controlling and manipulating magnon and phonon propagation in them, magphonic crystals could find applications in areas such as acoustic and spin-wave signal processing. For the magphonic samples studied here, while application of a magnetic field radically modifies their magnon dispersion spectra, their corresponding phonon ones are found to be independent of magnetic field, suggesting the absence of magnon-phonon interactions. This has important implications for potential applications. For instance, information carried by magnons and phonons could be separately and simultaneously processed in devices based on such magphonic crystals, with no undesirable cross-talk between the two excitations. Additionally the magnonic bandgaps in such devices can be tuned by the application of a magnetic field, independently of the phononic bandgaps. Further research into these interesting properties of magphonic crystals, a novel class of metamaterials, should prove to be rewarding in terms of fundamental science and technological applications.

References:

1. P. Moriarty, *Nanostructured materials*, Rep. Prog. Phys. **64**, 297 (2001).

2. V. C. Yang and T. T. Ngo, *Biosensors and Their Applications,* (Springer, 2000).

3. G. Merga, N. Saucedo, L. C. Cass, J. Puthussery, and D. Meisel, J. Phys. Chem. C **114**, 14811 (2010).

4. M. H. Kuok, H. S. Lim, S. C. Ng, N. N. Liu, and Z. K. Wang, Phys. Rev. Lett. **90**, 255502 (2003); **91**, 149901(E) (2003).

5. W. Cheng, J. J. Wang, U. Jonas, W. Steffen, G. Fytas, R. S. Penciu, and E. N. Economou, J. Chem. Phys. **123**, 121104 (2005).

6. H. S. Lim, M. H. Kuok, S. C. Ng, and Z. K. Wang, Appl. Phys. Lett. **84**, 4182 (2004).

7. Y. Li, S. Lim, S. C. Ng, M. H. Kuok, F. Su, and X. S. Zhao, Appl. Phys. Lett. **90**, 261916 (2007).

8. T. Still, M. Mattarelli, D. Kiefer, G. Fytas, and M. Montagna, J. Phys. Chem. Lett. **1**, 2440 (2010).

9. W. Cheng, J. J. Wang, U. Jonas, G. Fytas, and N. Stefanou, Nat. Mater. **5**, 830 (2006).

10. M. Montagna, Phys. Rev. B **77**, 045418 (2008).

11. F. Rischbieter, Acustica **16**, 75 (1965).

12. A. A. Maznev, Phys. Rev. B **78**, 155323 (2008).

13. A. A. Maznev and O. B. Wright, J. Appl. Phys. **105**, 123530 (2009).

14. J. R. Dutcher, S. Lee, B. Hillebrands, G. J. McLaughlin, B. G. Nickel, and G. I. Stegeman, Phys. Rev. Lett. **68**, 2464 (1992).

15. L. Dhar and J. A. Rogers, Appl. Phys. Lett. **77**, 1402 (2000).

16. V. L. Zhang, F. S. Ma, H. H. Pan, C. S. Lin, H. S. Lim, S. C. Ng, M. H. Kuok, S. Jain, and A. O. Adeyeye, Appl. Phys. Lett. **100**, 163118 (2012).

17. B. Graczykowski, S. Mielcarek, A. Trzaskowska, J. Sarkar, P. Hakonen, and B. Mroz, Phys. Rev. B **86**, 085426 (2012).

18. V. L. Zhang, C. G. Hou, H. H. Pan, F. S. Ma, M. H. Kuok, H. S. Lim, S. C. Ng, M. G. Cottam, M. Jamali, and H. Yang, Appl. Phys. Lett. **101**, 053102 (2012).